이학박사 학위논문

A Quasi-Stochastic Collection Model and Cloud and Precipitation Modeling

준확률 포착 모형과 구름 및 강수 모델링

2018년 2월

서울대학교 대학원

지구환경과학부

Jambajamts Lkhamjav

A Quasi-stochastic Collection Model and Cloud and Precipitation Modeling

By

Jambajamts Lkhamjav

A Dissertation Submitted to the Faculty of the Graduate School of Seoul National University in Partial Fulfillment of the Requirements for the Degree of Doctor of Philosophy

February 2018

Advisory Committee:

Professor Gyu-Ho Lim, Chair

Professor Jong-Jin Baik, Advisor

Professor Sang-Woo Kim

Professor Sang-Hyun Lee

Doctor Young-San Park

Abstract

The evolution of cloud drop size distribution due to the collision-coalescence process is generally described by a quasi-stochastic model that solves the stochastic collection equation (SCE) in a deterministic way. In this study, an improved quasi-stochastic (IQS) model, which is derived by rigorously considering a finite model time step, is examined in the context of comparison with the normal quasi-stochastic (NQS) model. The IQS model allows a large collector drop to collide with a small collected drop more than one time in a model time step even if the collision probability is small. The number distribution of collector drops then follows the Poisson distribution with respect to the number of collisions. Using a box model that takes turbulence-induced collision enhancement (TICE) into account, it is found that large drops in the IQS model tend to have larger sizes than those in the NQS model and that the IQS model accelerates large-drop formation by a few minutes compared to the NQS model. The effects of the IQS model depend on the model time step and the shape of initial drop size distribution. The IQS model is incorporated into a detailed bin cloud microphysics scheme that is coupled with the Weather Research and Forecasting (WRF) model, and a single warm cloud is simulated under idealized environmental conditions. It is found that the onset of surface precipitation is accelerated in the IQS model.

The IQS model against the NQS model in precipitation prediction is evaluated. For this, a precipitation event observed over north central Mongolia on 21 August 2014 is simulated using the WRF model with a detailed bin cloud microphysics scheme. The

surface precipitation amount is larger in the IQS model than in the NQS model, particularly over the strong precipitation region. The IQS model increases the mass contents of small drops and large drops due to multiple collisions. The increased large drops contribute to the increase in surface precipitation amount. The increased small drops are transported upward, which eventually leads to an increase in snow mass content. Deposition and riming in the IQS model occurs more actively, further increasing snow mass content. The increased snow mass content also contributes to the increase in surface precipitation amount through melting.

The impacts of aerosol loading on surface precipitation from mid-latitude deep convective systems are examined. For this, a precipitation case over north central Mongolia on 21 August 2014 is simulated with aerosol number concentrations of N_0 = 150, 300, 600, 1200, 2400, and 4800 cm^{-3}. The surface precipitation amount slightly decreases with increasing aerosol number concentration in the range of N_0 = 150–600 cm^{-3}, while it notably increases in the range of N_0 = 600–4800 cm^{-3} (22% increase with eightfold aerosol loading). An attempt is made to explain why the surface precipitation amount increases with increasing aerosol number concentration in the N_0 = 600–4800 cm^{-3} range. Higher aerosol number concentration results in more drops of small sizes. More drops of small sizes grow through condensation while being transported upward and some of them freeze, thus increasing the mass content of ice crystals. The increased ice crystal mass content leads to an increase in the mass content of small-sized snow particles largely through deposition, and the increased mass content of small-sized snow particles leads to an increase in the mass content of large-sized snow particles largely

through riming. Also, more drops of small sizes increase the mass content of supercooled drops, which leads to an increase in the mass content of large-sized snow particles through riming. The increased mass content of large-sized snow particles resulted from these pathways contributes to a larger surface precipitation amount through melting and collision-coalescence.

Keywords: improved quasi-stochastic collection model, bin cloud microphysics, WRF model, clouds and precipitation, aerosols, hail climatology, Mongolia.

Student number: 2014-30900

Contents

List of Figures

List of Tables

1. Introduction

Cloud drops with radii smaller than ~15 μm grow efficiently by diffusion of water vapor. However, although water vapor diffusion in a turbulent environment is somewhat controversial (McGraw and Liu, 2006; Grabowski and Wang, 2013), droplet growth by water vapor diffusion tends to be inefficient as the drop size increases, and cloud drops with radii larger than ~40 μm largely grow by collision-coalescence (Langmuir, 1948; Kogan, 1993; Beard and Ochs, 1993; Pruppacher and Klett, 1997). Therefore, drop collision-coalescence is an important processes in increasing drop size in warm clouds. Many studies on drop collision-coalescence have been performed using theoretical, experimental, and numerical approaches.

Two models have been proposed to describe the collisional growth of drops: the continuous model and the stochastic model (Gillespie, 1975a; Pruppacher and Klett, 1997). The continuous model assumes that all drops of the same size grow by the same growth rate. The continuous model predicts very slow formation of large drops, which is mainly caused by ignoring the stochastic nature in drop collision that occurs in real clouds. Telford (1955) first introduced the stochastic interpretation for the modeling of drop collision, in which not all the drops grow by the same growth rate but some drops are involved in collision while others are not. Telford (1955) derived the stochastic model that solves the stochastic collection equation (SCE) to describe the collisional growth of drops. Twomey (1964) showed that the stochastic model substantially

accelerates the formation of large drops compared to the continuous model.

Gillespie (1972; 1975b) and Bayewitz et al. (1974) considered the stochastic nature of drop collision more rigorously and showed that $N(m; t)$, which corresponds to the number of drops with mass m at time t, is replaced by $P(n, m; t)$, which corresponds to the probability that there are n drops with mass m at time t, as a predicted variable. Gillespie (1975a) called the newly proposed model a pure stochastic model and called the previously used stochastic model a quasi-stochastic model. Wang et al. (2006) further improved the pure stochastic model by specifying the range of drop size in calculating covariance to exclude unphysical coalescence and by requiring the mass conservation in solving the SCE. Alfonso (2013) applied the turbulence-induced collision enhancement (TICE) (Pinsky et al., 2008) to the pure stochastic model and introduced so-called 'sol-gel transition' in describing large drop formation.

The pure stochastic model is regarded as accurately describing the evolution of drop size distribution due to collision. However, the pure stochastic model generally requires a huge amount of computing time because numerous Monte Carlo experiments have to be done to acquire reasonable statistics (mean and deviation) on the drop size distribution. Some efforts have been made to improve the efficiency of the pure stochastic model (e.g., Alfonso, 2015). Because the quasi-stochastic model has better computational efficiency compared to the pure stochastic model and higher accuracy compared to the continuous model, thus far, the quasi-stochastic model has been the most viable way to treat the collisional growth of drops in cloud models.

Gillespie (1975a) showed that if a collector drop is assumed either to collide

with a collected drop or not to collide with a collected drop in an infinitesimal time interval *dt*, the number distribution of collector drops with respect to their masses (or equivalently to the number of collisions) is given as the Poisson distribution at any given time. Although there is no proper reason that a model time step Δt should be regarded as the same as *dt*, however, almost all models that adopt the quasi-stochastic model regard Δt as the same as *dt* in Gillespie (1975a) and allow a collector drop to collide with a collected drop only one time in Δt, hence neglecting the drop size distribution broadening in a model time step. Young (1975) first recognized the problem and introduced the Poisson distribution to represent the evolution of drop size distribution in a model time step Δt. However, Young (1975) considered only one case and concluded that the consideration of the Poisson distribution in a time step of 5 s accelerates the evolution of drop size distribution by only a few seconds.

In this study, the Poisson distribution in the quasi-stochastic model is revisited and examined under various initial drop size distributions. Moreover, the improved model is incorporated into a detailed bin microphysics scheme that is coupled with a cloud-resolving model and the effects of the improved model on cloud development and precipitation are investigated. In this study, the quasi-stochastic model with the Poisson distribution is referred to as an IQS model (improved quasi-stochastic collection model), while the quasi-stochastic model that allows a collector drop to collide with a collected drop only one time in a finite model time step is referred to as the NQS model (normal quasi-stochastic collection model). The fast raindrop formation in real-world cumuli is one of the important problems in cloud physics. Factors that affect fast raindrop

formation have been proposed, including in-cloud turbulence (e.g. Chen et al., 2017). We will see whether the IQS model accelerates the formation of raindrops or not.

In chapter 2, we examine an improved quasi-stochastic model for the collisional growth of drops. In chapter 3, we evaluate the improved quasi-stochastic collection model through precipitation prediction over north central Mongolia. In chapter 4, we examine the impacts of aerosol loading on surface precipitation from deep convective systems over north central Mongolia. In chapter 5, we examine hail climatology in Mongolia. In chapter 6, a summary and conclusions are given.

2. An improved quasi-stochastic collection model for the collisional growth of drops

2.1. Theoretical background

The basic concept of the improved quasi-stochastic collection (IQS) model was introduced in Gillespie (1975a) and Young (1975). Here, a rigorous derivation of the IQS model is given. The stochastic collection equation (SCE), which describes the rate of change of drop number concentration due to the collection between drops, is given in an integro-differential equation form as

$$\frac{\partial f(m)}{\partial t} = \frac{1}{2}\int_0^m f(m')\,f(m-m')K(m',m-m')dm' - \int_0^\infty f(m)\,f(m')K(m,m')dm', \quad (2.1)$$

where $f(m)dm$ is the drop number concentration in the mass interval of $[m, m + dm]$ and K is the collection kernel that is the product of swept volume and collection efficiency. K is given as

$$K(r_1,r_2) = \pi(r_1+r_2)^2\left|v_t(r_1)-v_t(r_2)\right|\eta, \quad (2.2)$$

where r_1 and r_2 are radii of drops, v_t is the drop terminal velocity, and η is the collection efficiency.

If discretized grid bins are adopted to represent the drop size distribution, Eq. (2.1) can be expressed in a discretized form as (e.g., Straka, 2009)

$$\frac{\partial n_k}{\partial t} = \frac{1}{2}\sum_{i=1}^{k-1} n_i n_j K_{ij} - \sum_{i=1}^{N} n_k n_i K_{ki}, \tag{2.3}$$

where n_i, n_j, and n_k are the drop number concentrations in the i-th, j-th, and k-th bins, respectively, K_{ij} is the collection kernel between the i-th and j-th bins, and N is the largest bin number. The drop masses in the i-th, j-th, and k-th bins m_i, m_j, and m_k satisfy $m_i + m_j = m_k$. Based on Eq. (2.3), if only collision between drops in the i-th and j-th bins is considered, changes in number concentration in the i-th, j-th, and k-th bins in a given model time step Δt are expressed as

$$\Delta n_k = n_i n_j K_{ij} \Delta t, \tag{2.4a}$$

$$\Delta n_i = \Delta n_j = -\Delta n_k. \tag{2.4b}$$

Equation (2.4b) can be expressed as

$$\Delta n_i = -p_i n_i, \tag{2.5a}$$

$$\Delta n_j = -p_j n_j, \tag{2.5b}$$

where p_i and p_j are equal to $n_j K_{ij} \Delta t$ and $n_i K_{ij} \Delta t$, respectively. Based on Eqs. (2.5a) and

(2.5b), collection between drops can be interpreted in a quasi-stochastic way as follows: if p_i is sufficiently small so that it is smaller than 1, then the collection probability for drops in the i-th bin to collide with drops in the j-th bin in a model time step is p_i so the number of drops that are involved in collision is $p_i n_i$ out of n_i. The same is true for drops in the j-th bin.

The collection probability is expressed as the product of number concentration of collected drops, swept volume, collection efficiency, and model time step. Because the model time step used in numerical cloud models is finite, the model time step can be divided into subtime steps, which results in some collector drops that can collide with collected drops more than one time even with sufficiently small collection probability. Let the model time step Δt be divided into M subtime steps. Because the collection probability is linearly proportional to the model time step, the collection probability in the sub-timestep is p/M where p is the collection probability for a given drop pair in a model time step Δt. If collision events are assumed to be independent from each other and the change in collection kernel during a model time step is negligible, then the probability of collision x times when the given model time step is divided into M subtime steps is given as

$$p_M(x) = {}_M\mathrm{C}_x \left(\frac{p}{M}\right)^x \left(1-\frac{p}{M}\right)^{M-x}. \tag{2.6}$$

Equation (2.6) is the binomial distribution. The number of subtime steps can be as large

as infinity. Then, the final form of the probability of collision x times in the model time step is given as

$$\lim_{M\to\infty} p_M(x) = \frac{p^x e^{-p}}{x!}, \tag{2.7}$$

which is the Poisson distribution. Equation (2.7) is also found in Young (1975).

It is noted that the average number of collisions in the model time step in Eq. (2.7) is p, which is the same as in the normal quasi-stochastic collection (NQS) model. Thus, the IQS model introduced in this study (Eq. (2.7)) does not increase the average number of collisions. Rather, by rigorously considering a finite model time step, some collector drops are allowed to collide with collected drops more than one time in the model time step. In the IQS model, the probability of non-collision is increased from $1 - p$ to e^{-p} and the probability of one time-collision is decreased from p to pe^{-p}. While in the NQS model the collector drop either collides one time or does not collide in the model time step, in the IQS model collisions more than one time are allowed, thus resulting in a wider size spectrum of collector drops. Therefore, the IQS model is expected to accelerate the formation of large drops by both considering some collector drops that have more chances to collide with collected drops and broadening the drop size distribution that can further accelerate collision.

It is also noted that p sometimes exceeds 1 depending on the number concentrations of drops, the size and terminal velocity of drops, and the model time step. Under this situation, the NQS model treats the collision in the same way as the

continuous model; all of collector drops collide with collected drops p times. On the other hand, the IQS model treats the collision in the same way as when p is less than 1, which is another advantage of the IQS model over the NQS model. When p is sufficiently large, it is known that Eq. (2.7) is approximated by the normal distribution, which simplifies the calculation. (see Appendix: The Detailed algorithm of the IQS model)

In this study, the turbulence-induced collision enhancement (TICE) between drops (Pinsky et al., 2008) is taken into account. It is known that turbulence increases the velocity difference of drops, the correlation of drop number concentrations, and the TICE collision efficiency that is related to aerodynamic properties. Pinsky et al. (2008) provided in a tabulated form that is a function of radii of drop pair and the turbulence intensity. Therefore, in this study, can calculate the evolution of drop size distribution with high accuracy using the IQS model that includes the TICE.

2.2. Results and discussion

2.2.1 Box model

To examine the evolution of drop size distribution and the formation of large drops using the NQS and IQS models, a simple box model that considers only collision of drops is employed in this study. To calculate the collection kernel (Eq. (2.2)), the terminal velocity of drops in Beard (1976), the collision efficiency of drops in Pinsky et

al. (2001), and the TICE in Pinsky et al. (2008) are adopted. The coalescence efficiency is assumed to be 1. The drop size distribution is represented using a bin method with 80 mass-doubling bins in which drop masses are doubled every two bins. The SCE is solved using the exponential flux method proposed in Bott (1998, 2000). The initial drop size distribution is given as a log-normal distribution

$$F(r) = \frac{L}{\sqrt{2\pi}\sigma} \exp\left[-\frac{(\log_2 r - \log_2 r_c)^2}{2\sigma^2} \right], \tag{2.8}$$

where $F(r)$ is the mass concentration of drops with radii of r, L is the total liquid water content and r_c and σ are the median and standard deviation of the distribution, respectively. L is set to 1 g m^{-3}. In the control experiments, r_c and σ are set to 10 μm and 0.33, respectively, and the time step Δt is 10 s. The model is integrated for 90 min.

Figure 2.1 shows the time evolution of mass-size distributions of drops obtained using the NQS and IQS models and the difference between the two models in the control experiments. Also, the mass-size distributions at t = 30 min are shown. In both the models, the rapid mass transition from small drops to large drops is clearly observed at t ~ 25 min (Figures 2.1a and 2.1b). This reflects the nature of drop growth: when the size of drops is relatively small (smaller than ~15 μm), collision between drops is less active so the growth of drops is relatively slow. However, once a small number of relatively large drops (larger than ~40 μm) form, the large drops can effectively grow by

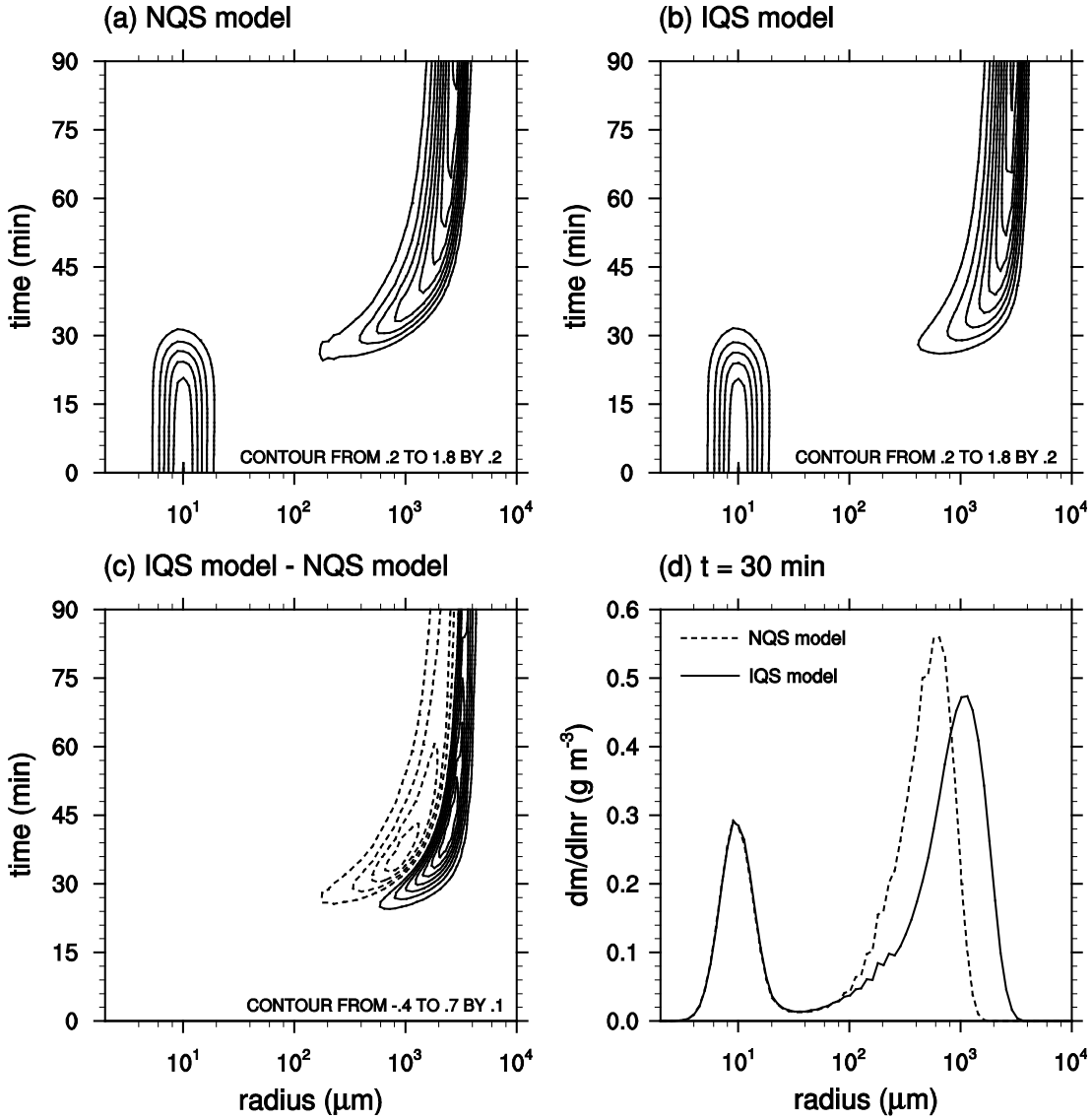

Figure 2.1. Time evolution of mass-size distributions of drops (g m^{-3}) obtained using (a) the NQS model, (b) the IQS model, and (c) difference between the two models in the control experiments. In (c), positive and negative values are depicted by solid and dashed lines, respectively. (d) Mass-size distributions of drops obtained using the NQS and IQS models at t = 30 min.

collecting small drops. This characteristic is also shown in many previous studies (e.g., Berry and Reinhardt, 1974; Khain et al., 2000).

Before the appearance of large drops (t < 25 min), the results obtained using the NQS and IQS models are very similar to each other. The difference between the two models is observed after t ~ 25 min, where the size of large drops tends to be increased in the IQS model. (Figure 2.1c). This is because in the IQS model some drops have more chances to collide with other drops than those in the NQS model, which causes an increase in relatively large drops. The difference in the results is persistent until the end of the time integration. The drop size distribution at t = 30 min clearly shows that large drops in the IQS model tend to have larger sizes than those in the NQS model, while there is little difference in the size distribution of small drops (Figure 2.1d). These effects of the IQS model are also found to be similar when other initial drop size distributions, such as the gamma distribution and the Weibull distribution (Costa et al., 2000), are used.

Sensitivity experiments are conducted. First, experiments in which the model time step is reduced from 10 s to 1 s are conducted because it is expected that the difference between the results of the IQS and NQS models would increase with increased model time step. Figure 2.2 shows the results with Δt = 1 s. Figures 2.2a and 2.2b are similar to Figures 2.1a and 2.1b, respectively, which indicates that both the models show reasonable drop size distribution evolution with Δt ~ 10 s. This agrees with the result in Bott (2000). The difference between the model results with Δt = 1 s is depicted in Figure 2.2c, in which there is still difference between the model results even

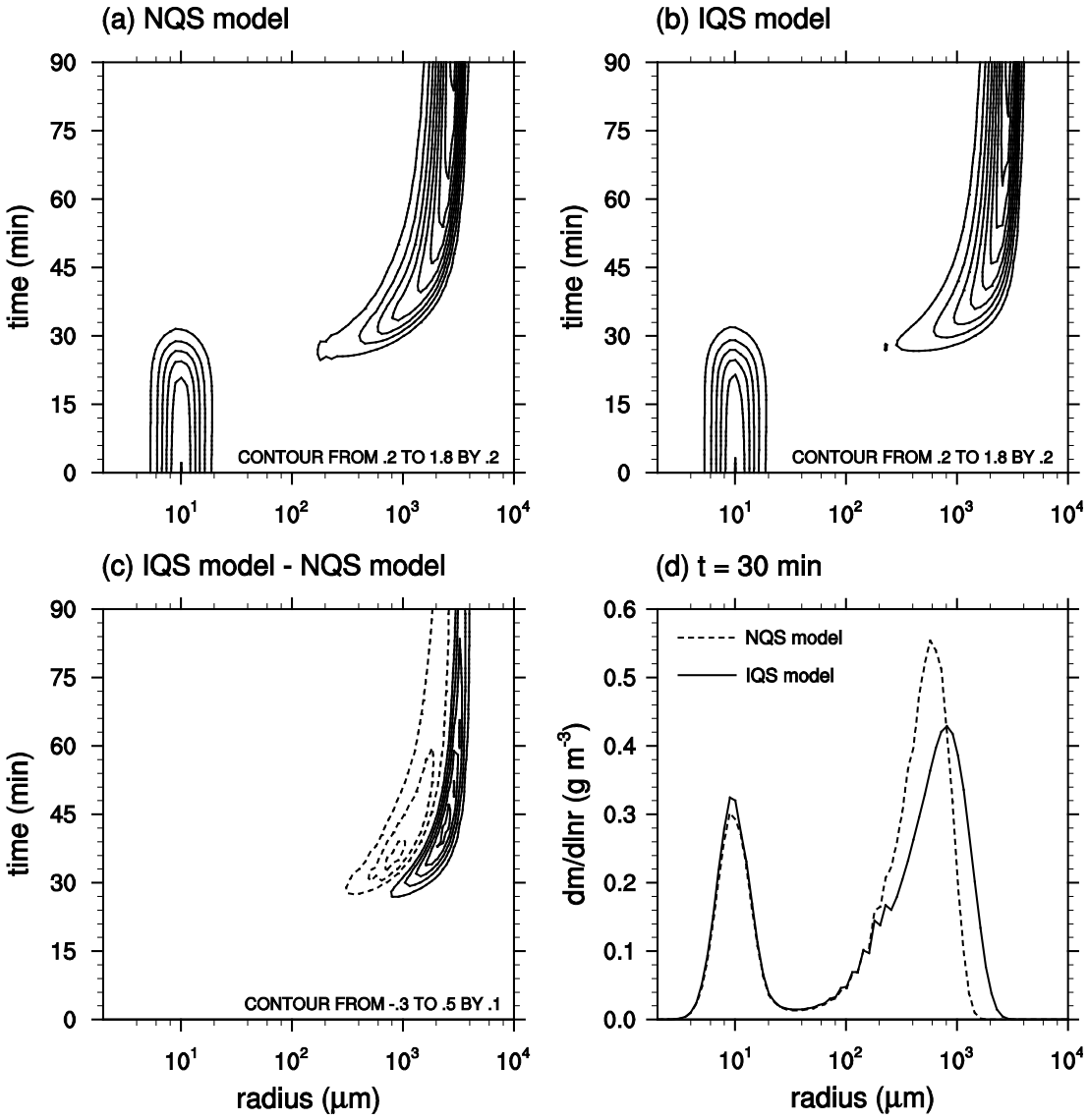

Figure 2.2. Same as in Figure 2.1 but for Δt = 1 s.

with the small model time step. The difference also persist until the end of the time integration. Compared to Figure 2.1c, Figure 2.2c clearly shows that the difference is reduced with the small model time step, as expected. Figure 2.2d also shows that the difference in the shift of the size distribution of large drops is reduced.

Sensitivity experiments with different drop size distribution parameters are also conducted. Figures 2.3a–2.3c and 2.3d–2.3f are the same as Figures 2.1a–2.1c but with r_c = 8 μm and 12 μm, respectively. Corresponding initial drop number concentrations are 761 and 226 cm^{-3}, respectively. For r_c = 8 μm, the formation of large drops are substantially impeded in both the NQS and IQS models compared to the control experiments. The rapid mass transition from small drops to large drops occurs at t ~ 40 min, while it occurs at t ~ 25 min in the control experiments. The difference in the size distribution of large drops obtained using the two models is larger than that in the control experiments (Figure 2.3c compared to Figure 2.1c).

Figures 2.3d–2.3f show the results for r_c = 12 μm. The formation of large drops and the mass transition from small drops to large drops are considerably accelerated compared to the control experiments. The rapid mass transition from small drops to large drops is observed at t ~ 18 min. The difference in the size distribution of large drops obtained using the two models is smaller than that in the control experiments (Figure 2.3f compared to Figure 2.1c).

Figures 2.3g–2.3i and 2.3j–2.3l show the results for σ = 0.22 and 0.44, respectively. Because σ is the standard deviation of the initial drop size distribution that is given in a log-normal distribution, a larger σ indicates a more dispersed initial drop

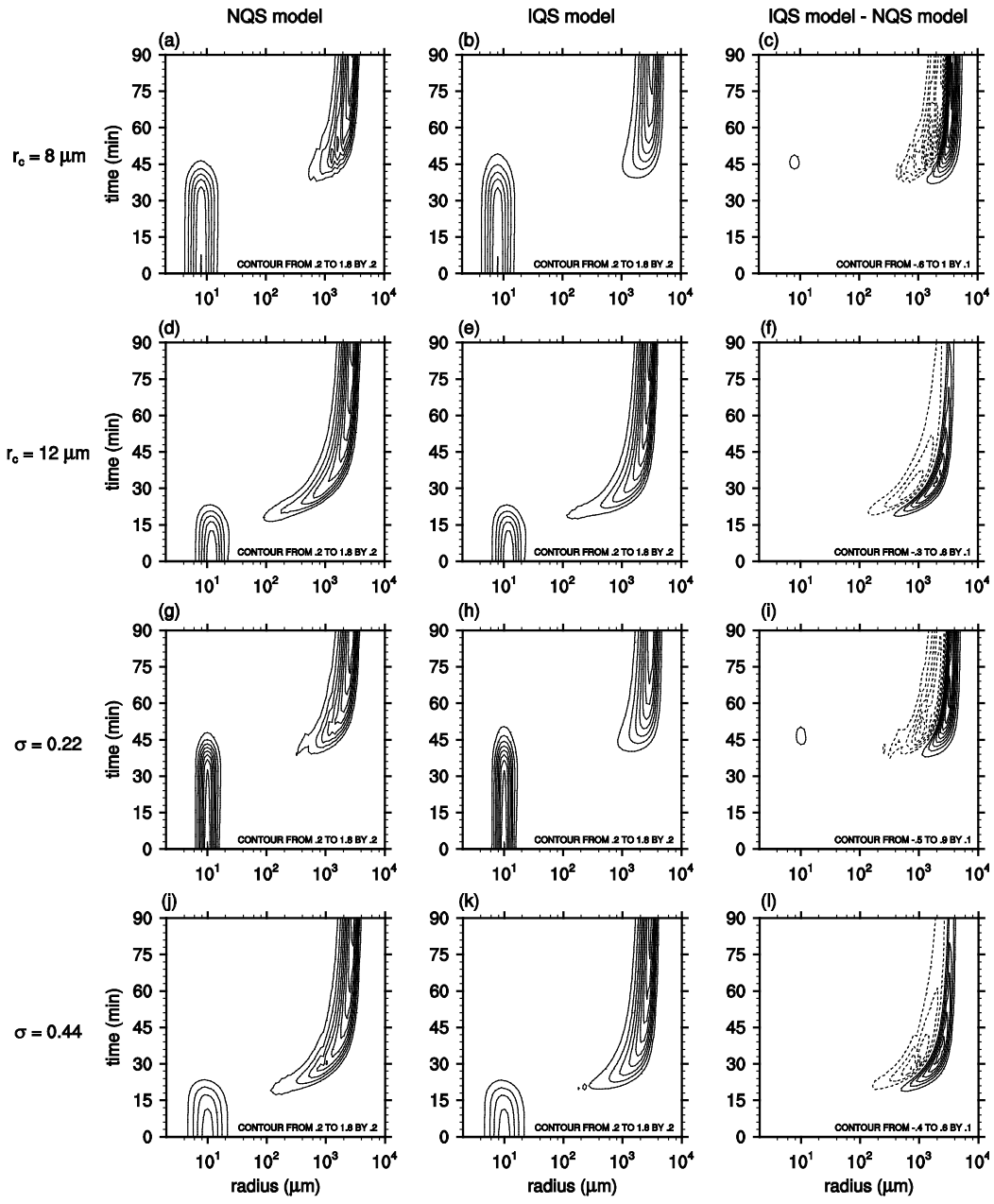

Figure 2.3. Same as in Figures 2.1a–2.1c but for the sensitivity experiments with varied r_c and σ. (a)–(c) are for the experiments with r_c = 8 μm, (d)–(f) are for the experiments with r_c = 12 μm, (g)–(i) are for the experiments with σ = 0.22, and (j)–(l) are for the experiments with σ = 0.44.

size distribution. Differences between the two models when the initial dispersion is relatively small are similar to those when the initial median drop size is relatively small (Figures 2.3c and 2.3i), and differences between the two models when the initial dispersion is relatively large are similar to those when the initial median drop size is relatively large (Figures 2.3f and 2.3l). The effect of the IQS model on the size distribution of large drops is larger in an environment in which the large drop formation is less favorable, which includes either smaller initial median drop size or smaller initial drop size dispersion.

Figure 2.4 shows the time series of the total mass of large drops in the control experiments and the other sensitivity experiments. In this figure, a large drop is defined using a critical radius of 1 mm. In all experiments, the IQS model accelerates large drop formation. Therefore, the IQS model affects not only the size distribution of large drops but also the time required for large drop formation. In contrast to the size distribution of large drops, however, the difference in the time required for large drop formation is larger when the large drop formation is more favorable (larger r_c or larger σ) than when the large drop formation is less favorable (smaller r_c or smaller σ).

It is known that an increase in aerosol number concentration induces a decrease in mean drop size at the early cloud development stage, hence causing a delay in large drop formation (e.g., Albrecht, 1989; Rosenfeld, 1999; Choi et al., 2014). In this study, it is shown that the difference in the time required for large drop formation caused by different initial median drop sizes is larger in the IQS model than in the NQS model. Therefore, it might be deduced that the IQS model somewhat amplifies the aerosol

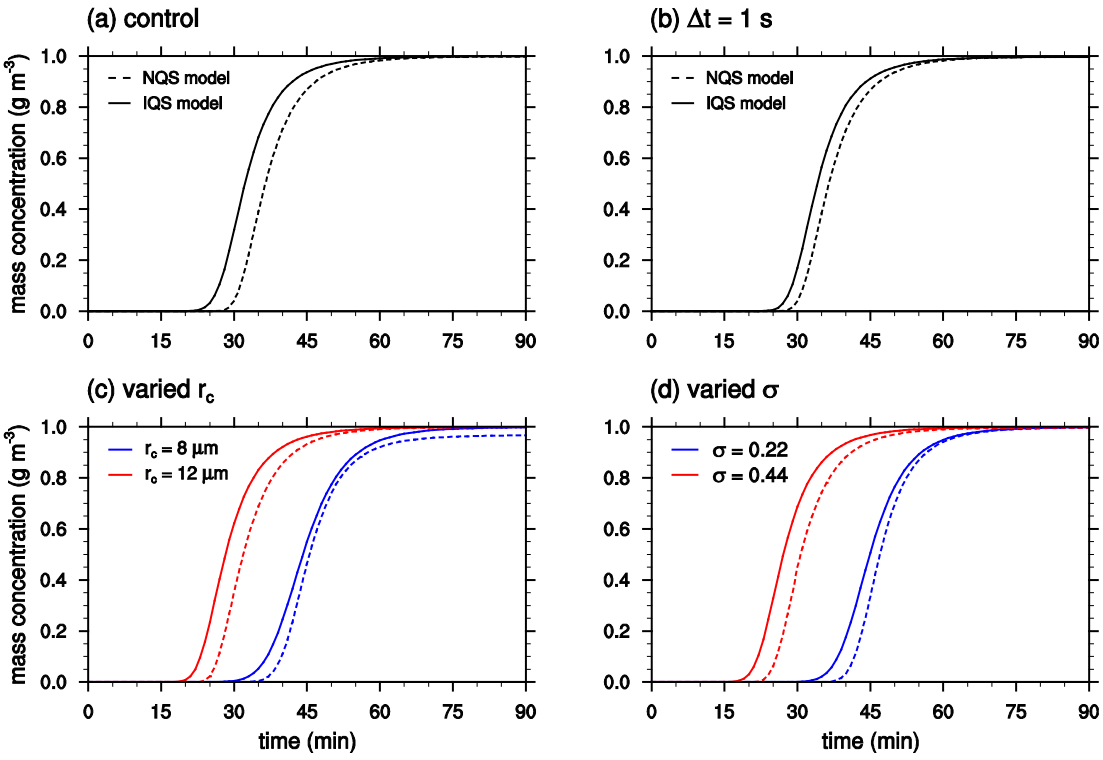

Figure 2.4. Time series of the total mass concentration of large drops (r > 1 mm) in (a) the control experiments, (b) the sensitivity experiments with Δt = 1 s, (c) the sensitivity experiments with r_c = 8 and 12 μm, and (d) the sensitivity experiments with σ = 0.22 and 0.44. In (c) and (d), dashed lines are the results of the NQS model and solid lines are the results of the IQS model.

effect that is known to delay large drop formation. However, because the aerosol effect related to the large drop formation is very complex in nature depending on various environmental conditions, careful approaches and in-depth studies are needed. The difference is larger with a larger model time step, as expected.

The difference in the time of large drop formation between the NQS and IQS models in this study is approximately a few minutes, from 1–2 min to ~5 min, which is much larger than a few seconds that is reported in Young (1975). The difference depends on the initial drop size distribution and the model time step

2.2.2 Cloud-resolving model

To examine the effects on cloud development and precipitation, the IQS model is implemented into a microphysics scheme, which is in Hebrew University Cloud Model (HUCM) that originally adopts the NQS model to solve the SCE. The microphysics scheme in HUCM uses a bin method; it represent each hydrometeor size distribution at each grid point and at each time instance using 43 mass-doubling bins. A detailed description of the microphysics scheme in HUCM is given in Khain et al. (2011). TICE proposed in Pinsky et al. (2008) that is considered in the box model is also taken into account in the microphysics scheme in HUCM.

The Weather Research and Forecasting (WRF) model version 3.6.1 (Skamarock et al., 2008) coupled with the microphysics scheme in HUCM (Lee and Baik, 2016) is used in this study. Numerical experiments that simulate a 2-D single warm cloud are conducted using the WRF model. The experimental setup is established following Lee

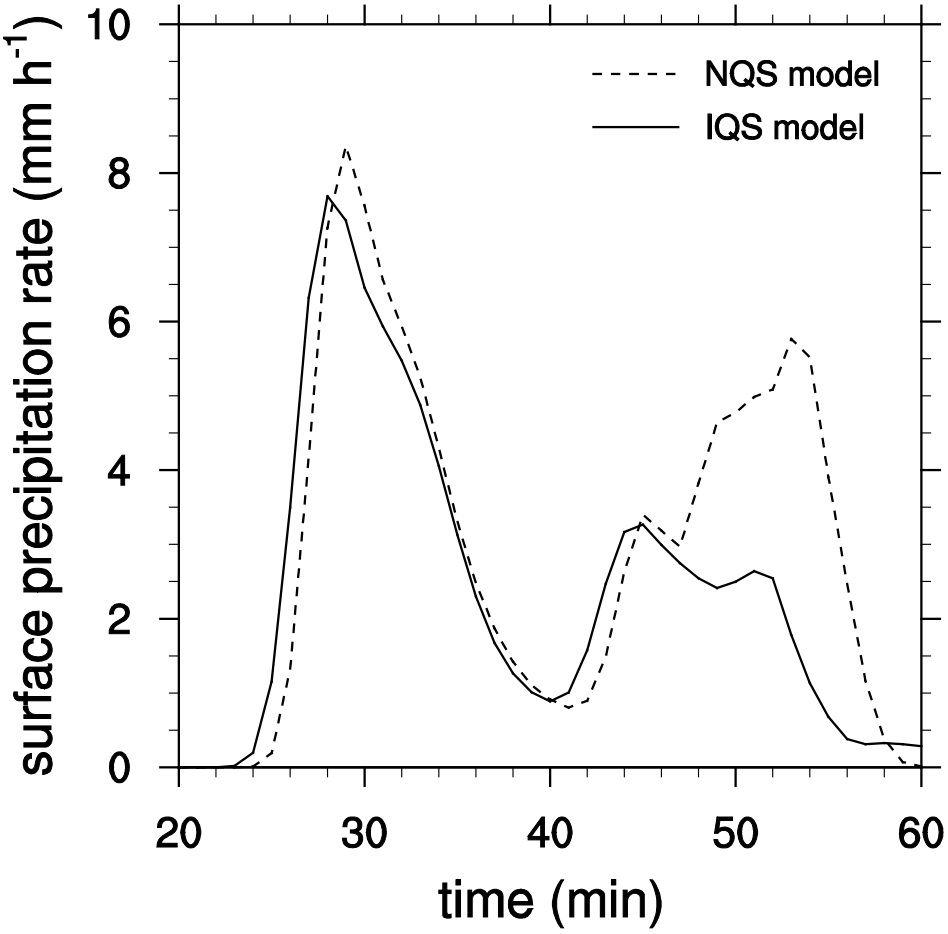

Figure 2.5. Time series of the surface precipitation rate averaged over x = 13–23 km in the NQS and IQS models.

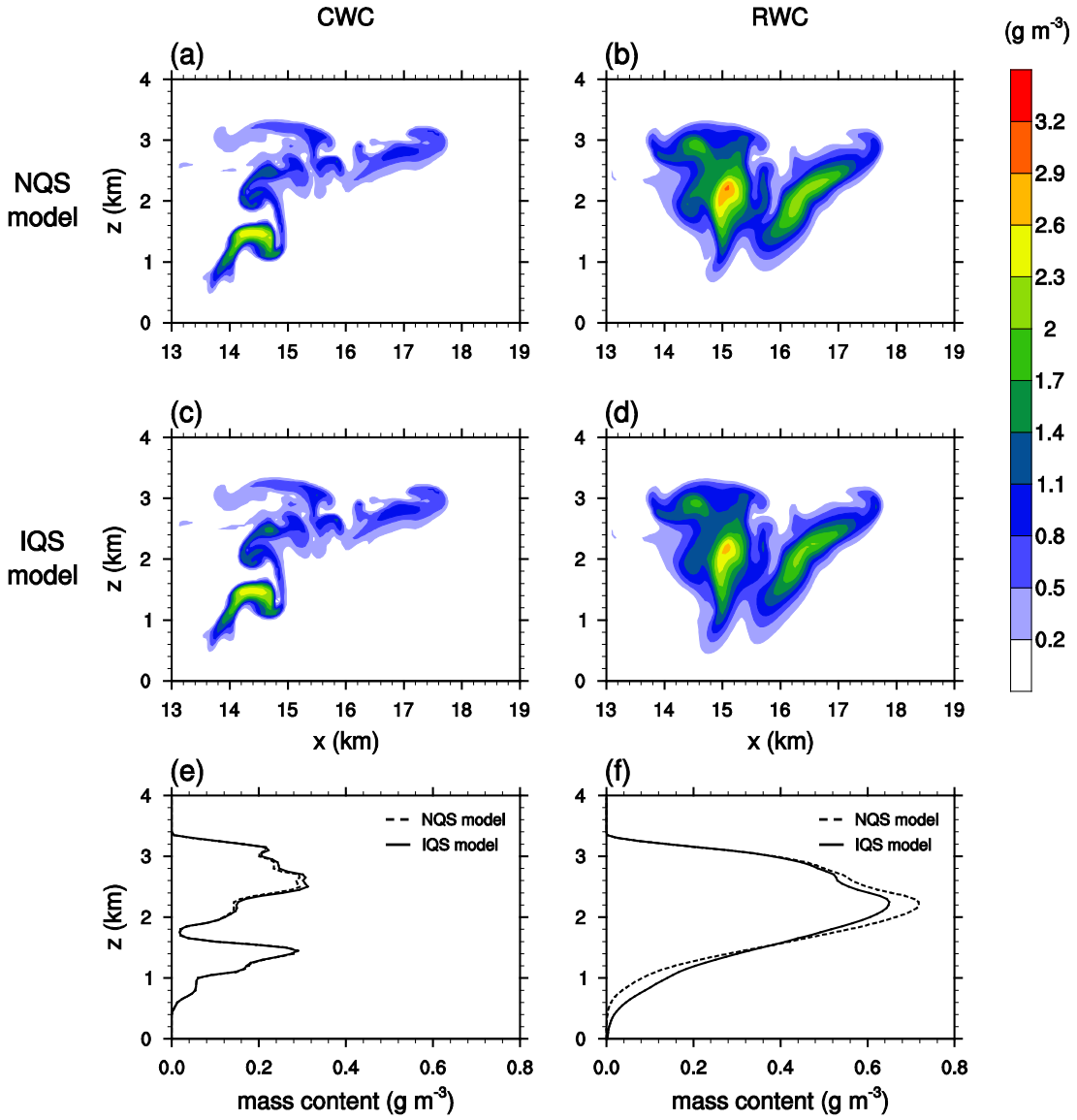

Figure 2.6. Fields of (a) cloud water content (CWC) and (b) rainwater content (RWC) at t = 23 min obtained using the NQS model. (c) and (d) same as (a) and (b), respectively, but for the IQS model. Vertical profiles of (e) CWC and (f) RWC averaged over x = 13–19 km at t = 23 min in the NQS and IQS models.

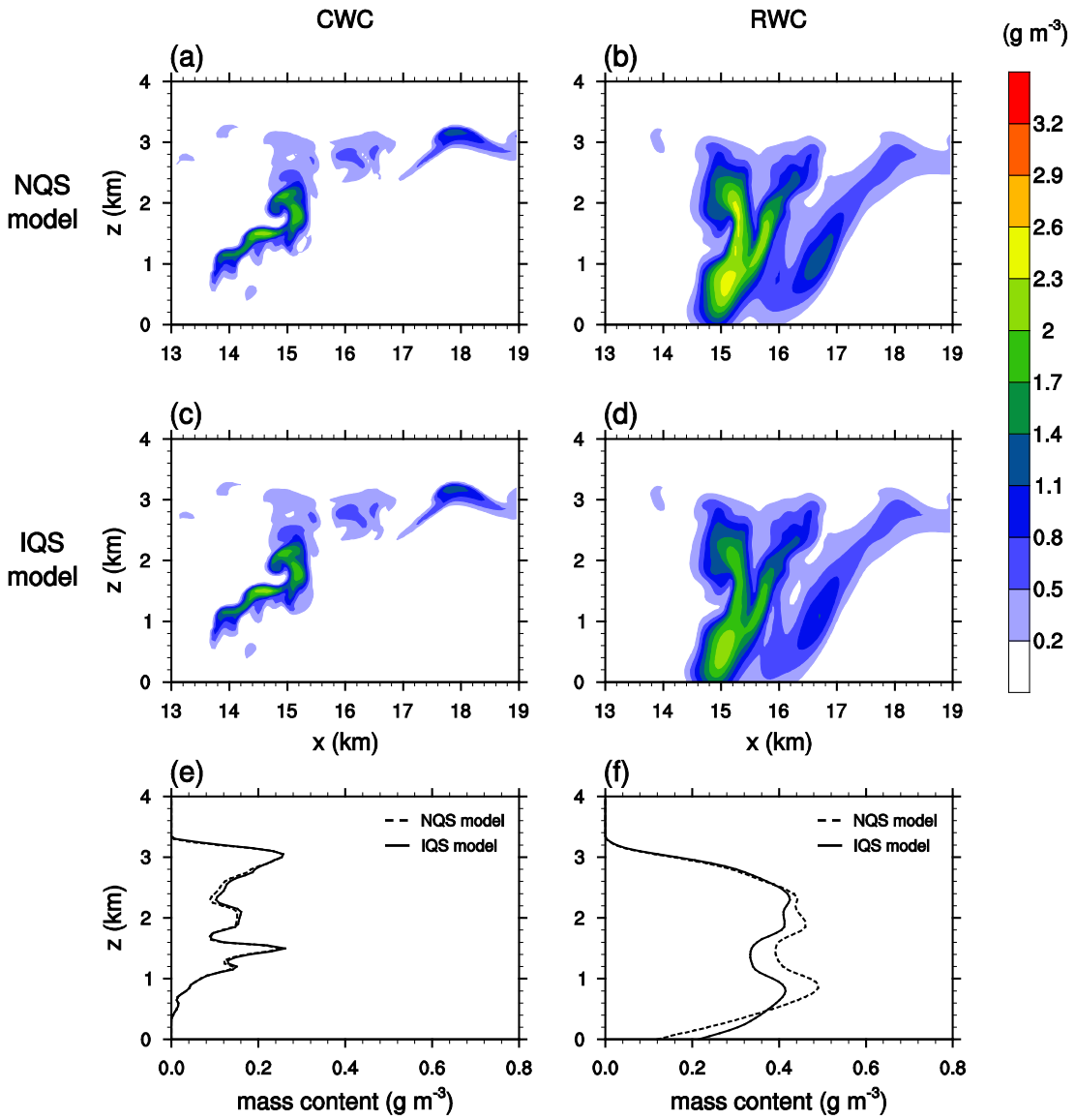

Figure 2.7. Same as in Figure 2.6 but at t = 26 min.

et al. (2015). The thermodynamic sounding used by Ogura and Takahashi (1973), which is characterized by a warm and humid environment and a strong capping inversion layer near z = 3 km, is adopted for simulations. The initial aerosol number concentration near the surface is set to 300 cm^{-3}. The model domain size is 51.2 km in the horizontal direction and 8 km in the vertical direction. The grid spacing is 50 m in both the horizontal and vertical directions. The model is integrated for 60 min with a time step of 1 s.

The time series of the surface precipitation rate averaged over the mostly cloudy area (x = 13–23 km in the model domain) in the NQS and IQS models are shown in Figure 2.5. While the overall precipitation patterns before t ~ 45 min are similar to each other, the surface precipitation starts earlier in the IQS model than in the NQS model by 1–2 minutes, which agrees with the box model results in chapter 2.2.1. This study demonstrates that the rigorous consideration of the finite model time step can affect not only the evolution of drop size distribution in the simple box model but also cloud development and precipitation in the complex cloud-resolving model. The time series of the surface precipitation rate in the two models exhibit a large difference after t ~ 45 min. As the first formed cloud is decaying, many small clouds form. Because they are largely affected by perturbed environmental conditions, it is difficult to argue that the difference after t ~ 45 min is caused by the IQS model, and a direct comparison between the results obtained using the two models after t ~ 45 min is not straightforward.

The spatial distributions of cloud water content (CWC) and rainwater content (RWC) are examined to investigate the effects of the IQS model on cloud development

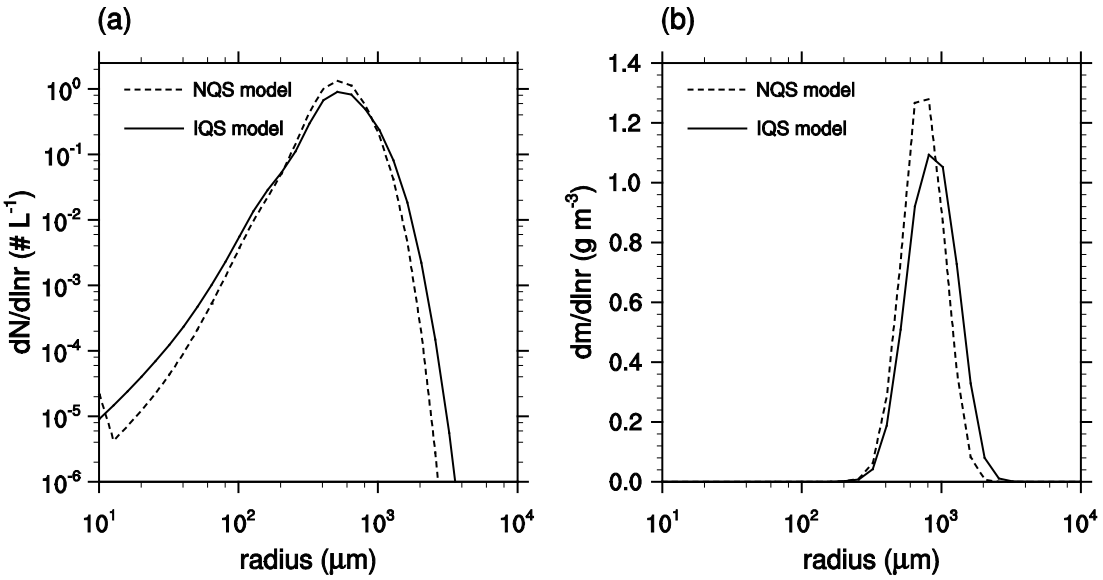

Figure 2.8. (a) The number- and (b) mass-size distributions of drops averaged over the area where $z < 0.5$ km and the rainwater mixing ratio ≥ 0.5 g kg^{-1} at $t = 27$ min in the NQS and IQS models.

and precipitation. Figure 2.6 shows the CWC and RWC fields and the vertical profiles of horizontally averaged CWC and RWC at t = 23 min. The difference in CWC between the two models is negligible (Figures 2.6a, 2.6c, and 2.6e) at this time, but the difference in RWC are observed (Figures 2.6b, 2.6d, and 2.6f). RWC in the layer z < 1.5 km is larger in the IQS model than in the NQS model. It is shown in the box model results that the IQS model accelerates large drop formation. The large drops that form earlier fall to the lower layer earlier, so RWC in the lower layer is larger in the IQS model than in the NQS model. Over time, the difference in CWC is still very small but the difference in RWC becomes clearer (see Figure 2.7). At t = 26 min (Figure 2.7), when the early surface precipitation rate is rapidly increasing, RWC in the layer z < 0.5 km is larger in the IQS model than in the NQS model, which results in the increased early surface precipitation amount in the IQS model. It is noted that RWC in the layer z = 0.5–2.5 km is smaller in the IQS model than in the NQS model mainly because of the early sedimentation of larger drops in the IQS model.

Figure 2.8 shows the drop size distributions averaged in the rain shaft area (where z < 0.5 km and the rainwater mixing ratio is larger than 0.5 g kg^{-1}) at t = 27 min in the NQS and IQS models. A wider spectrum of the number-size distribution of drops is seen in the IQS model (Figure 2.8a), which results from the Poisson distribution. The mass-size distributions of drops show that the large drops in the IQS model tend to have larger sizes than those in the NQS model, which is similar to the result of the box model (Figures 2.1d and 2.2d).

2.3. Summary and conclusions

In this study, the IQS model, which is derived by rigorously considering a finite model time step for solving SCE, was examined and compared with the NQS model. In the IQS model, the probability that a large collector drop collides with a small collected drop follows the Poisson distribution with respect to the number of collisions.

Using a box model that takes the TICE into account, it was shown that the IQS model tends to increase the sizes of large drops and accelerates the large drop formation compared to the NQS model. This is because some large collector drops are allowed to have more chances to collide with small collected drops in the IQS model. The size distribution of large drops becomes wider, which also enhances collisions. Our box model results suggest that the IQS model can partially explain the drop growth across so-called the size gap, typically referring to a radius range between ~15 and ~40 μm (Beard and Ochs, 1993; Grabowski and Wang, 2013). The effects of the IQS model depend on the model time step and the shape of initial drop size distribution. Because the IQS model considers collision of drops in the model time step, the effects are smaller when the model time step is smaller. The shift in the size distribution of large drops is larger when the collisional growth of drops is less favorable, but the acceleration of larger drop formation is larger when the collisional growth of drops is more favorable. The accelerated large drop formation by the IQS model that is larger in the situation in which the collisional growth of drops is more favorable implies that the aerosol effect that is known to delay the large drop formation could be somewhat increased in the IQS model. The acceleration of the drop size distribution evolution

caused by the IQS model is a few minutes, which is much larger than that reported in Young (1975). The IQS model was incorporated into a cloud-resolving model that uses a detailed bin microphysics scheme, and a single warm cloud was simulated. It was shown that the onset of surface precipitation is accelerated in the IQS model, which agrees with the box model result.

It would be interesting to investigate the effects of the IQS model on mixed-phase cloud development and precipitation under idealized environmental conditions. In real environments, the effects of the IQS model on clouds and precipitation could be very complex but positive impacts on precipitation prediction are expected. This deserves an in-depth investigation through the simulations of many real cases.

3. Evaluation of an improved quasi-stochastic collection model through precipitation prediction over north central Mongolia

3.1. Introduction

Numerical models that resolve cloud and precipitation processes explicitly on grid scale have been increasingly used to better understand moist convection and accurately predict precipitation. They are categorized into numerical models that include bulk microphysics schemes, hereafter called bulk models, and numerical models that include bin microphysics schemes, hereafter called bin models (Houze, 2014; Khain et al., 2015). Bulk and bin models share common characteristics. For example, both the models usually classify hydrometeors into similar types (e.g., drops, cloud ice/crystals, snow, and graupel). However, bulk and bin models adopt fundamentally different approaches in the way they treat cloud microphysical processes, particularly in describing the size distribution of hydrometeors. In bulk models, the size distribution of precipitation particles is assumed to have a specific form (e.g., Marshall-Palmer distribution or gamma distribution). One-moment bulk models predict the mixing ratios of hydrometeors (e.g., Kessler, 1969; Lin et al., 1983), and two-moment bulk models predict the mixing ratios and number concentrations of hydrometeors (e.g., Seifert and Beheng, 2006; Lim and Hong, 2010). On the other hand, in bin models, the entire mass

range of each hydrometeor is divided into discrete mass bins and the number concentration of each hydrometeor in each bin is predicted (e.g., Khain et al., 1996; Lynn et al., 2005a; Iguchi et al., 2012).

Bin models require much more computing times but represent microphysical processes more reliably than bulk models (Sato et al., 2009; Khain et al., 2015). Most numerical models and all the operational weather forecasting models have adopted bulk microphysics schemes. Recently, however, many studies have been performed to simulate moist convection and weather using bin models. Lynn et al. (2005a; 2005b) showed that the bin model simulates the rate and distribution of precipitation caused by mesoscale convection better than the bulk model. Iguchi et al. (2012) simulated a real case of shallow convective clouds and precipitation behind a cold front and obtained results from the bin model that are closer to the observation than those from the one-moment bulk model.

Many microphysical processes such as nucleation, vapor diffusion, freezing, melting, collision, breakup, and sedimentation are included in bin microphysics schemes. Among them, the collision process plays a key role in the growth of cloud particles (Pruppacher and Klett, 1997). To describe the collisional growth of cloud particles, a quasi-stochastic collection equation that considers the stochastic concept (Telford, 1955; Berry, 1967) is utilized. Traditional quasi-stochastic models assume that the time step is infinitesimally small, so that a cloud particle can collide with other cloud particle only once within the time step and the average number of collisions is interpreted as a collision probability (Gillespie, 1972). However, since the time step

used is finite, a cloud particle can collide with other cloud particle more than once within the time step. As a next research step, it would be meaningful to examine differences in surface precipitation when the improved quasi-stochastic collection (IQS) and the normal quasi-stochastic collection (NQS) models are compared through real-case prediction and find reasons for the differences. A small change in cloud microphysics in a three-dimensional model with full physics can sometimes result in large or noticeable changes in surface precipitation through complex nonlinear interactions between cloud microphysics and dynamics.

The aims to evaluate the IQS model against the NQS model in precipitation prediction. For this, a numerical model coupled with an updated bin microphysics scheme is used to simulate a precipitation event observed in north central Mongolia. In chapters 3.2 and 3.3, the observational analysis for this precipitation event is given and the numerical model and the experimental setup are described. In chapter 3.4, the model is validated and the results from the IQS and NQS models are presented and discussed, particularly focusing on the impacts of the improvement in the quasi-stochastic model on clouds and precipitation. A summary and conclusions are given in chapter 3.5.

3.2. Observational analysis

On 21 August 2014, a precipitation event took place in north central Mongolia. The amount of daily accumulated surface precipitation from 00 UTC 21 to 00 UTC 22 was 30 mm in Ulaanbaatar, capital of Mongolia, and 19 mm in Darkhan. The two locations are indicated in Figure 3.1. The daily accumulated surface precipitation

amount of ~20–30 mm can be regarded as a special event in Mongolia considering that the average annual precipitation amount in Mongolia is ~210 mm (Dagvadorj et al., 2014).

The synoptic-scale features associated with the precipitation event are analyzed using the ERA-Interim reanalysis data (Dee et al., 2011). Figure 3.1 shows the mean sea-level pressure and 850-hPa temperature fields, and Figure 3.2 shows the 500-hPa geopotential height and 200-hPa horizontal wind fields. Analysis times are at 12 UTC 20, 00 UTC 21, 12 UTC 21, and 00 UTC 22 August 2014. At 12 UTC 20, a cold high is located north of Mongolia and a warm low is located south of Mongolia (Figure 4.1a). An upper-level cold low that is associated with the low-level cold high exists, and the polar jet streams along the border of the upper-level cold low (Figure 3.2a). For the next 12 h, the low-level cold high moves southeastward and the low-level warm low changes little in its position (Figure 3.1b). The flow of the polar jet is strengthened in the north-south direction (Figure 3.2b). At 00 UTC 21, the 500-hPa geopotential height at the center of the upper-level cold low is 5490 m.

The low-level warm low moves northeastward from 00 UTC 21 to 12 UTC 21 and is located southeast of Ulaanbaatar at 12 UTC 21 (Figure 3.1c). In the meanwhile, the low-level cold high moves southeastward. The gradients of pressure and temperature are enhanced so a cold front is developed near Darkhan. In the upper layer, the cold low moves eastward, the vorticity of the cold low increases, and the flow of the polar jet is

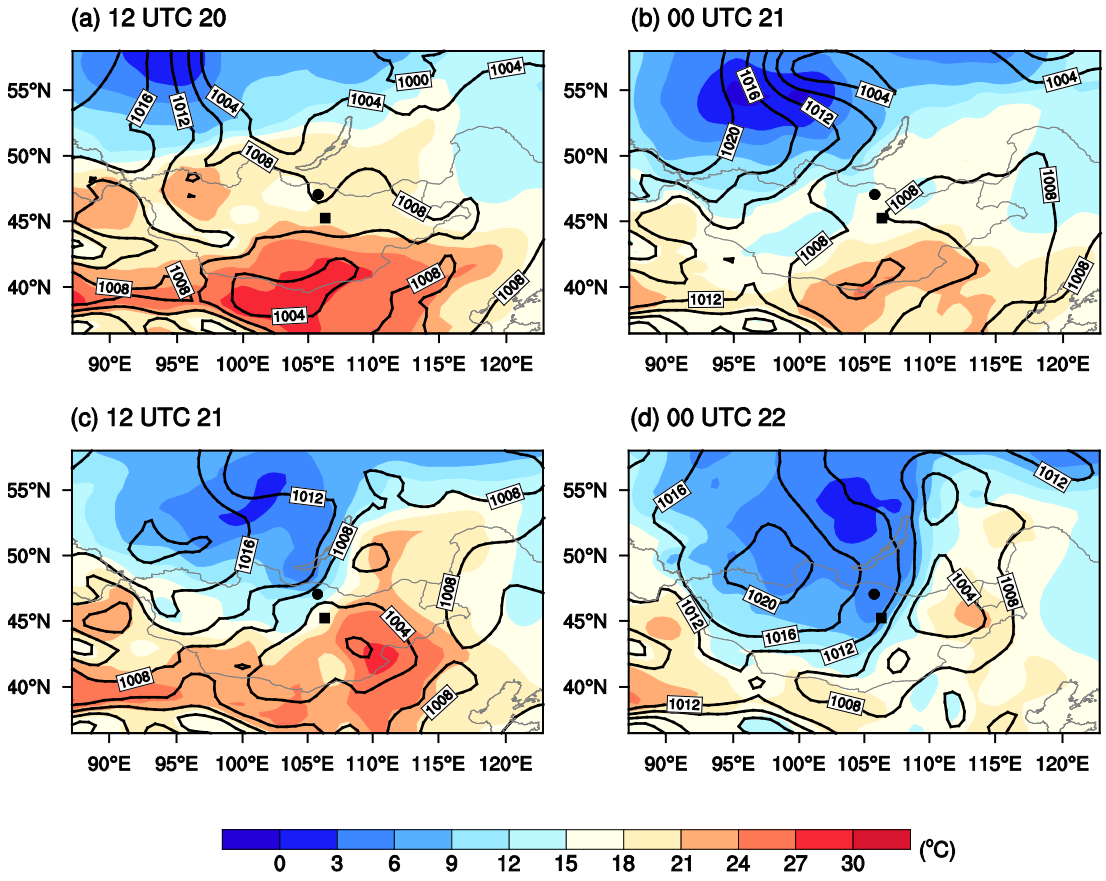

Figure 3.1. Mean sea-level pressure (hPa, black solid lines) and 850-hPa temperature (color shaded) fields at (a) 12 UTC 20, (b) 00 UTC 21, (c) 12 UTC 21, and (d) 00 UTC 22 August 2014 from the ERA-Interim reanalysis data. The locations of Darkhan and Ulaanbaatar observatories are denoted by the small circle and small square in each frame, respectively

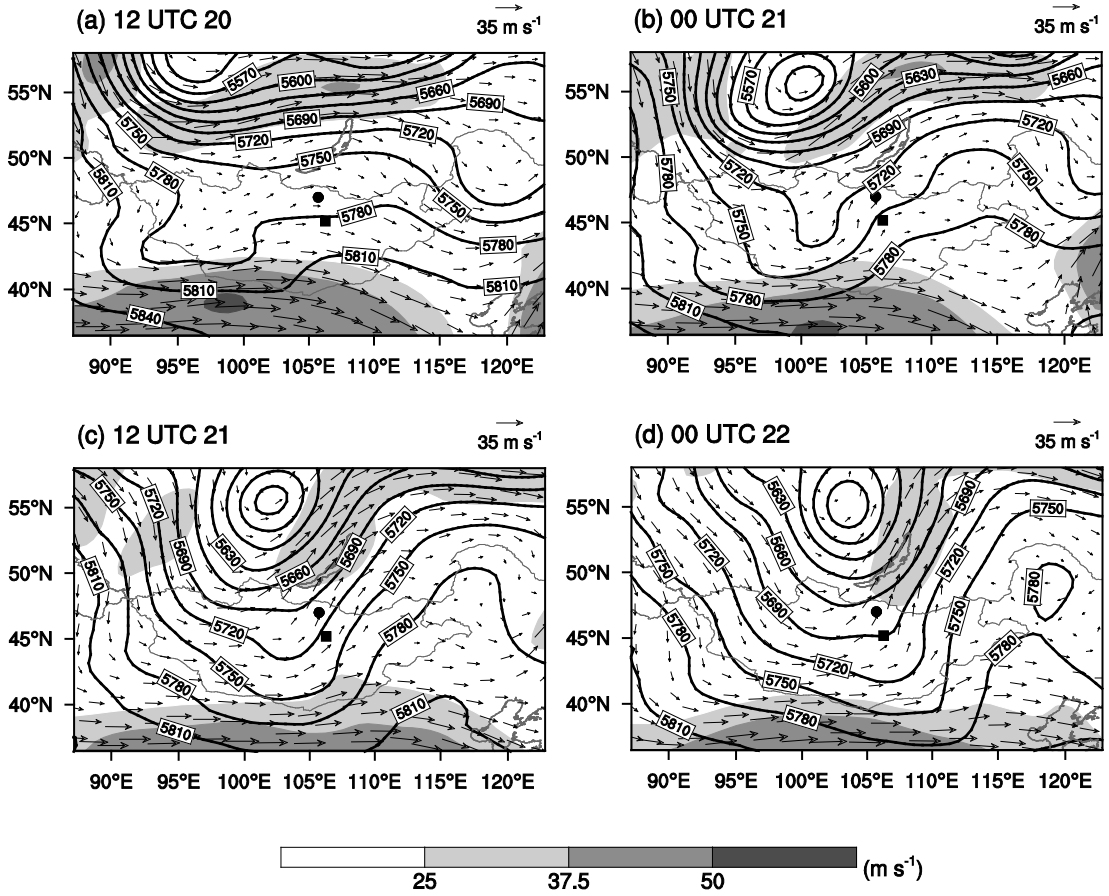

Figure 3.2. Same as in Figure 1 but for 500-hPa geopotential height (m, black solid lines) and 200-hPa horizontal wind vector and speed (shaded).

further strengthened in the north-south direction (Figure 3.2c). As the cold low and the polar jet move eastward during this period, the entrance of the polar jet is located northwest of Darkhan at 12 UTC 21. At this time, the low-level warm low is located on the right side of the entrance of the upper-level jet. Accordingly, the vertical motion is strengthened and the low-level warm low is developed: the pressure at the center of the low-level warm low.at 12 UTC 21 is lower compared to the previous time. The minimum mean sea-level pressure of the low-level warm low at 12 UTC 21 is 999 hPa. It is noted that at the cold front the isobars are generally parallel to the isotherms. From 12 UTC 21 to 00 UTC 22, the low-level cold high is further extended southeastward (Figure 3.1d). At 00 UTC 22, the cold front had passed through Darkhan. The low-level warm low moves further northeastward during this period.

Figure 3.3 shows the time series of 2-m temperature, 2-m dew-point temperature, 2-m relative humidity, and 10-m wind speed and direction observed at Darkhan observatory. From ~10 UTC 21 August, the temperature and dew-point temperature drop rapidly and the relative humidity increases abruptly in 1–2 hours. For the 2-h period of 10–12 UTC, the decrease in 2-m temperature is 6.5°C and the increase in 2-m relative humidity is 38%. The wind speed after ~10 UTC is stronger than that before ~10 UTC, and the wind direction after ~10 UTC is little changed (northwesterly). These features are evidence for the passage of the cold front at ~10 UTC at Darkhan.

Figure 3.4 shows the enhanced infrared (IR) imageries of COMS (Communication, Ocean and Meteorological Satellite) operated by the Korea

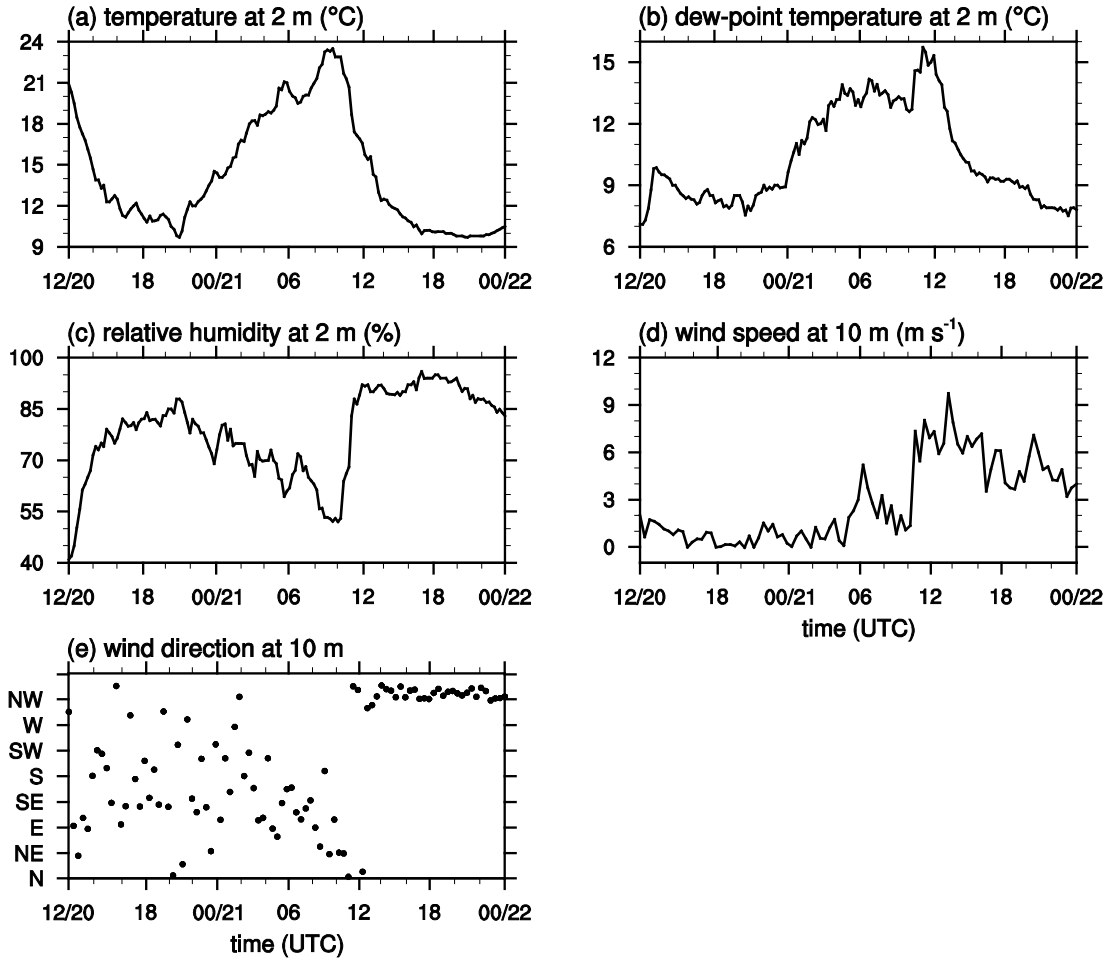

Figure 3.3. Time series of (a) temperature at 2 m, (b) dew point temperature at 2 m, (c) relative humidity at 2 m, (d) wind speed at 10 m, and (e) wind direction at 10 m from 12 UTC 20 to 00 UTC 22 August 2014 observed at Darkhan observatory.

Meteorological Administration at times before and after the cold front passage at Darkhan. At 0700 UTC (before the passage of the cold front at Darkhan), small convective cells are widespread in north central Mongolia (Figure 3.4a). These convective cells are associated with the low-level warm low located in the southern part of Mongolia (Figures 3.1b and 3.1c). The small convective cells are organized into large convective cells as the low-level warm low is intensified under the favorable environmental conditions (the cold front, polar jet, and upper-level vorticity). At 0845 UTC, the large convective cells are observed (Figure 3.4b). At 1030 UTC, shortly after the passage of the cold front at Darkhan, the convective cells are further organized and developed. For the next ~3 hours, the convective cells maintain their strength and move northeastward slowly (Figures 3.4c–3.4e). At 1530 UTC, the convective cells becomes weak.

Figure 3.5 shows the radiosonde-observed temperature and dew-point temperature profiles at 12 UTC 20, 12 UTC 21, and 00 UTC 22 August 2014 observed at Ulaanbaatar observatory. At 12 UTC 20, the convective available potential energy (CAPE) is 47 J kg^{-1}. This value is small compared to typical values for strong convection. At 12 UTC 21 (after the cold front passage at Ulaanbaatar), the air is almost saturated up to ~200 hPa and the CAPE is as small as 6 J kg^{-1}. At 00 UTC 22, the air is still saturated up to ~500 hPa and the decrease in upper-layer temperature is not so large, which reflects the parallel alignment of isotherms and isobars (Figure 3.1d). This type of cold front is known to often cause a relatively long-lasting surface precipitation (Bluestein, 1993).

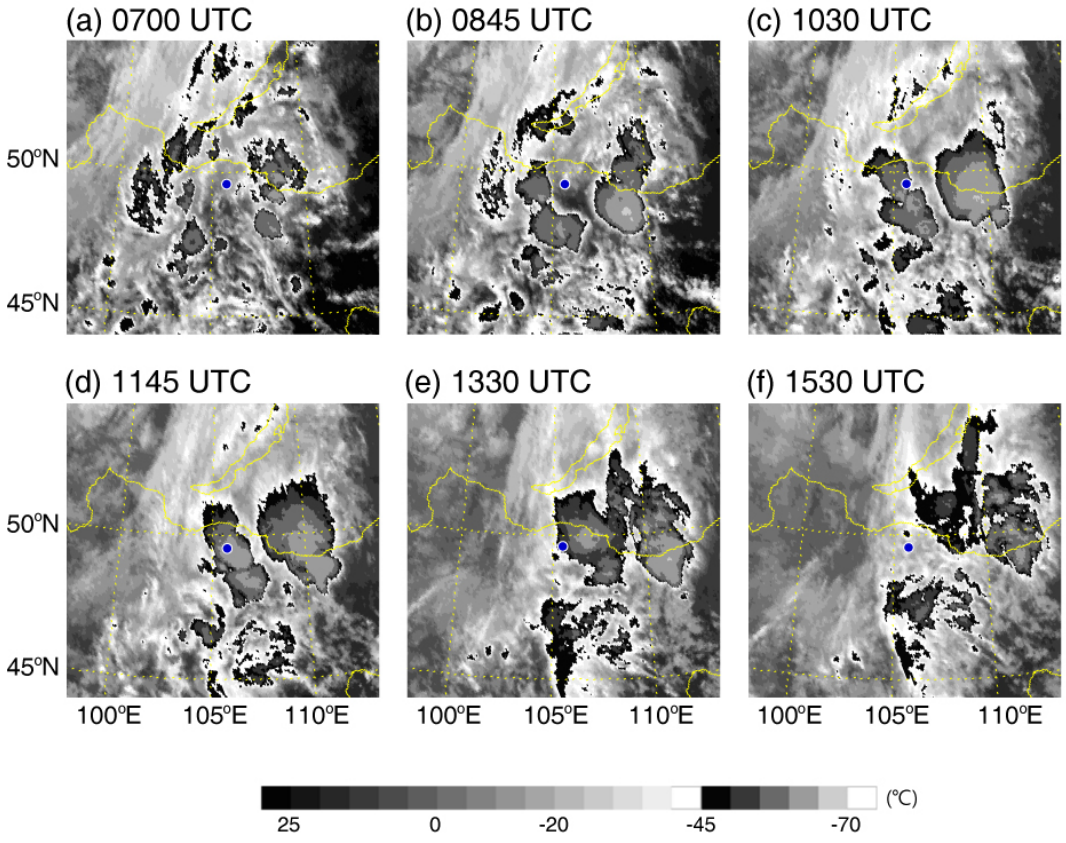

Figure 3.4. Enhanced infrared (IR) imageries of COMS (Communication, Ocean and Meteorological Satellite) over north central Mongolia at (a) 0700, (b) 0845, (c) 1030, (d) 1145, (e) 1330, and (f) 1530 UTC 21 August 2014. The location of Darkhan observatory is denoted by the small blue circle in each frame.

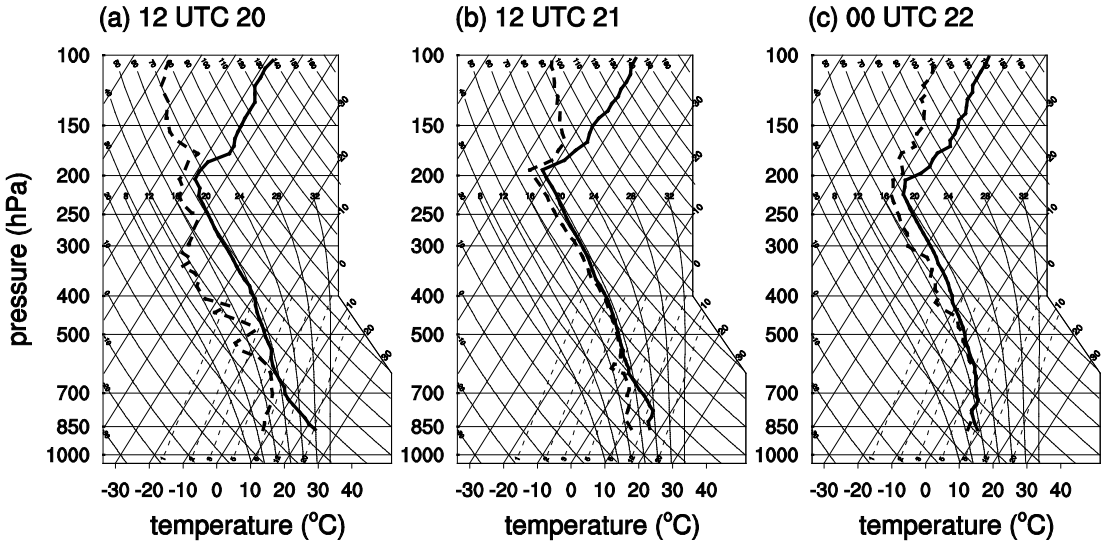

Figure 3.5. Soundings of temperature (solid thick line) and dew point temperature (dashed thick line) on skew *T*-log *p* diagram at (a) 12 UTC 20, (b) 12 UTC 21, and (c) 00 UTC 22 August 2014 at Ulaanbaatar.

3.3. Model description and experimental setup

To numerically simulate the precipitation event described above, the Weather Research and Forecasting (WRF) model v3.7.1 (Skamarock et al., 2008) is used. The bin microphysics scheme of the Hebrew University Cloud Model (HUCM) is implemented in the WRF model (Lee and Baik, 2016; 2017). The bin microphysics scheme used in this study considers seven hydrometeor types (liquid drop, three ice crystals (column, plate, and dendrite), snow, graupel, and hail) and aerosol. The bin microphysics scheme uses 43 mass-doubling bins to describe the size distributions of each hydrometeor and aerosol. To consider the gradual melting of large ice particles, the liquid fractions of snow, graupel, and hail are predicted (Phillips et al., 2007). The rimed fraction of snow is also predicted and used to calculate the properties of snow (density and terminal velocity). A simple breakup parameterization of large snow particles (Khain et al., 2011) is incorporated. In the present study, the turbulence-induced collision enhancement is not considered. A more description of the bin microphysics scheme is given in Khain et al. (2011) and Lee and Baik (2016).

Compared to Lee and Baik (2017), the bin microphysics scheme is further improved by considering the IQS model in which the multiple collisions of cloud particles within a time step is allowed. If collisions of cloud particles in the *i* th and *j* th bins are considered, the rate of the change of number concentration is given as

$$\Delta n_i = \Delta n_j = -n_i n_j K_{ij} \Delta t, \tag{3.1}$$

where n_i and n_j are the number concentrations of cloud particles in the i th and j th bins, respectively, K_{ij} is the collection kernel between the i th and j th bins, and Δt is the time step. The NQS model assumes an infinitesimally small time step within which a cloud particle either collides with other cloud particle once or does not collide. However, since the time step used is not infinitesimally small but finite, a cloud particle can collide with other cloud particle more than one time. When multiple collisions within a finite time step are rigorously considered, the probability of the number of collisions in the IQS model is given as a Poisson distribution form

$$P(x) = \frac{p^x e^{-p}}{x!}, \tag{3.2}$$

where x is the number of collisions and p is the average number of collisions (e.g., $p = n_j K_{ij} \Delta t$ for cloud particles in the i th bin in (3.1)). In the IQS model, the average number of collisions is the same as that in the NQS model but some cloud particles have a chance to collide with other cloud particle more than one time within a time step. That is, in the NQS model, only $P(0)$ and $P(1)$ are not zero, which are $1 - p$ and p, respectively. On the other hand, in the IQS model, the summation of $P(x)$ from $x = 0$ to ∞ is 1 and the expectation value of x is p but $P(x)$ with $x \geq 2$ have also certain non-zero values. Note that the Poisson approach in the IQS model is not applied to the collisional breakup process.

Two one-way nested domains are considered (Figure 3.6). The horizontal grid

size is 5 km in the inner domain (domain 2 in Figure 3.6) and 15 km in the outer domain (domain 1 in Figure 3.6). The model top is 50 hPa (~20 km), and the number of vertical layers is 41. To provide initial and boundary conditions in the outer domain, the ERA-Interim data (Dee et al., 2011) are used. The radiation scheme (Iacono et al., 2008) is used for the parameterization of shortwave and longwave radiation, the YSU scheme (Hong et al., 2006) for the parameterization of the planetary boundary layer, and the Kain-Fritsch scheme (Kain, 2004) for the parameterization of subgrid-scale cumulus convection which is applied only to the outer domain. The Noah land surface model (Chen and Dudhia, 2001) is used. The initial aerosol number concentration (here, initial cloud condensation nucleus (CCN) number concentration at 1% supersaturation) is set to 300 cm^{-3} near the surface, and the size distribution of aerosol is set to follow the Köhler equation (Köhler, 1936) and the Twomey equation (Twomey, 1959). The WRF model is integrated for 36 h starting from 12 UTC 20 August 2014. The time step used is 20 s in the inner domain and 60 s in the outer domain.

3.4. Results and discussion

3.4.1. Model validation

Before comparing the results of the IQS and NQS models in predicting the precipitation event, the simulations are validated using observation data. Figure 3.7 shows the mean sea-level pressure and 850-hPa temperature fields (left column) and

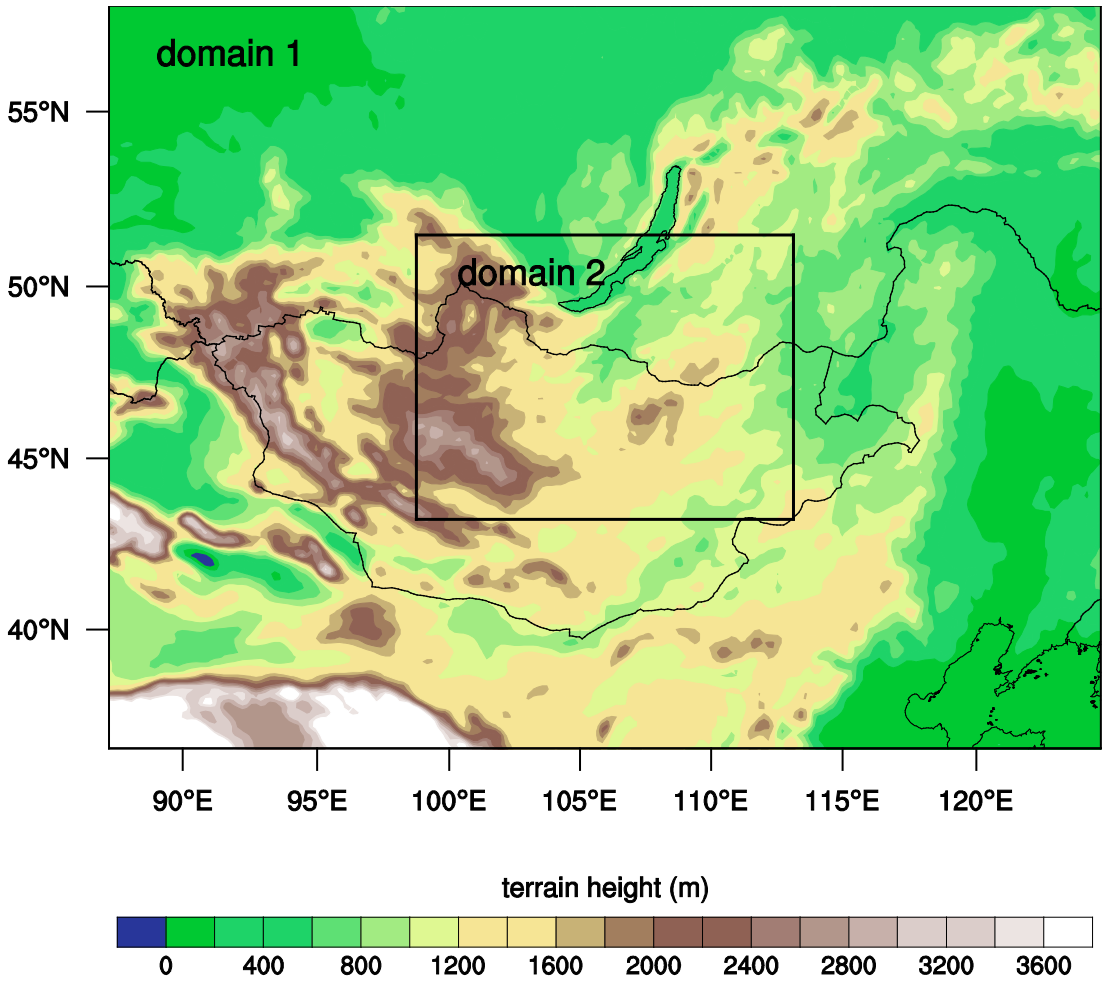

Figure 3.6. Two nested computational domains and terrain height.

500-hPa geopotential height and 200-hPa wind fields (right column) at 00 UTC 21, 12 UTC 21, and 00 UTC 22 August 2014 in the IQS model. The simulated synoptic features in the NQS model are very similar to those in the IQS model. The comparison of the observation (reanalysis data) and simulation (Figures 3.1, 3.2, and 3.7) indicates that the model well simulates the structure and evolution of the synoptic features that are associated with the precipitation event as described in chapter 3.1: the movement of the low-level warm low, the enhanced north-south directed flow in the polar jet, the increased vorticity of the upper-level cold low, and the proper locations of the polar jet and the low-level warm low.

Figures 3.8a–3.8c show the distributions of the observed and IQS model-simulated surface precipitation amount in the domain from 00 UTC 21 to 00 UTC 22 August 2014. The observation data are from the Integrated Multi-satellite Retrievals for GPM (IMERG), where GPM stands for Global Precipitation Measurement, (Figure 3.8a) and the National Agency for Meteorology and Environment Monitoring (NAMEM) of Mongolia (Figure 3.8b). The difference in 24-h accumulated surface precipitation amount between the IQS and NQS models is presented in Figure 3.8d. The IMERG dataset used in this study is version 03D and multi-satellite precipitation estimate with gauge calibration (final run) and has a horizontal resolution of 0.1º and a temporal resolution of half an hour (Huffman et al., 2015). Since many parts of the study area are remote mountainous areas, the number of meteorological observatories (32) is not large enough to obtain precipitation distribution fields in high spatial resolution. To compare all the precipitation data at same spatial resolution, an area average over 0.5º×0.5º is

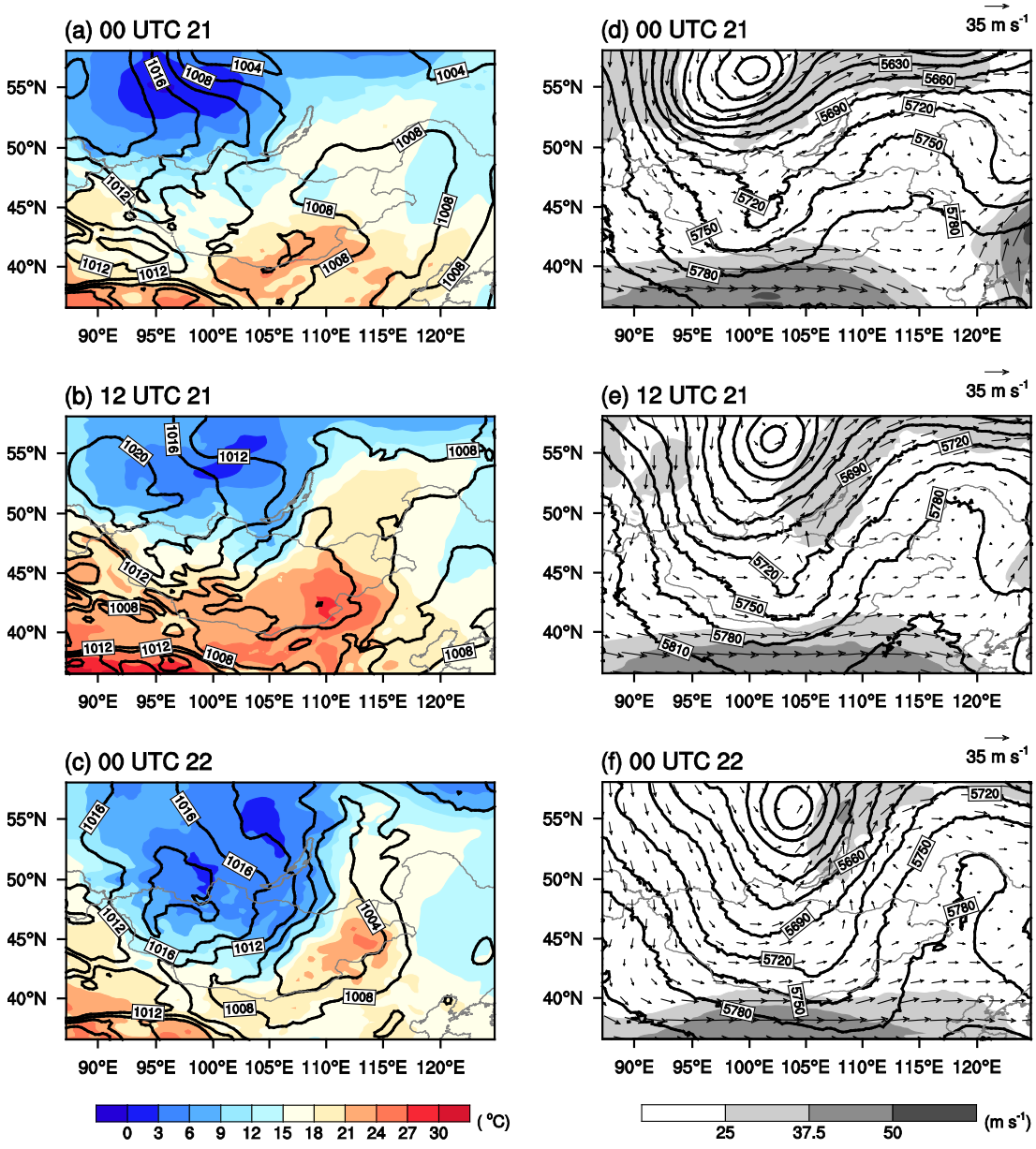

Figure 3.7. Mean sea-level pressure (hPa, black solid lines) and 850-hPa temperature (color shaded) fields at (a) 00 UTC 21, (b) 12 UTC 21, and (c) 00 UTC 22 August 2014 in the IQS model. (d)–(f) are the same as (a)–(c) but for 500-hPa geopotential height (m, black solid lines) and 200-hPa horizontal wind vector and speed (shaded).

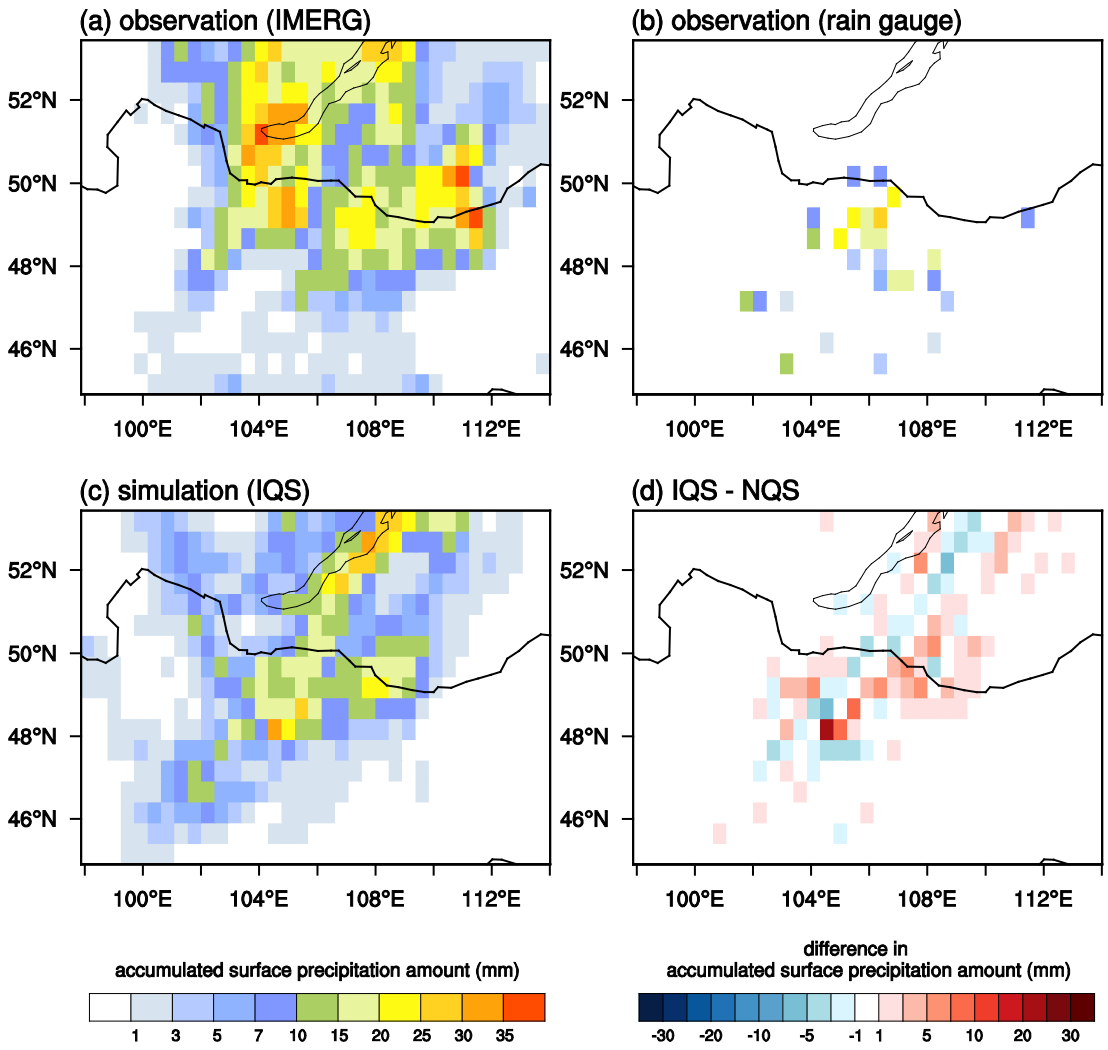
(a) observation (IMERG)
(b) observation (rain gauge)
(c) simulation (IQS)
(d) IQS - NQS
52°N
50°N
48°N
46°N
100°E
104°E
108°E
112°E
accumulated surface precipitation amount (mm)
1 3 5 7 10 15 20 25 30 35
difference in
accumulated surface precipitation amount (mm)
-30 -20 -10 -5 -1 1 5 10 20 30

Figure 3.8. Distributions of accumulated surface precipitation amount from 00 UTC 21 to 00 UTC 22 August 2014: (a) Integrated Multi-satellite Retrievals for GPM (IMERG) data, (b) rain gauge data from the National Agency for Meteorology and Environment Monitoring (NAMEM) of Mongolia, and (c) the IQS model simulation. (d) Difference in accumulated surface precipitation amount between the IQS model and the NQS model. Note that (b) is constructed using rain gauge data at 32 meteorological observatories. In (b), the areas with white color stand for no precipitation, 24-h accumulated surface precipitation amount smaller than 1 mm, or the absence of observation.

considered (Figure 3.8). The simulation result (Figure 3.8c) exhibits a strong precipitation band along the northeast-southwest direction across the center region of the domain including Darkhan, some of this feature being revealed in the rain gauge data. This strong precipitation band is consistent with the direction of the cold front in Figure 3.1c. Moreover, another relatively strong precipitation is simulated east of Darkhan, which is associated with the low-level warm low ahead of the cold front (see Figures 3.1b and 3.1c).

It is seen from Figure 3.8d that the deviation of the IQS model from the NQS model is to a large extent positive in the domain, particularly at and near Darkhan, although an alternating pattern (i.e., spatial shifts) is seen. Because the IQS (also NQS) model tends to underestimate the 24-h accumulated surface precipitation amount compared to the IMERG data, in this regard, this positive deviation partially alleviates the negative bias of the NQS model. In spite of the uncertainty of the IMERG data and the insufficient spatial coverage of the rain gauge data, it seems that the IQS model improves over the NQS model by taking account of multiple collisions of cloud particles.

It is noted that IMERG data are based upon the combined analysis of intermittent satellite measurements and limited rain gauge measurements. Thus, it may be relatively not good to calculate and discuss bias and error due to large uncertainty in the accumulated surface precipitation amounts, although the temporal and spatial patterns of surface precipitation are relatively good to be discussed. Keeping this in mind, the root-mean-square error of 24-h accumulated surface precipitation amount is

calculated using the simulation data of the IQS and NQS models and the rain gauge data. The simulation data are bi-linearly interpolated to the locations of meteorological observatories. The root-mean-square error is 9.2 mm in the IQS model and 10.2 mm in the NQS model, showing an improvement of the IQS model over the NQS model. Also, the deviation of simulated 24-h accumulated surface precipitation amount from the rain gauge data is calculated. The mean deviation is –6.0 mm in the IQS model and –6.5 mm in the NQS model, indicating that both the models underestimate 24-h accumulated surface precipitation amount, but the prediction performance is better in the IQS model than in the NQS model.

Two additional simulations are conducted to examine the impacts of different initial conditions on precipitation prediction for the case considered in this study. For this, following Lee and Baik (2016), the initial potential temperature at every grid point is perturbed by the random noise uniformly distributed between –0.3 K and 0.3 K in the IQS and NQS model simulations. Except for the initial potential temperature perturbations, the experimental setup is the same as that described in chapter 3.3. Using the simulation and rain gauge data, the root-mean-square error and deviation are calculated. The root-mean-square error of 24-h accumulated surface precipitation amount is 9.5 mm in the IQS model and 9.7 mm in the NQS model. Thus, the IQS model improves over the NQS model, which is also found in the IQS and NQS model simulations without the initial potential temperature perturbations. The mean deviation of simulated 24-h accumulated surface precipitation amount is –5.3 mm in the IQS model and –6.1 mm in the NQS model. This means that the 24-h accumulated surface

precipitation amount is underestimated in both the models, but the IQS model is better than the NQS model in the performance of precipitation prediction, which is also found in the IQS and NQS model simulations without the initial potential temperature perturbations.

3.4.2. Impacts on precipitation and cloud microphysics

Figures 3.9a–3.9c show the distributions of 24-h accumulated surface precipitation amount in the IQS and NQS models and the difference between them. The accumulated surface precipitation amount in the domain is larger in the IQS model than in the NQS model. Focusing on a region of north central Mongolia where the surface precipitation amount is large (marked as the rectangle in Figure 3.9, hereafter called the analysis area), the increase in surface precipitation amount in the IQS model is overall more pronounced in the analysis area than in its outside area. The time series of surface precipitation rate averaged over the analysis area in the IQS and NQS models are presented in Figure 3.9d. The surface precipitation rate is consistently larger throughout the simulation period in the IQS model than in the NQS model despite spatial shifts in the distribution of surface precipitation. The 24-h accumulated surface precipitation amount averaged over the analysis area is 11.7 mm in the IQS model and 10.5 mm in the NQS model, 11.4% larger in the IQS model relative to the NQS model.

The distributions of accumulated surface precipitation amount in the IQS and NQS model simulations with the initial potential temperature perturbations were analyzed. It is found that the spatial patterns of accumulated surface precipitation

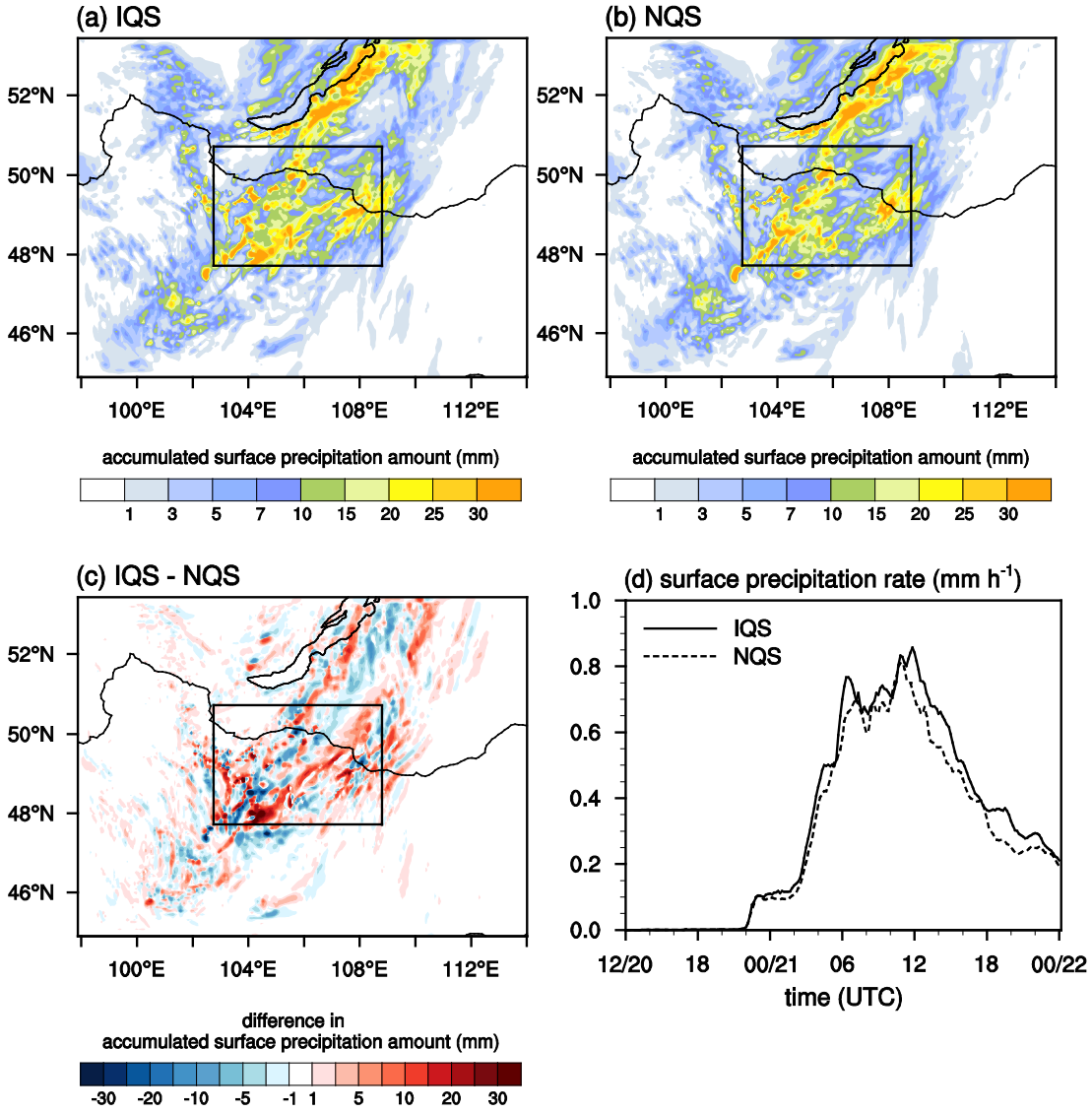
(a) IQS
(b) NQS
(c) IQS - NQS
(d) surface precipitation rate (mm h-1)
52°N
50°N
48°N
46°N
100°E
104°E
108°E
112°E
accumulated surface precipitation amount (mm)
1 3 5 7 10 15 20 25 30
difference in
accumulated surface precipitation amount (mm)
-30 -20 -10 -5 -1 1 5 10 20 30
IQS
NQS
1.0
0.8
0.6
0.4
0.2
0.0
12/20 18 00/21 06 12 18 00/22
time (UTC)

Figure 3.9. Distributions of accumulated surface precipitation amount from 00 UTC 21 to 00 UTC 22 August 2014 in (a) the IQS model and (b) the NQS model. (c) Difference in accumulated surface precipitation amount between the IQS model and the NQS model. (d) Time series of surface precipitation rate in the IQS and NQS models. In (d), the surface precipitation rate is averaged over the analysis area centered at Darkhan observatory (marked as the rectangle).

amount are similar to those in the IQS and NQS model simulations without the initial potential temperature perturbations. The time series of surface precipitation rate averaged over the analysis area show that before ~15 UTC the surface precipitation rate is larger in the IQS model than in the NQS model and after ~15 UTC the surface precipitation rate is smaller in the IQS model than in the NQS model. The 24-h accumulated surface precipitation amount averaged over the analysis area is larger in the IQS model (11.4 mm) than in the NQS model (10.9 mm), 4.6% larger in the IQS model relative to the NQS model. These results indicate some sensitivity of precipitation prediction to initial conditions. In spite of the sensitivity, the IQS model produces more precipitation than the NQS model in both the experimental settings (with and without the initial potential temperature perturbations). Further in-depth studies are needed to better understand the impacts of different initial conditions on precipitation prediction in the framework of the IQS and NQS models using an ensemble approach and many precipitation cases.

Figures 3.10a and 3.10b show the vertical profiles of hydrometeor mass contents averaged over 10–20 UTC 21 August 2014 and the analysis area in the IQS and NQS models. Note that the ice crystal mass content is the sum of column-, plate-, and dendrite-type ice crystal mass contents. In both the IQS and NQS models, the snow mass content is dominant, the averaged freezing level is ~4 km, and snow particles are simulated even below the freezing level because of the gradual melting of snow particles. Also, in both the models, supercooled drops exist largely between the freezing level and z ~ 5 km.

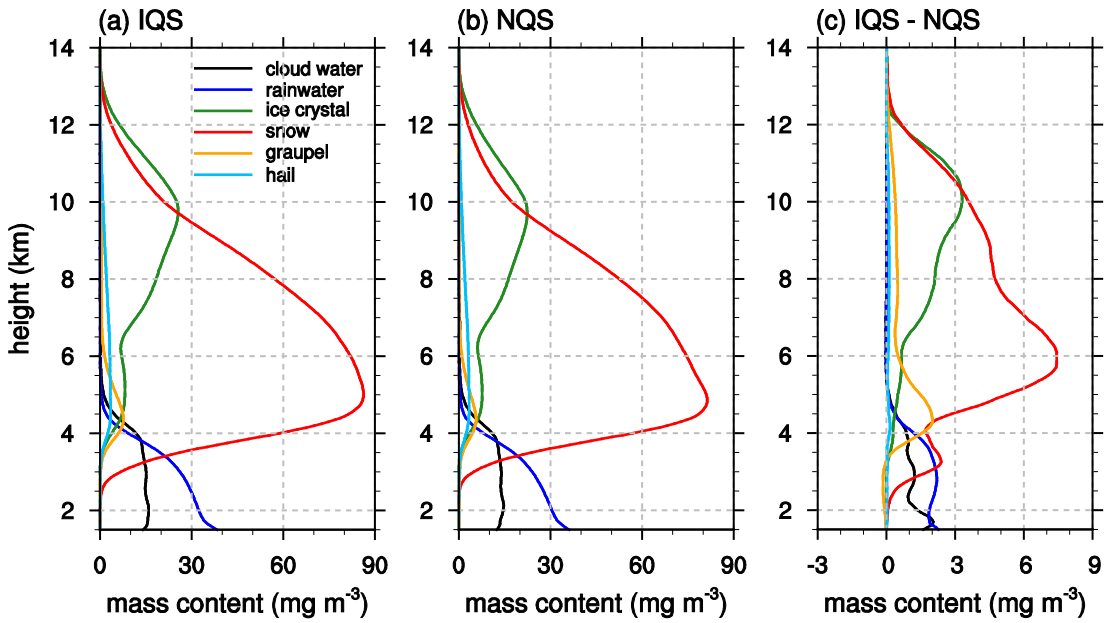

Figure 3.10. Vertical profiles of hydrometeor mass contents averaged over 10–20 UTC 21 August 2014 and the analysis area in (a) the IQS model and (b) the NQS model. (c) Differences in hydrometeor mass contents between the IQS model and the NQS model.

The differences in hydrometeor mass contents between the IQS and NQS models (Figure 3.10c) show that the mass contents of cloud water, rainwater, ice crystal, snow, and graupel increase in the IQS model relative to the NQS model and the hail mass contents almost the same in both the models. Among the increases in the hydrometeor mass contents, the increase in snow mass content is the most noticeable. The maximum increase in snow mass content is 7.4 mg m^{-3} at z = 5.9 km. The increase in ice crystal mass content above the freezing level is also noticeable, and its maximum increase is 3.3 mg m^{-3} at z = 10.1 km. The increase in graupel mass content is large between z ~ 4 km and z ~ 6 km. The maximum increase in graupel mass content is 2.0 mg m^{-3} at z = 4.4 km. The mass contents of cloud water and rainwater increase noticeably below z ~ 4 km. The enhanced large drop formation due to multiple collisions of cloud particles in the IQS model results in an increase in rainwater mass content. In addition to the enhanced large drop formation, the increased mass contents of snow and graupel in the IQS model can have a significant role in controlling rainwater mass content through melting.

The vertical profiles of vertical velocity and net heating rate due to cloud microphysical processes in the IQS and NQS models are presented in Figure 3.11. The vertical velocity and net heating rate are averaged over 10–20 UTC 21 August 2014 and the analysis area. The vertical profiles of vertical velocity in the IQS and NQS models are overall similar to each other, but there is a difference. In the mid-to-upper troposphere, the upward motion is stronger in the IQS model than in the NQS model. The vertical profiles of the net heating rate due to cloud microphysical processes in the

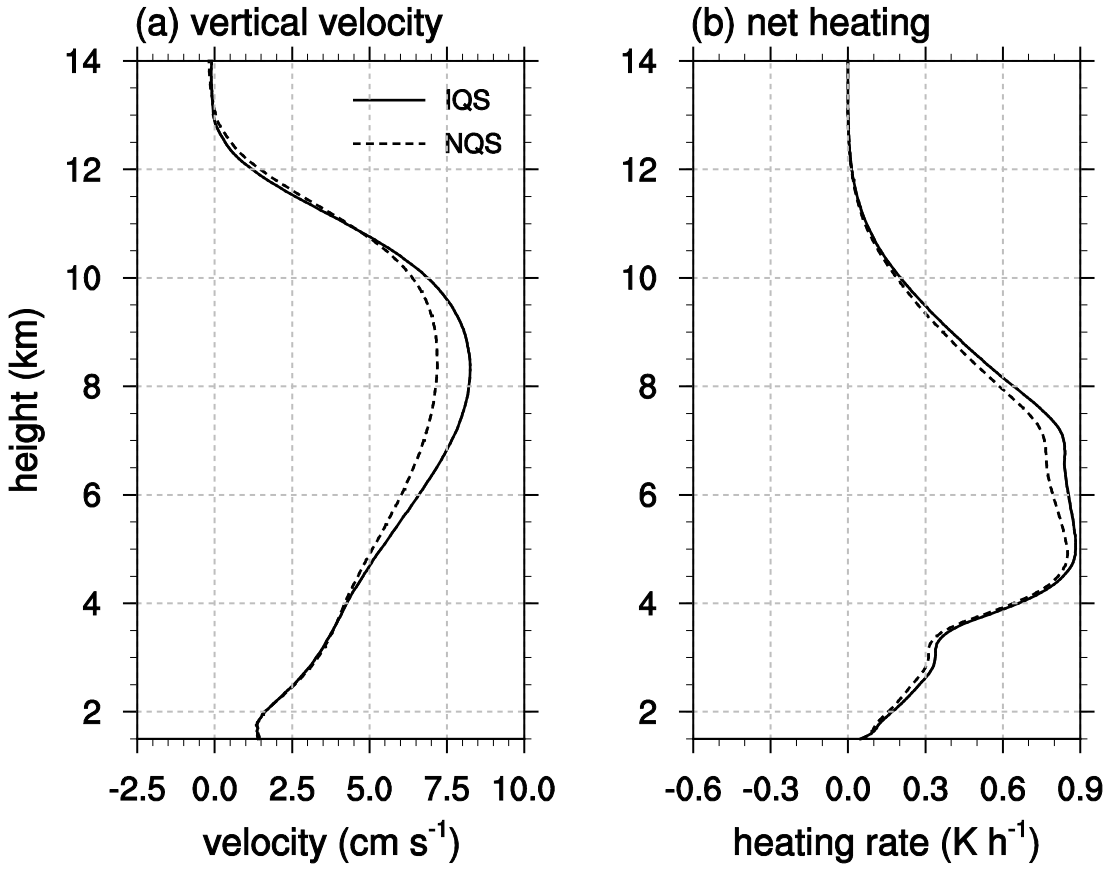

Figure 3.11. Vertical profiles of (a) vertical velocity and (b) net heating rate due to cloud microphysical processes averaged over 10–20 UTC 21 August 2014 and the analysis area in the IQS model and the NQS model.

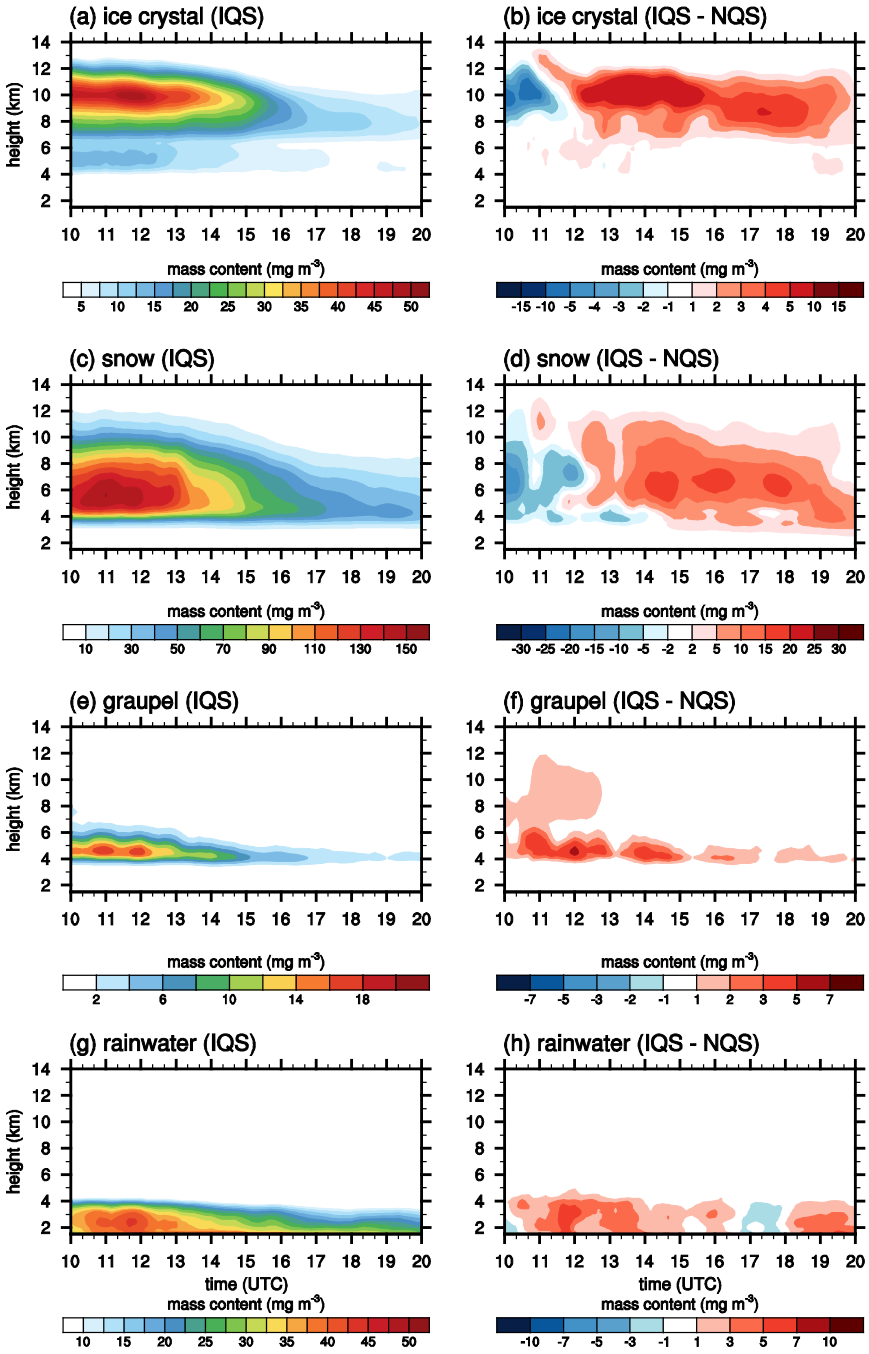
(a) ice crystal (IQS)
(b) ice crystal (IQS - NQS)
(c) snow (IQS)
(d) snow (IQS - NQS)
(e) graupel (IQS)
(f) graupel (IQS - NQS)
(g) rainwater (IQS)
(h) rainwater (IQS - NQS)
height (km)
time (UTC)
mass content (mg m-3)

Figure 3.12. Time-height sections of horizontally averaged (a) ice crystal mass content, (c) snow mass content, (e) graupel mass content, and (g) rainwater mass content in the IQS model. Differences in (b) ice crystal mass content, (d) snow mass content, (f) graupel mass content, and (h) rainwater mass content between the IQS model and the NQS model.

IQS and NQS models are also overall similar to each other, which are also positive in the mid-to-upper troposphere. The positive heating rate is consistently larger in the IQS model than in the NQS model. Figure 3.11 indicates that the increase in heating due to microphysical processes in the IQS model induces stronger upward motion which in turn enhances microphysical processes, thus promoting interactions of cloud microphysics with dynamics.

Figure 3.12 shows the time-height sections of horizontally averaged ice crystal, snow, graupel, and rainwater mass contents in the IQS model and the differences in ice crystal, snow, graupel, and rainwater mass contents between the IQS and NQS models. The ice crystal, snow, and graupel mass contents are large before ~12 UTC, and they exhibit a decreasing trend after ~12 UTC (Figures 3.12a, 3.12c, and 3.12e). The differences in ice crystal and snow mass contents are consistently positive after ~12 UTC. The analysis of the time-height section of horizontally averaged vertical velocity shows that the upward motion is stronger after ~12 UTC in the IQS model than in the NQS model (figure not shown). The difference in ice crystal mass content is large after ~12 UTC, and the difference in snow mass content is large after ~14 UTC. This implies that the increase in snow mass content in the IQS model is mainly caused by the increase in ice crystal mass content. The increase in snow mass content propagates downward, and it induces an increase in rainwater mass content through melting, hence resulting in the enhanced surface precipitation amount. Note that the significant increase in rainwater mass content before ~14 UTC is due to multiple collisions of cloud particles in the IQS model. Before ~12 UTC, the mass contents of ice crystal and snow

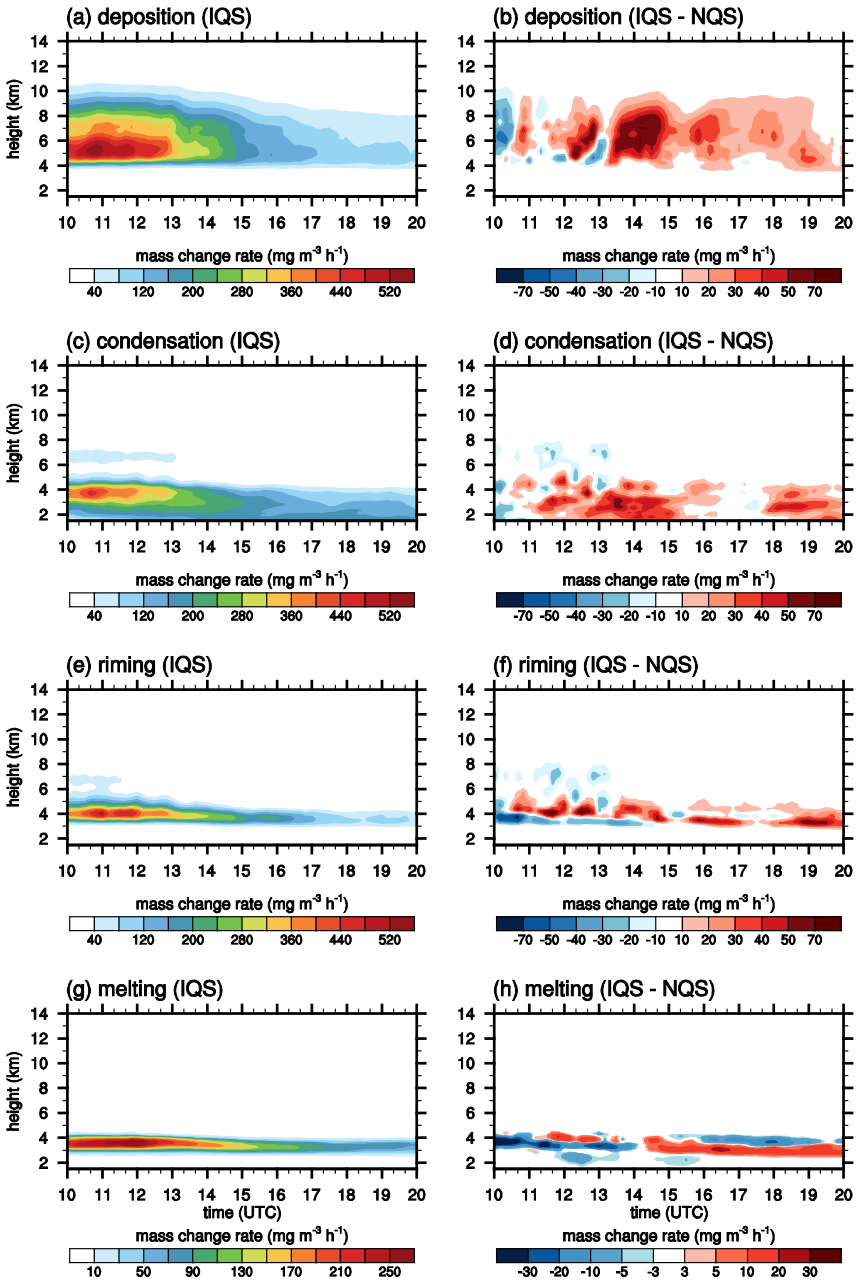
(a) deposition (IQS)
(b) deposition (IQS - NQS)
(c) condensation (IQS)
(d) condensation (IQS - NQS)
(e) riming (IQS)
(f) riming (IQS - NQS)
(g) melting (IQS)
(h) melting (IQS - NQS)
height (km)
time (UTC)
mass change rate (mg m-3 h-1)
40 120 200 280 360 440 520
-70 -50 -40 -30 -20 -10 10 20 30 40 50 70
10 50 90 130 170 210 250
-30 -20 -10 -5 -3 3 5 10 20 30

Figure 3.13. Time-height sections of horizontally averaged (a) deposition rate, (c) condensation rate, (e) riming rate, and (g) melting rate in the IQS model. Differences in (b) deposition rate, (d) condensation rate, (f) riming rate, and (h) melting rate between the IQS model and the NQS model.

are smaller in the IQS model than in the NQS model. This implies that in the IQS model ice-phased microphysical processes before ~12 UTC is less active than those after ~12 UTC.

Figure 3.13 shows the time-height sections of horizontally averaged deposition, condensation, riming, and melting rates in the IQS model and the differences in the rates between the IQS and NQS models. The increases in deposition and condensation in the IQS model are clear, and their trends are similar to those of the increases in snow and rain drop in the IQS model. This implies that the increases in snow and drop mass contents in the IQS model is largely due to the increased deposition and condensation, respectively. Also, these increases in snow and drop mass contents again contribute to the increases in deposition and condensation, respectively, which intensifies the differences in snow and drop mass contents. Riming just above the freezing level is stronger in the IQS model than in the NQS model. The increase in the ice mass content due to riming after ~14 UTC in the IQS model is mainly caused by the riming of snow (Figures 3.12d and 3.13f). On the other hand, the increase in ice mass content due to riming before ~14 UTC in the IQS model is mainly caused by the riming of graupel (Figures 3.12f and 3.13f). Riming plays a role in increasing snow mass content after ~14 UTC in the IQS model, and the increased snow mass content results in the enhanced surface precipitation amount through melting (Figure 3.13h). Although the graupel mass content is also increased before ~14 UTC in the IQS model, reduced ice-phased microphysical processes appear to result in the decreased melting of ice particles. The overall enhancement of deposition, condensation, and riming causes more latent

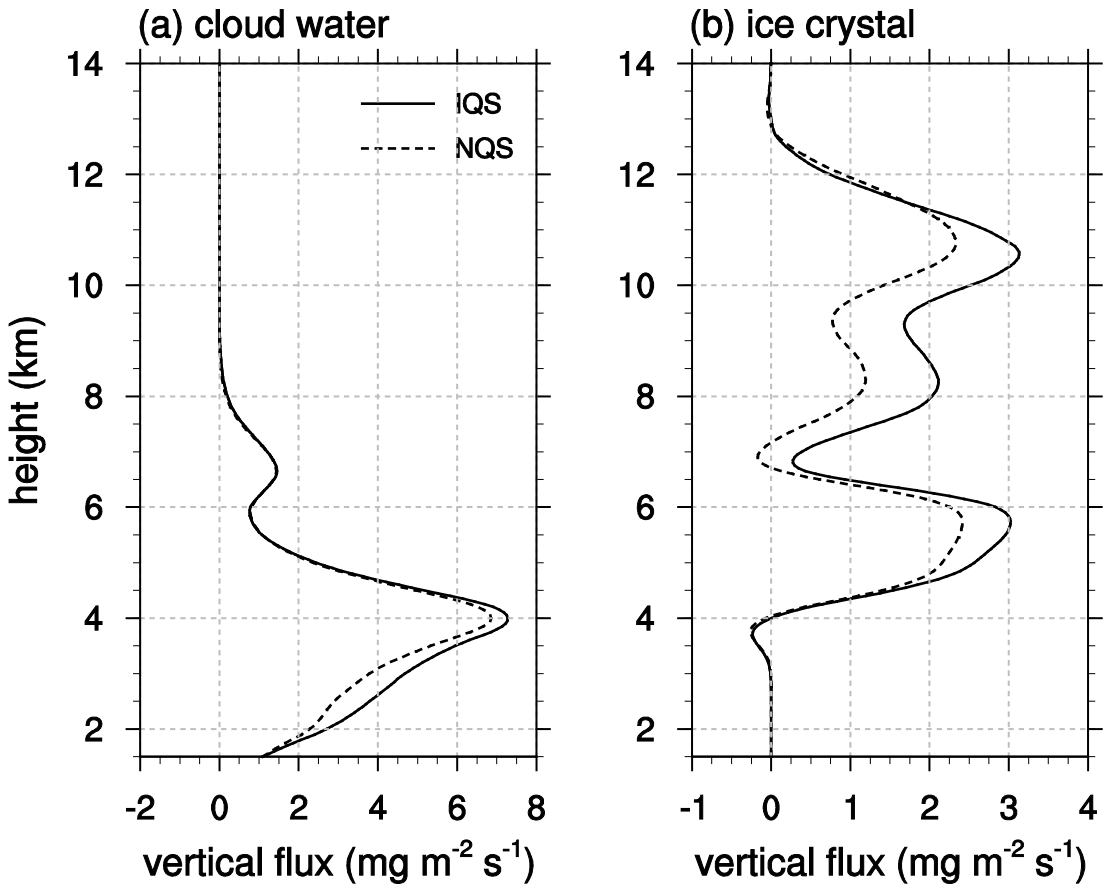

Figure 3.14. Vertical profiles of the vertical fluxes of (a) cloud water and (b) ice crystal averaged over 10–20 UTC 21 August 2014 and the analysis area in the IQS model and the NQS model.

heat release in the IQS model than in the NQS model (Figure 3.11b), which contributes to the stronger upward motion in the IQS model than in the NQS model (Figure 3.11a).

The vertical profiles of the vertical fluxes of cloud water and ice crystal in the IQS and NQS models averaged over 10–20 UTC 21 August 2014 and the analysis area are presented in Figure 3.14. Here, the vertical flux of any hydrometeor is defined as the hydrometeor mass content times ($w + v_t$), where w is the vertical velocity and v_t is the terminal velocity of the hydrometeor (v_t is negative). In both the IQS and NQS models, the vertical flux of cloud water is positive, that is, cloud droplets are transported upward. Between $z \sim 1.5$ km and $z \sim 5.5$ km, the vertical flux of cloud water is larger in the IQS model than in the NQS model, implying that multiple collisions of cloud particles in the IQS model leads to more vertical transport of cloud droplets. The vertical flux of ice crystal is positive at almost all levels. Some large differences in the vertical flux of ice crystal between the IQS and NQS models are present in the layer between $z \sim 5$ km and $z \sim 11$ km where more vertical transport of ice crystal occurs in the IQS model. As mentioned before, the upward motion is enhanced due to the increased latent heat release in the IQS model, which contributes to the positive differences in the vertical fluxes of cloud water and ice crystal (Figure 3.14).

Figure 3.15 shows the size distributions of drop (cloud droplet plus raindrop), snow, and graupel averaged over the 10-h period and the analysis area in the IQS and NQS models and the differences in the size distributions of drop, snow, and graupel between the IQS and NQS models. The size distribution is calculated at $z = 3$ km for drop, at $z = 5$ km for snow, and $z = 4$ km for graupel. In both the IQS and NQS models,

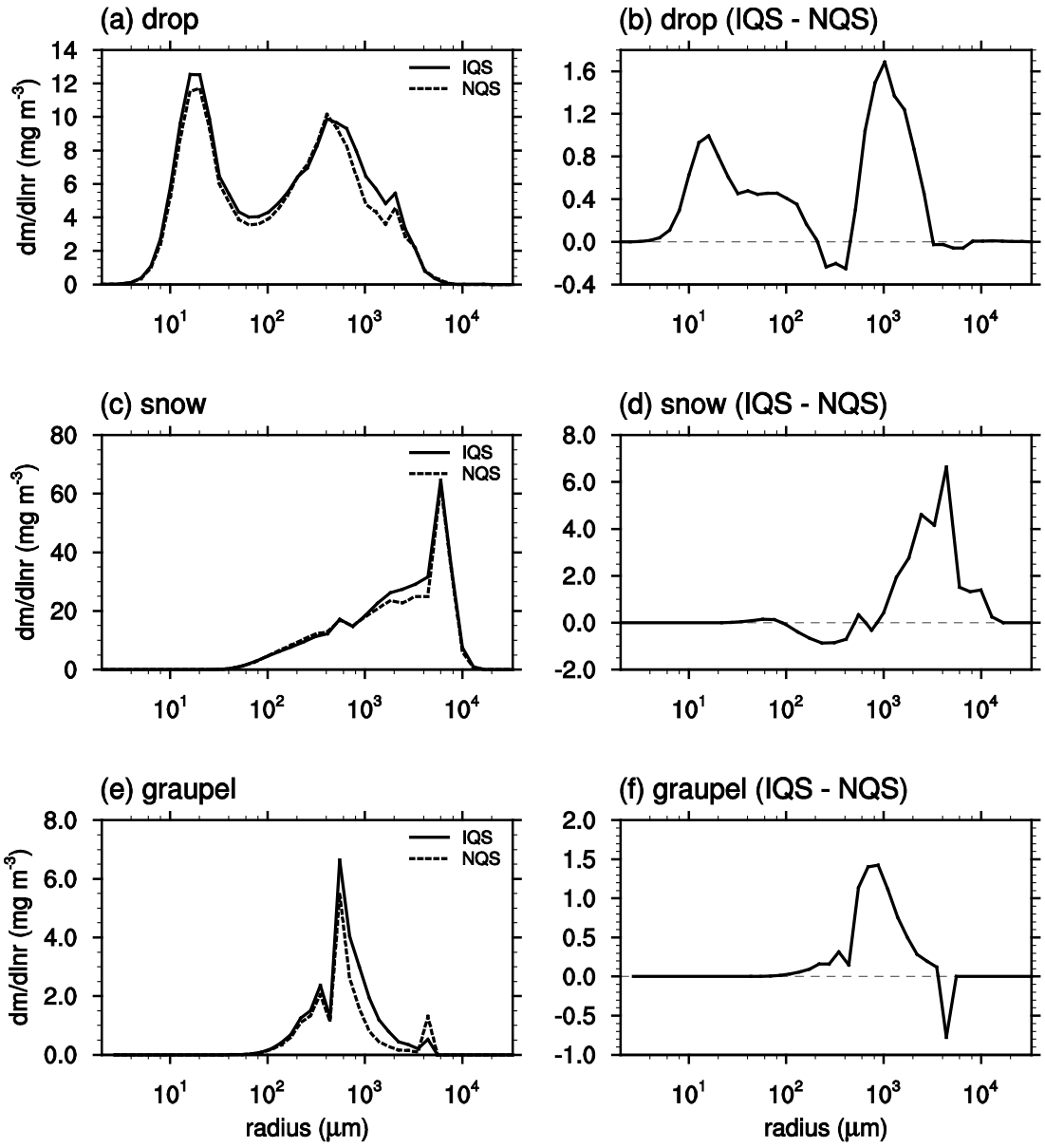

Figure 3.15. Size distributions of (a) drop at z = 3 km, (c) snow at z = 5 km, and (e) graupel at z = 4 km averaged over 10–20 UTC 21 August 2014 and the analysis area in the IQS and NQS models. Differences in the size distributions of (b) drop, (d) snow, and (f) graupel between the IQS model and the NQS model.

the drop size distribution exhibits primary peaks at ~20 μm and ~410 μm in radius, which belong to cloud droplets and raindrops, respectively. The difference in drop size distribution shows that the drop mass content is increased in the IQS model both in the small drop range (maximum at ~20 μm) and in the large drop range (maximum at ~1 mm). The increased large drop mass content contributes to the enhanced surface precipitation amount. It is noted that the drop mass content in a part of medium sizes is decreased in the IQS model. The increased drop mass content in the small drop range in the IQS model results from the difference between the IQS and NQS models. However, unlike in the box model and idealized two-dimensional simulations in chapter 2.2, in the real-case simulation (the present study), it seems to be very difficult to find detailed reasons for the increased drop mass content in the small drop range because of the increased complexity. More activation of CCN due to the increase in upward motion can be a reason. Further study is needed to find reasons for that, in views of microphysics and dynamics feedback.

For the snow size distribution, both the IQS and NQS models share common features that it exhibits a primary peak at ~6 mm in radius and the mass of snow is largely occupied by large snow particles (~0.1–1 cm in radius) (Figure 3.15c). The difference between the IQS and NQS models is mainly positive, that is, the snow mass content is larger in the IQS model than in the NQS model. In Figure 3.12, it is shown that the increase in snow mass content is largely caused by the increase in ice crystal mass content. Therefore, it can be deduced that the increase in the mass content of cloud droplets (Figure 3.15b) causes the increase in ice crystal mass content by increased

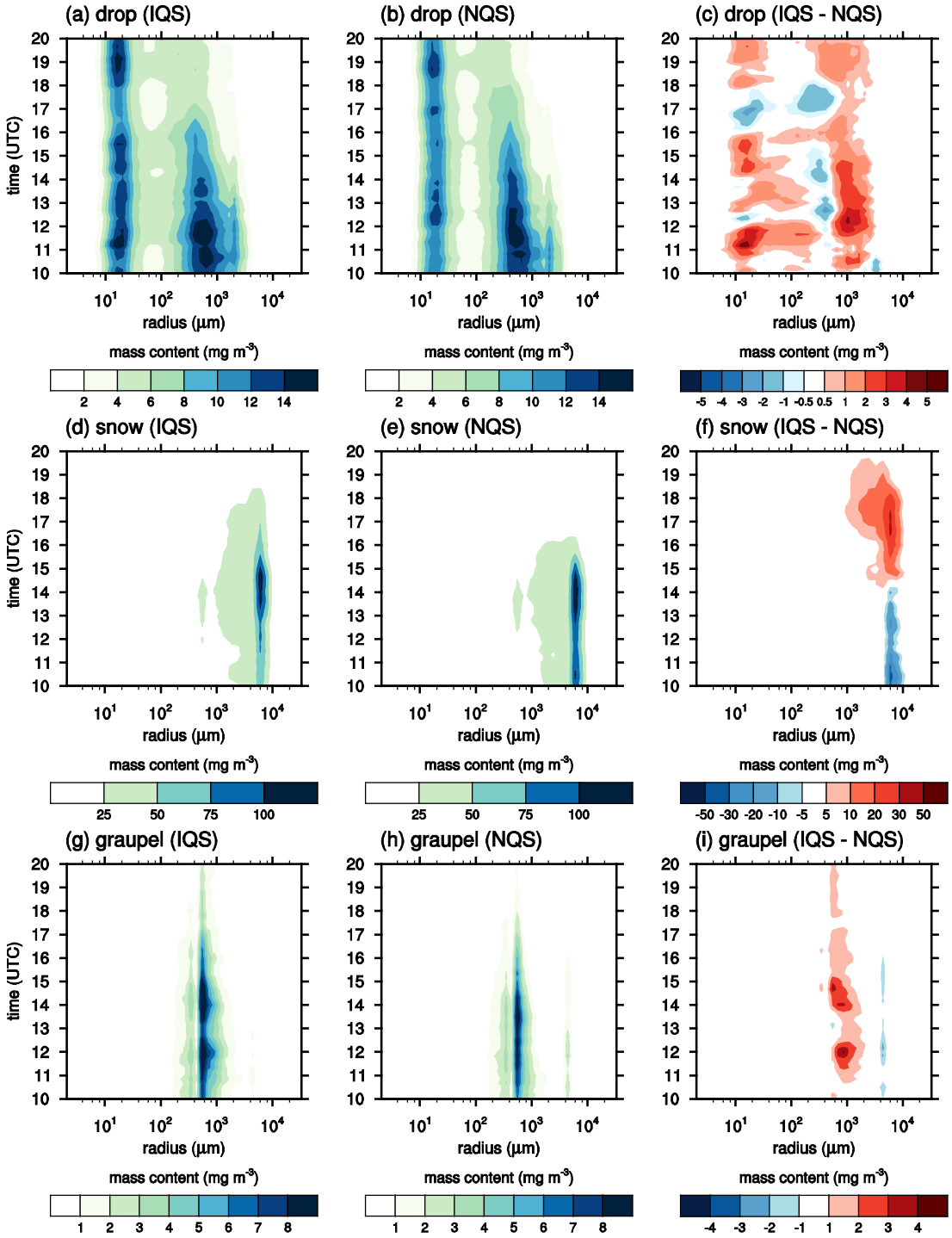
(a) drop (IQS)
(b) drop (NQS)
(c) drop (IQS - NQS)
(d) snow (IQS)
(e) snow (NQS)
(f) snow (IQS - NQS)
(g) graupel (IQS)
(h) graupel (NQS)
(i) graupel (IQS - NQS)
time (UTC)
radius (μm)
mass content (mg m-3)

Figure 3.16. Time evolution of the horizontally averaged size distributions of (a) drop in the IQS model, (b) drop in the NQS model, and (c) difference in drop size distribution between the IQS model and the NQS model. (d), (e), and (f) are the same as (a), (b), and (c), respectively, but for snow. (g), (h), and (i) are the same as (a), (b), and (c), respectively, but for graupel.

upward transport of cloud droplets (Figure 3.14a) and freezing, hence increasing snow mass content. In addition, this increased snow mass content contributes to the increased raindrop mass content (Figures 3.15b and 3.15d) through melting, which enhances the surface precipitation amount. The graupel size distribution exhibits a primary peak at ~550 μm in both the IQS and NQS models (Figure 3.15e). The graupel mass content is noticeably larger in the IQS model than in the NQS model in the ~0.5–2 mm radius range, with its maximum difference at ~880 μm (Figure 3.15f).

Figure 3.16 is the same as Figure 3.15 but as a form of the time evolution of the size distributions of drop, snow, and graupel and the differences. Figure 3.16 exhibits the characteristics of the size distributions in more detail. The increases in the mass of small and large drops are seen throughout almost the entire period and are more distinct before ~15 UTC. The increase in the mass of large snow particles is simulated after ~14 UTC (see also Figure 3.12d). This implies that the increase in the mass of large drops after ~14 UTC is caused by the increase in the mass of large snow particles. The increase in graupel mass content in the ~0.5–2 mm radius range is seen throughout the time period, especially before ~15 UTC. Before ~15 UTC, the riming of snow with increased large drops may result in an increase in graupel mass content. However, Figures 3.16f and 3.16i show that after ~15 UTC the contribution of the increased graupel mass content to surface precipitation amount through melting is less significant than the contribution of the increased snow mass content to surface precipitation amount through melting. This results in the decrease in melting before ~14 UTC in the IQS model (Figure 3.13h).

Based upon the analysis results of Figures 3.8–3.16, we construct a schematic diagram which depicts major pathways of microphysics that result in the larger surface precipitation amount in the IQS model relative to the NQS model (Figure 3.17). The IQS model that takes account of multiple collisions of cloud particles increases the mass contents of both large drops and small drops. The increased large drops grow through coalescence and condensation, which further increases the mass content of larger drops. The increased mass content of larger drops contributes to the increase in surface precipitation amount. This pathway is depicted on the left side of the schematic diagram. The increased small drops due to multiple collisions are transported upward, grow through condensation, and then freeze, forming ice crystals. The ice crystals grow by deposition, further increasing ice crystal mass content. The increase in the mass content of ice crystal gives rise to the increase in the mass content of snow through deposition and riming. The mass content of snow is further increased through deposition and riming. The increased mass content of snow increases the mass content of large drops through the melting of snow particles. Thus, the increased mass content of large drops also contributes to the increase in surface precipitation amount. This pathway is depicted on the right side of the schematic diagram.

It should be noted that the schematic diagram shows major microphysics pathways only that lead to the larger amount of surface precipitation in the IQS model. The interactions of microphysics with dynamics in the precipitation systems simulated in this study, which need further investigation, are too complicated to understand fully and be included appropriately in a schematic diagram. The schematic diagram presented,

nonetheless, could be a valuable one showing the connections of microphysical processes.

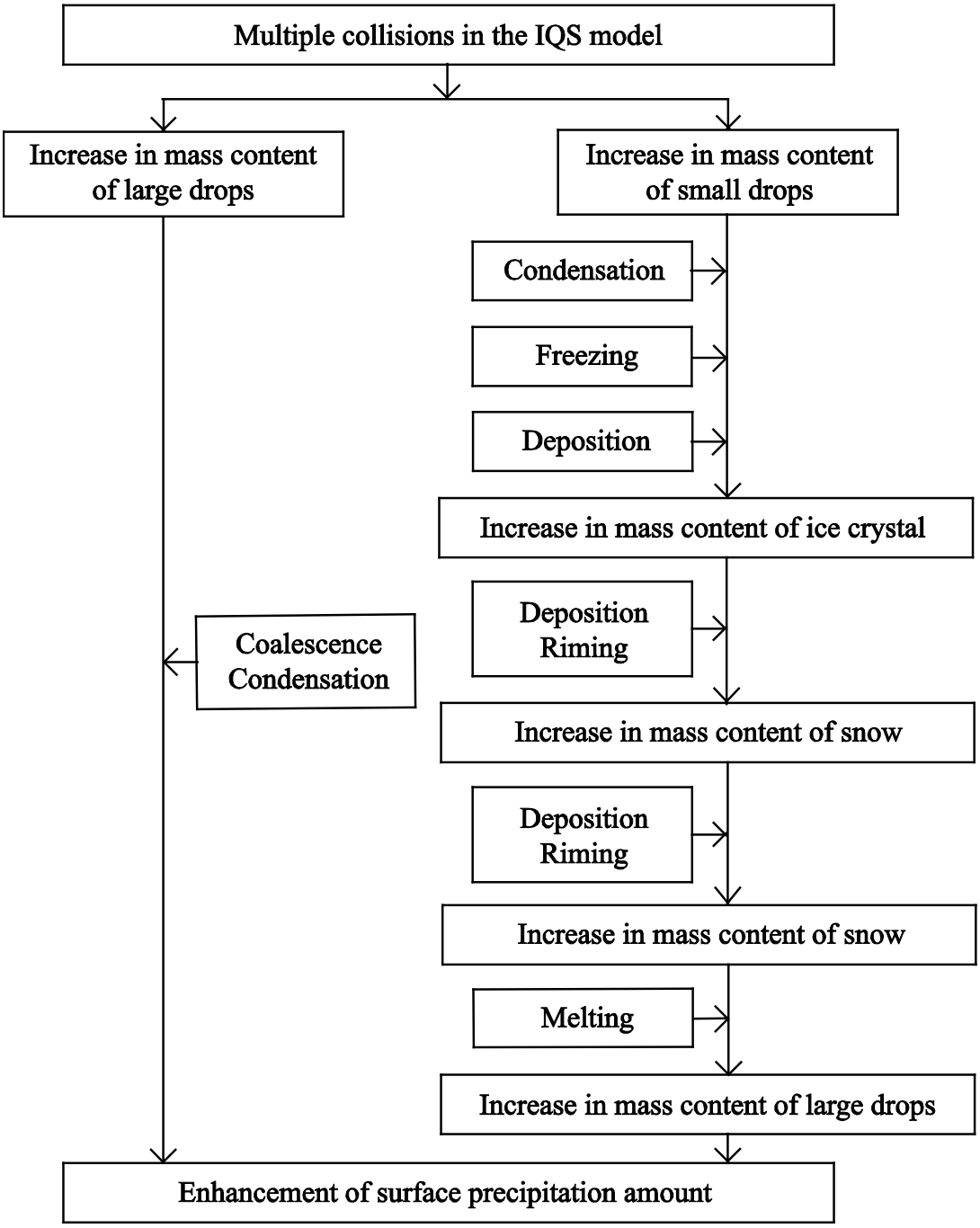

Figure 3.17. Schematic diagram of microphysical processes that result in the larger surface precipitation amount in the IQS model.

3.5. Summary and conclusions

The IQS model that allows for multiple collisions of cloud particles within a time step was evaluated through precipitation prediction. For this purpose, a precipitation event observed over north central Mongolia on 21 August 2014 was simulated using the WRF model with a detailed bin microphysics scheme and the simulation results from the IQS model were compared to those from NQS model in which a cloud particle can collide with other cloud particle only once within a time step.

The simulated surface precipitation amount in the IQS model is closer to the observation than that in the NQS model, although both the IQS and NQS models underestimate the surface precipitation amount. It was found that the surface precipitation amount is larger in the IQS model than in the NQS model, particularly over the strong precipitation region. Microphysical processes that lead to the larger surface precipitation amount in the IQS model were analyzed in detail. In the IQS model, the mass contents of both large drops and small drops are increased due to multiple collisions of cloud particles. The increased large drops act to increase surface precipitation amount. The increased small drops increase snow mass content through freezing, deposition, and riming. The increased snow mass content also acts to increase surface precipitation amount through melting.

The number of studies that utilize numerical models that include bin microphysics schemes to understand clouds and precipitation has increased in recent years with advances in computing power. The quasi-stochastic collection model that takes account of multiple collisions of cloud particles can be easily implemented in

models with bin microphysics schemes, expecting to better simulate cloud and precipitation processes, as demonstrated in this study. This study considered only one precipitation event. Many precipitation events are required to examine the impacts of the IQS model on cloud and precipitation processes which could vary with environmental conditions, deserving an investigation. In chapter 2, it is indicated that the effects of aerosols on the evolution of drop size distribution can be modulated by the IQS model. Aerosol effects on clouds and precipitation in the IQS model through real case simulations need to be also investigated to better understand cloud-aerosol-precipitation interactions.

4. Impacts of aerosol loading on surface precipitation from deep convective systems over north central Mongolia.

4.1. Introduction

Aerosols in the atmosphere play an important role in radiation processes and cloud and precipitation processes. They can serve as cloud condensation nuclei or ice nuclei. The sizes and chemical compositions of aerosols greatly influence the size distribution of nucleated drops in a cloud which subsequently affects the evolution of the cloud (Houze, 2014). Aerosol-cloud-precipitation interactions have been recognized as one of the important problems in weather and climate research.

The impacts of aerosols on clouds and precipitation have been extensively investigated using numerical models, particularly focusing on how surface precipitation varies with aerosol number concentration (see review papers of Khain, 2009; Tao et al., 2012; Fan et al., 2016). Many studies have shown that surface precipitation from shallow warm clouds decreases with increasing aerosol number concentration (Kuba and Fujiyoshi, 2006; Xue and Feingold, 2006; Cheng et al., 2007; Fan et al., 2012; Choi et al., 2014) while surface precipitation from deep convective clouds increases with increasing aerosol number concentration (Khain et al., 2005; Wang, 2005; Rosenfeld et al., 2008; Igel et al., 2013; Clavner et al., 2017). The enhancement of surface precipitation from deep convective clouds with increasing aerosol number concentration has been explained as the invigoration of deep convective clouds under certain

conditions such as humid condition. In a polluted environment, the mean radius of condensates is reduced (Twomey, 1977) and the production of raindrops through collision-coalescence is inhibited. Instead, more cloud droplets are transported upward above the freezing level and then freeze with releasing latent heat, which consequently promotes updrafts and the formation of ice hydrometeors (Rosenfeld et al., 2008) and eventually enhances surface precipitation. The evaporation of raindrops in the boundary layer can strengthen cold pool, which can facilitate the formation of secondary convection and thus enhance surface precipitation (Khain et al., 2005; Rosenfeld et al., 2008; O'Halloran et al., 2015). On the other hand, some studies have shown that the variation of surface precipitation with aerosol number concentration is not monotonic (Ilotoviz et al., 2016; Alizadeh-Choobari and Gharaylou, 2017; Dagan et al., 2017), implying the complexity of aerosol-cloud-precipitation interactions.

In the past two decades, numerical models with bin microphysics schemes have been broadly used to better understand clouds and precipitation and more accurately predict precipitation (e.g., Khain et al., 1999; Lynn et al., 2005; Khain et al., 2005; Tao et al., 2007; Khain, 2009; Han et al., 2012; Iguchi et al., 2012; Xue et al., 2012; Lee et al., 2014; Khain et al., 2015; Xiao et al., 2015; Lee and Baik, 2016; Tao and Li., 2016; Gayatri et al., 2017; Sarangi et al., 2017). Numerical models with bin microphysics schemes predict the number concentration of each hydrometeor for each size bin. Accordingly, the size distributions of hydrometeors are better represented in numerical models with bin microphysics schemes than those with bulk microphysics schemes in which specified size-distribution functions are used. Hence, numerical models with bin

microphysics schemes can be used more reliably to examine aerosol impacts on clouds and precipitation, although they require much more computing resources.

The improved quasi-stochastic collection (IQS) model which considers multiple collisions of cloud particles within a model time step is evaluated in chapter 2. Using a numerical model that includes the IQS, a precipitation prediction over north central Mongolia is performed in chapter 3.

This study investigates the impacts of aerosol loading on surface precipitation from mid-latitude deep convective systems through real-case simulations, particularly attempting to find pathways that lead to the variation of surface precipitation amount with aerosol loading. As a real case, a precipitation event that occurred over north central Mongolia is selected. In chapter 4.2, the case description and experimental setup are briefly described. In chapter 4.3, results and discussion are given. A summary and conclusions are provided in chapter 4.4.

4.2. Case description and experimental setup

The case selected for this study is the 21 August 2014 precipitation event over north central Mongolia in chapter 3. The 24-h accumulated surface precipitation amount that day was 30 mm in Ulaanbaatar and 19 mm in Darkhan. The two locations are indicated in Fig. 4.1a. In Mongolia, the average annual precipitation amount is ~210 mm, so the precipitation event with the 24-h accumulated surface precipitation amount of ~20–30 mm is unique. To see the synoptic environment of the precipitation event, the

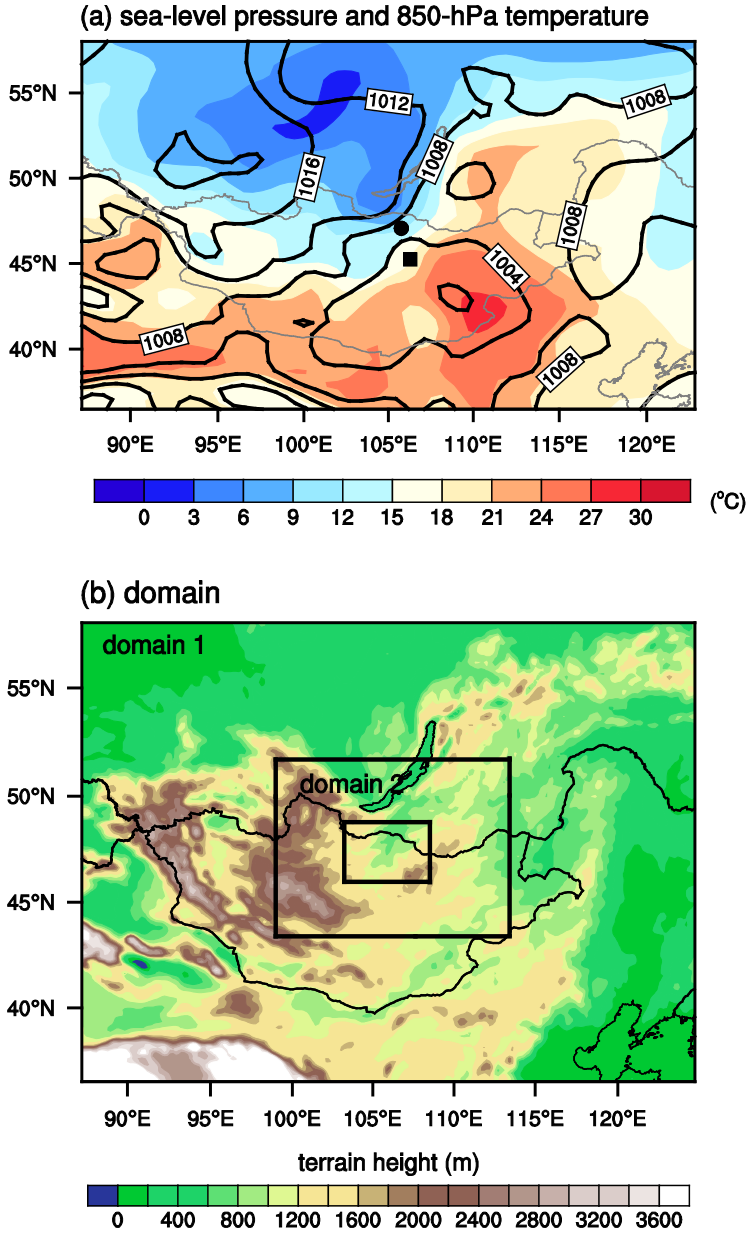
(a) sea-level pressure and 850-hPa temperature
55°N
50°N
45°N
40°N
1012
1008
1016
1008
1008
1004
1008
1008
90°E
95°E
100°E
105°E
110°E
115°E
120°E
0
3
6
9
12
15
18
21
24
27
30
(°C)
(b) domain
domain 1
domain 2
55°N
50°N
45°N
40°N
90°E
95°E
100°E
105°E
110°E
115°E
120°E
terrain height (m)
0
400
800
1200
1600
2000
2400
2800
3200
3600

Figure 4.1. (a) Field of mean sea-level pressure (hPa, black solid lines) and 850-hPa temperature (color shaded) at 12 UTC 21 August 2014 plotted using the ERA-Interim (0.75° × 0.75°) reanalysis data. The circle and square represent the locations of Darkhan and Ulaanbaatar observatories, respectively. (b) Two nested computational domains (domain 1 and domain 2) and terrain height. The innermost rectangular area represents the analysis area. (a) and (b) are adapted from chapter 3.

mean sea-level pressure and 850-hPa temperature field at 12 UTC 21 August 2014 is presented in Fig. 4.1a. This figure is adapted from chapter 3 (Fig. 3.1. and Fig 3.6.). The low-level warm low is located southeast of Ulaanbaatar at 12 UTC 21 and moves northeastward. The low-level cold high is located northwest of Darkhan at 12 UTC 21 and moves southeastward. Near Darkhan, the gradients of pressure and temperature become large, implying the presence of a cold front. The precipitation that occurred on 21 August 2014 is associated with the warm low and the cold front.

The numerical model used in this study is the Weather Research and Forecasting (WRF) model coupled with the bin microphysics scheme of the Hebrew University Cloud Model (HUCM) (Lee and Baik, 2016). The IQS model is implemented in the bin microphysics scheme in chapters 2.2.2 and 3.3. The bin microphysics scheme considers seven hydrometeor types [liquid drop, three types of ice crystals (column, plate, and dendrite), snow, graupel, and hail] and aerosol and uses 43 mass-doubling bins. The turbulence-induced collision enhancement is not included in the present study. All physical parameterization schemes and experimental setup are the same as those in chapter 3.3. Figure 4.1b shows two one-way nested computational domains: the outer domain (domain 1) with a horizontal grid size of 15 km and the inner domain (domain 2 with a horizontal grid size of 5 km). The ERA-interim reanalysis data (Dee et al., 2011) are used to provide initial and boundary conditions for the WRF model.

Following Khain et al. (2000) and Lee et al. (2014), the initial size distribution of aerosol number concentration $N(r_a)$ is given by

$$\frac{dN}{d\ln r_a} = \frac{3}{2} N_0 k \left(\frac{4A^3}{27Br_a^{\ 3}} \right)^{k/2} . \quad (4.1)$$

Here, r_a is the radius of aerosol, N_0 is the cloud condensation nucleus (CCN) number concentration at 1% supersaturation, k (= 0.5) is a constant, and A and B are coefficients related to the curvature and solution effects, respectively. The radius of the largest aerosol is 2 μm. To examine the impacts of aerosol loading on surface precipitation amount, six numerical experiments are carried out with initial aerosol number concentrations of N_0 = 150, 300, 600, 1200, 2400, and 4800 cm^{-3}. The initial aerosol number concentration in the vertical is uniform up to 2 km height above the surface and then decreases exponentially with an *e*-folding height of 2 km. In chapter 3, N_0 = 300 cm^{-3} was used. The WRF model is integrated for 36 h starting from 12 UTC 20 August 2014, and the last 24-h simulation data are used for analysis. For further details of the case synopsis, numerical model, and experimental setup, see chapter 3.

4.3. Results and discussion

To understand how and why surface precipitation amount from the deep convective systems over north central Mongolia varies as the aerosol number concentration increases, we analyze surface precipitation amount, mass contents and number concentrations of hydrometeors, mass change rates of hydrometeors and water vapor due to microphysical processes, and size distributions of hydrometeors. Figure 4.2

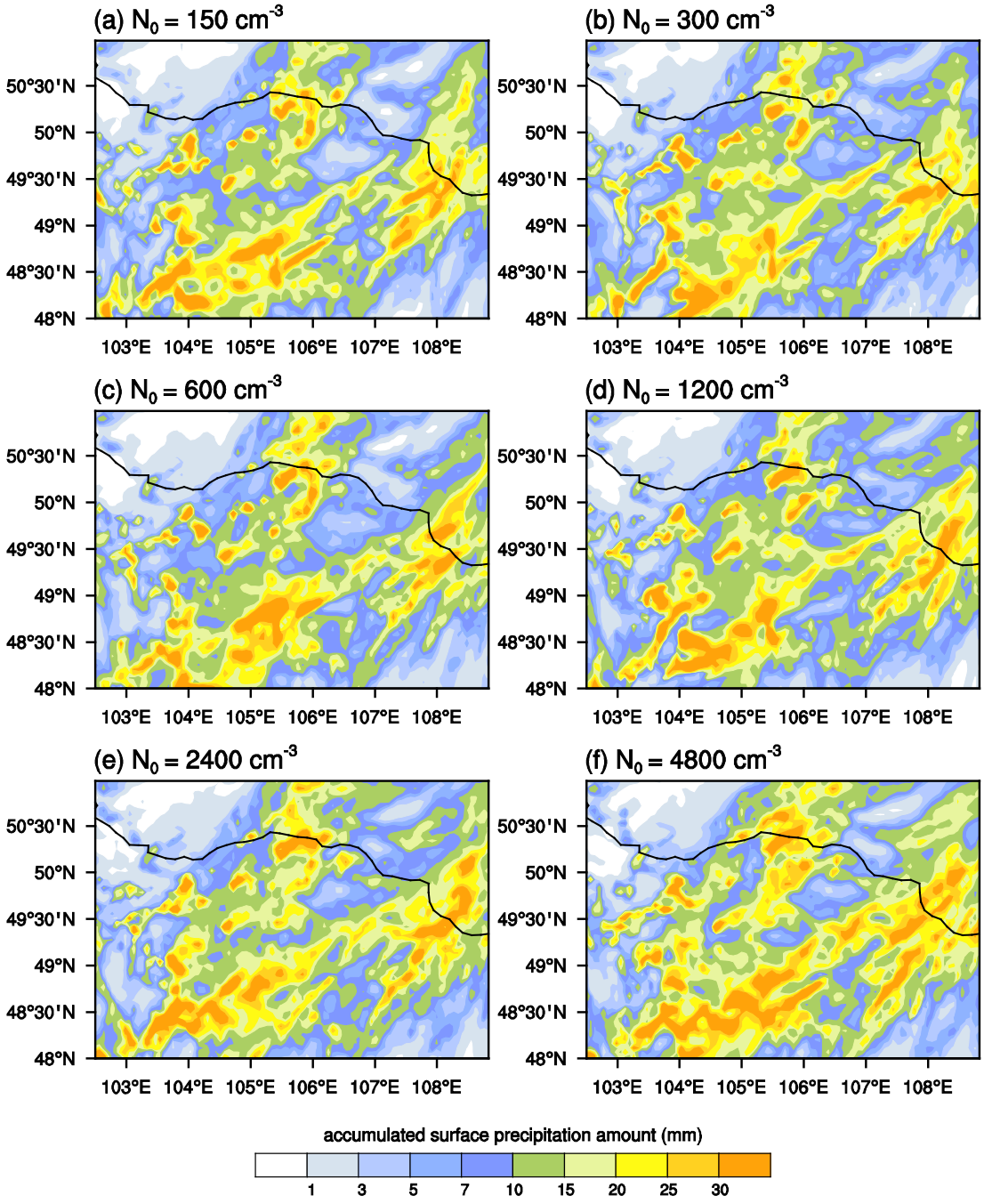
(a) N0 = 150 cm-3
(b) N0 = 300 cm-3
(c) N0 = 600 cm-3
(d) N0 = 1200 cm-3
(e) N0 = 2400 cm-3
(f) N0 = 4800 cm-3
50°30'N
50°N
49°30'N
49°N
48°30'N
48°N
103°E 104°E 105°E 106°E 107°E 108°E
accumulated surface precipitation amount (mm)
1 3 5 7 10 15 20 25 30

Figure 4.2. Distributions of accumulated surface precipitation amount in the analysis area from 00 UTC 21 to 00 UTC 22 August 2014 in the cases of aerosol number concentrations of N_0 = (a) 150, (b) 300, (c) 600, (d) 1200, (e) 2400, and (f) 4800 cm^{-3}. The case of N_0 = 300 cm^{-3} is the same as that in chapter 3.

shows the distributions of 24-h accumulated surface precipitation amount in the analysis area from 00 UTC 21 to 00 UTC 22 August 2014 for initial aerosol number concentrations of N_0 = 150, 300, 600, 1200, 2400, and 4800 cm^{-3}. Note that N_0 = 300 cm^{-3} is used in chapter 3. Overall, the spatial distributions of accumulated surface precipitation amount, which are associated with the warm low and the cold front, are similar to each other. Major rainbands are elongated in the southwest-northeast direction. In addition to the similarities, some differences are also evident in the fine structure and amount of surface precipitation. For example, in the case of N_0 = 4800 cm^{-3}, the rainband elongated in the southwest-northeast direction in the southern region of the analysis area is longer and stronger than those in the other cases.

Figure 4.3 shows the averaged 24-h accumulated surface precipitation amount as a function of the initial aerosol number concentration. The average is taken over the analysis area. The non-monotonic behavior of the accumulated surface precipitation amount is seen as the aerosol number concentration changes. This kind of non-monotonic behavior has been revealed in several studies (Ilotoviz et al., 2016; Alizadeh-Choobari and Gharaylou, 2017). In the range of N_0 = 150–600 cm^{-3}, the accumulated surface precipitation amount slightly decreases with increasing aerosol number concentration. On the other hand, in the range of N_0 = 600–4800 cm^{-3}, the increase in accumulated surface precipitation amount with increasing aerosol number concentration is notable. The increasing trend of surface precipitation with increasing aerosol number concentration has been reported in many studies (e.g., Wang, 2005; Lee et al., 2008; Zhou et al., 2017). Several studies support the hypothesis that greater aerosol loading

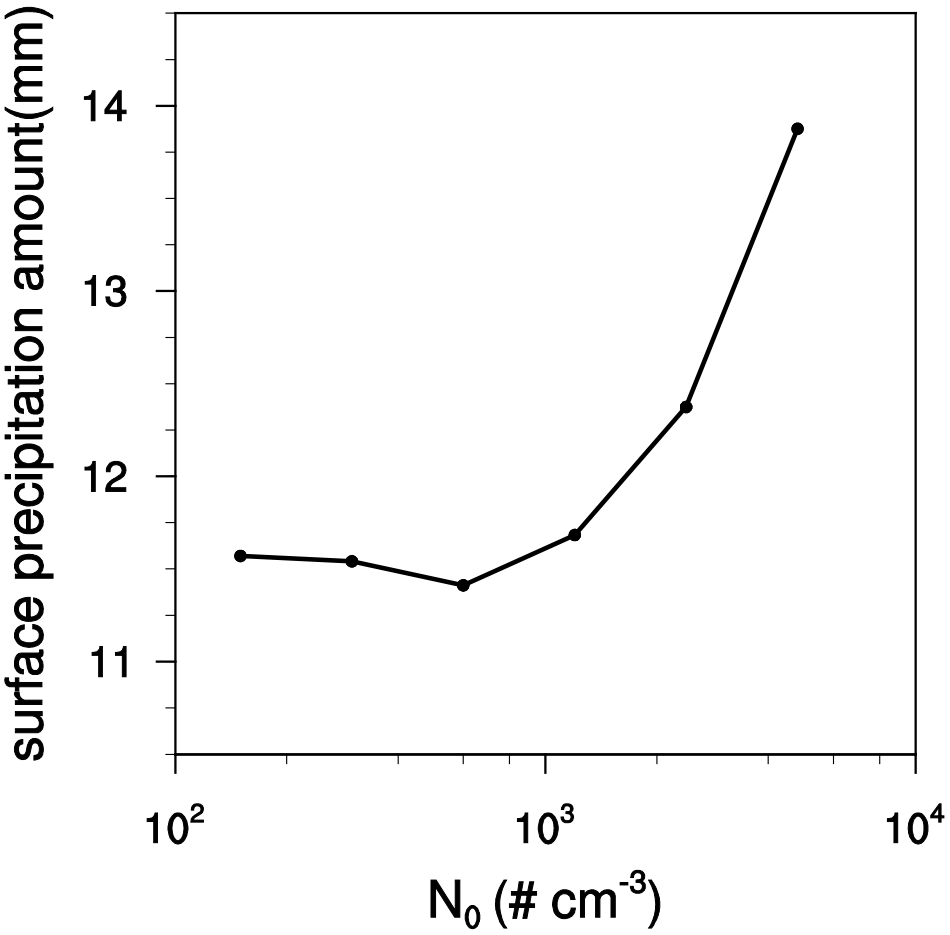

Figure 4.3. Accumulated surface precipitation amount from 00 UTC 21 to 00 UTC 22 August averaged over the analysis area as a function of the initial aerosol number concentration.

leads to the invigoration of deep convective systems (Khain et al., 2005; Lee et al., 2008; Rosenfeld et al., 2008). In the present study, the 24-h accumulated surface precipitation amount averaged over the analysis area in the case of N_0 = 4800 cm^{-3} (13.9 mm) is 22% larger than that in the case of N_0 = 600 cm^{-3} (11.4 mm). Next, we present analysis results of mass contents and number concentrations of hydrometeors, mass change rates of hydrometeors and water vapor due to microphysical processes, and size distributions of hydrometeors and attempt to explain why the accumulated surface precipitation amount increases with increasing aerosol number concentration in the range of N_0 = 600–4800 cm^{-3}.

The vertical profiles of hydrometeor mass contents in the case of N_0 = 4800 cm^{-3} and differences in hydrometeor contents between the case of N_0 = 4800 cm^{-3} and the case of N_0 = 600 cm^{-3} averaged over the 24-h period and the analysis area are presented in Figs. 4.4a and 4.4b, respectively. In Fig. 4.4 (also Figs. 4.5, 4.6, and 4.8), the height is the height from the mean sea level. The average topographic height in the analysis area is ~1200 m. The freezing level is z ~ 4 km. Figure 4.4a shows that the snow mass content is the largest, followed by the ice crystal mass content. The snow mass content is maximal at z ~ 5 km, and the ice crystal mass content is maximal at z ~ 10 km. Snow particles are seen even below the freezing level because of their gradual melting. Below z ~ 3 km, the rainwater mass content is the largest. The mass content of supercooled drops is largely concentrated between the freezing level and z ~ 5 km. Although the graupel mass content is much smaller than that of snow or ice crystal, it is notably

concentrated between z ~ 4 km and z ~ 6 km. Hail is also seen, but the hail mass content is small.

Above the freezing level, the snow mass content is consistently larger in the case of N_0 = 4800 cm^{-3} than in the case of N_0 = 600 cm^{-3} (Fig. 4.4b). The cloud water and rainwater mass contents are notably larger in the case of N_0 = 4800 cm^{-3} than in the case of N_0 = 600 cm^{-3} (Fig. 4.4b). As will be presented later, the increased snow mass content is responsible for an increase in rainwater mass content. The increase in cloud water mass content is particularly pronounced between z ~ 2 km and z ~ 3 km. The increase in cloud water mass content above the freezing level means the increase in the amount of supercooled cloud droplets in the case of N_0 = 4800 cm^{-3}. The rainwater mass content also increases below the freezing level in the case of N_0 = 4800 cm^{-3}. This results from an increase in the melting of snow particles and from an increase in the collisional growth of raindrops, which are produced by the melting of snow particles, in the layer with larger cloud water mass content.

Figure 4.5 shows the vertical profiles of the number concentrations of cloud drops (cloud droplets), ice crystals, and raindrops averaged over the 24-h period and the analysis area in the cases of N_0 = 600 and 4800 cm^{-3}. The cloud drop number concentration is consistently higher in the case of N_0 = 4800 cm^{-3} than in the case of N_0 = 600 cm^{-3} due to the higher aerosol number concentration. The maximum number concentration of cloud drops is ~4030 L^{-1} (per one liter of air) at z ~ 3 km in the case of 4800 cm^{-3} and ~2460 L^{-1} at z ~ 3 km in the case of 600 cm^{-3}, ~1.6 times larger in the case of N_0 = 4800 cm^{-3}. The ice crystal number concentration is also consistently higher

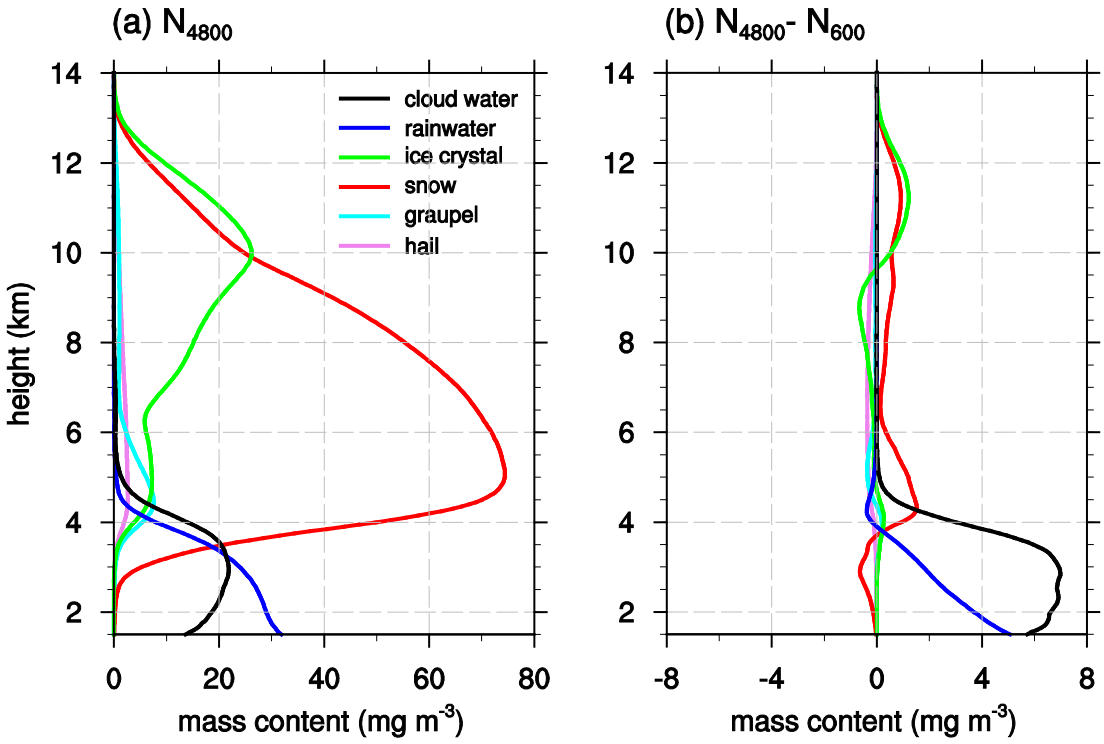

Figure 4.4. (a) Vertical profiles of hydrometeor mass contents averaged over 24 h from 00 UTC 21 to 00 UTC 22 August 2014 and the analysis area in the case of N_0 = 4800 cm^{-3}. (b) Vertical profiles of differences in hydrometeor mass contents between the case of N_0 = 4800 cm^{-3} and the case of N_0 = 600 cm^{-3}.

in the case of N_0 = 4800 cm^{-3} than in the case of N_0 = 600 cm^{-3}. In both the cases, the maximum number concentration of ice particles is seen just above the freezing level. Just above the freezing level, a portion of the cloud drops transported below the freezing level freeze, forming ice crystals (Figs. 4.5a and 4.5b). The higher number concentration and smaller mass content of ice crystals mean that the average size of ice crystals is smaller in the case of N_0 = 4800 cm^{-3} than in the case of N_0 = 600 cm^{-3} (Figs.4.4b and 4.5b). On the other hand, the raindrop number concentration is consistently lower in the case of N_0 = 4800 cm^{-3} than in the case of N_0 = 600 cm^{-3}. The lower number concentration and larger mass content of raindrops mean that the average size of raindrops is larger in the case of N_0 = 4800 cm^{-3} than in the case of N_0 = 600 cm^{-3} (Figs. 4.4b and 4.5c). In the case of N_0 = 4800 cm^{-3}, the average size of ice crystals is small, but the average size of raindrops is large. This implies that the growth of small-sized ice crystals through mixed-phased processes is important.

Figure 4.6a shows the vertical profiles of the mass change rates of hydrometeors and water vapor due to deposition, sublimation, condensation, evaporation, freezing, melting, riming, and nucleation averaged over the 24-h period and the analysis area in the case of N_0 = 4800 cm^{-3}. Here, the mass change rate due to a microphysical process means the increase rate of the mass of water vapor, liquid water or ice produced through the microphysical process. For example, the mass change rate due to condensation means the increase rate of the mass of liquid water due to condensation. The mass change rate due to nucleation is amplified 10 times. Overall, the mass change rate due to deposition is much larger than that of sublimation and the mass change rate due to

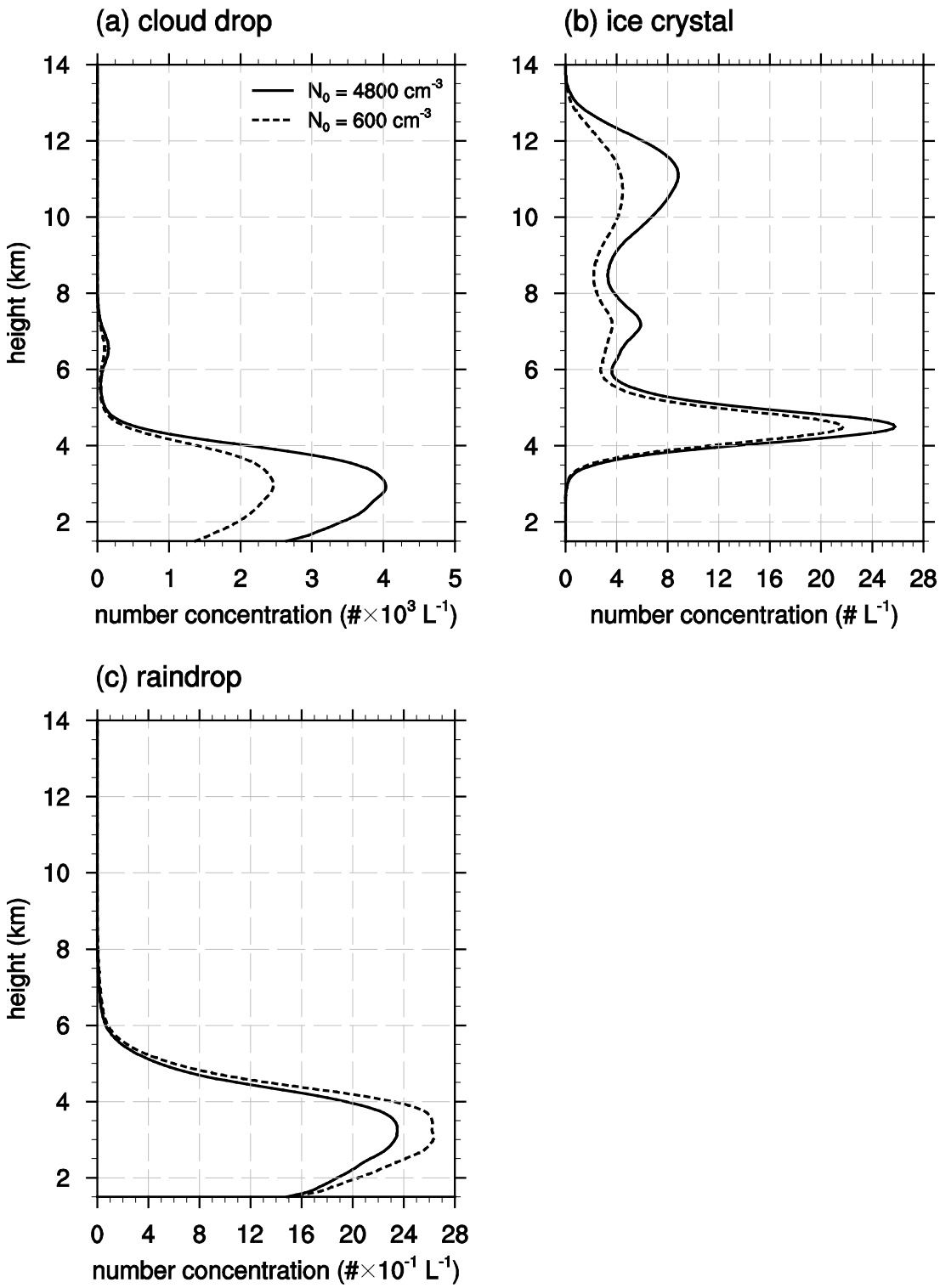
(a) cloud drop
(b) ice crystal
(c) raindrop
height (km)
N_0 = 4800 cm^{-3}
N_0 = 600 cm^{-3}
number concentration (#×10^{3} L^{-1})
number concentration (# L^{-1})
number concentration (#×10^{-1} L^{-1})

Figure 4.5. Vertical profiles of the number concentrations of (a) cloud drop, (b) ice crystal, and (c) raindrop averaged over 24 h from 00 UTC 21 to 00 UTC 22 August 2014 and the analysis area in the cases of N_0 = 600 and 4800 cm^{-3}.

condensation is larger than that of evaporation. On the other hand, overall, the mass change rate due to freezing is smaller than that of melting. The mass change rate due to riming is notable, whose peak is located at $z \sim 4$ km and whose peak magnitude is comparable to that of the mass change rate due to deposition or condensation. The mass change rate due to nucleation is negligible. From Figs. 4.6a and 4.4a, can deduce that the deposition in the mid- and upper troposphere is mainly responsible for the snow mass content and the growth of snow particles through riming is effective near the freezing level.

Differences in the mass change rates of hydrometeors and water vapor due to microphysical processes (Fig. 4.6b) indicate increases in riming, evaporation, and condensation in the case of $N_0 = 4800$ cm^{-3} relative to the case of $N_0 = 600$ cm^{-3}. The maximum increases in the mass change rates due to riming, evaporation, and condensation are seen at $z \sim 4$, 3, and 2 km, respectively. Higher aerosol number concentration produces more drops of small sizes. Thus, the sum of surface areas of drops is larger and accordingly the diffusional growth of drops becomes stronger (Lee et al., 2014), which is reflected in the larger mass change rate due to condensation in the case of $N_0 = 4800$ cm^{-3} relative to the case of $N_0 = 600$ cm^{-3} (Fig. 4.6b). As discussed earlier, the average size of ice crystals is smaller, while the number concentration of ice crystals is higher in the case of $N_0 = 4800$ cm^{-3} than in the case of $N_0 = 600$ cm^{-3}. This is reflected in the lower mass change rate due to freezing in the case of $N_0 = 4800$ cm^{-3} than in the case of $N_0 = 600$ cm^{-3} (Fig. 4.6b). The mass change rate due to melting is overall lower in the case of $N_0 = 4800$ cm^{-3} than in the case of $N_0 = 600$ cm^{-3} except for

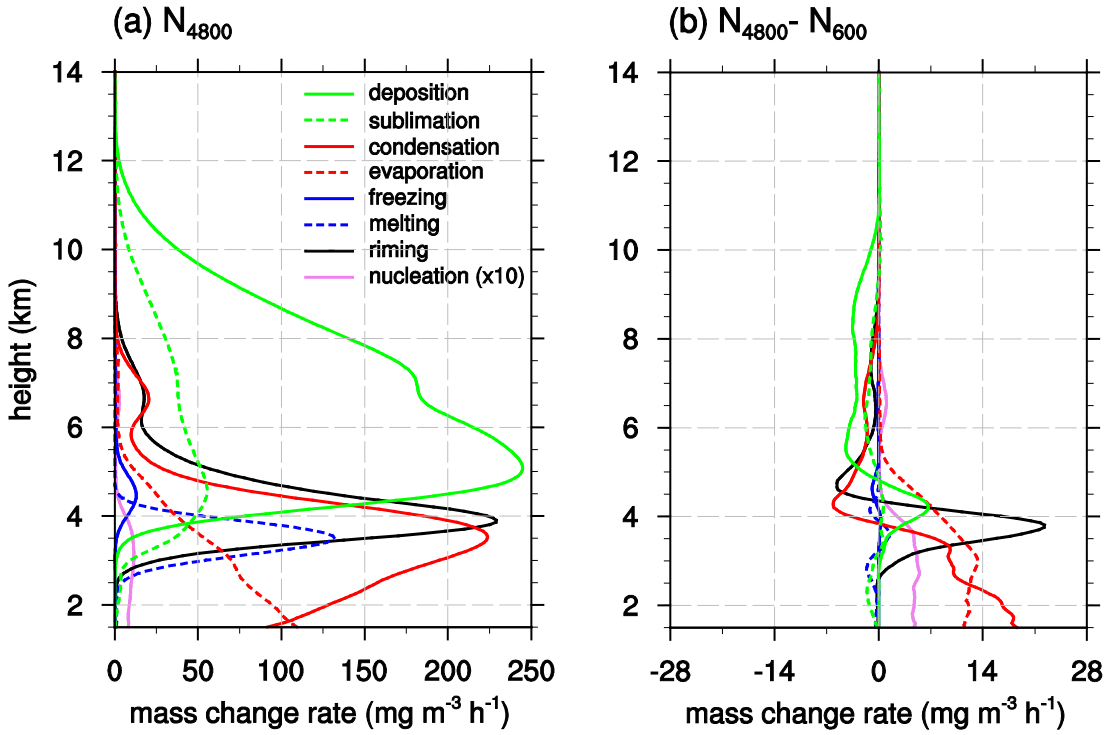

Figure 4.6. (a) Vertical profiles of the mass change rates of hydrometeors due to deposition, sublimation, condensation, evaporation, freezing, melting, riming, and nucleation (amplified 10 times) processes averaged over 24 h from 00 UTC 21 to 00 UTC 22 August 2014 and the analysis area in the case of N_0 = 4800 cm^{-3}. (b) Vertical profiles of differences in the mass change rates of hydrometeors due to deposition, sublimation, condensation, evaporation, freezing, melting, riming, and nucleation (amplified 10 times) processes between the case of N_0 = 4800 cm^{-3} and the case of N_0 = 600 cm^{-3}.

the layer just below the freezing level. As will be shown below, however, the number concentration of snow particles is higher in the case of N_0 = 4800 cm^{-3} than in the case of N_0 = 600 cm^{-3}, contributing to an increase in the mass content of raindrops through melting and active collision-coalescence.

Figure 4.7 shows the mass size distributions of drops at z = 3 km and snow at z = 5 km and the number size distributions of snow at z = 5 km averaged over the 24-h period and the analysis area in the cases of N_0 = 600 and 4800 cm^{-3}. The differences in the size distributions of drops at z = 3 km, snow at z = 5 km, and snow at z = 7 km between the case of N_0 = 4800 cm^{-3} and the case of N_0 = 600 cm^{-3} are also shown. At z = 3 km, the drop mass content is particularly larger in the size range of ~6–15 μm in radius, which belongs to a size range of cloud droplets, in the case of N_0 = 4800 cm^{-3} than in the case of N_0 = 600 cm^{-3} (Figs. 4.4a and 4.4b). This result means that more drops of small sizes form as the aerosol number concentration is higher. The maximum difference in the mass size distribution of drops is seen at ~10 μm in radius. More drops of small sizes increase the total area of drops, thus resulting in stronger low-level condensation (Fig. 4.6b). In addition, more drops of small sizes contribute to increases in ice crystals and supercooled drop mass contents above the freezing level (Fig. 4.4b).

The mass size distributions of snow at z = 5 km in the cases of N_0 = 600 and 4800 cm^{-3} are similar to each other and exhibit a high peak at ~6 mm (Fig. 4.7c). In the case of N_0 = 4800 cm^{-3}, more cloud droplets result in more ice crystals through freezing (Figs. 4.4b and 4.7a). More ice crystals are grown into more small-sized snow particles near the freezing level largely through deposition (Figs. 4.4b, 4.6b, and 4.7e). As a

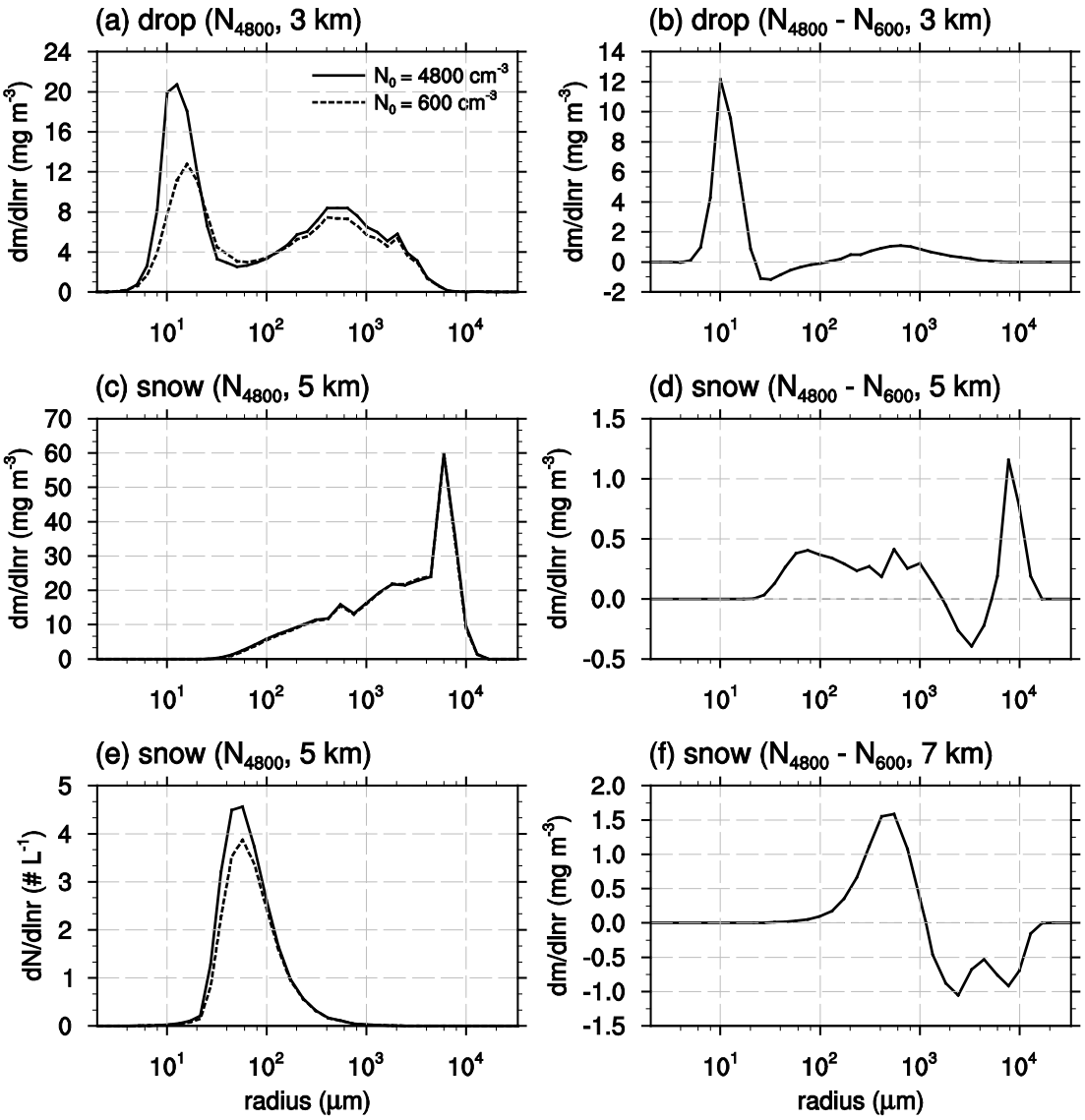
(a) drop (N_{4800}, 3 km)
N_0 = 4800 cm^{-3}
N_0 = 600 cm^{-3}
dm/dlnr (mg m^{-3})
(b) drop (N_{4800} - N_{600}, 3 km)
dm/dlnr (mg m^{-3})
(c) snow (N_{4800}, 5 km)
dm/dlnr (mg m^{-3})
(d) snow (N_{4800} - N_{600}, 5 km)
dm/dlnr (mg m^{-3})
(e) snow (N_{4800}, 5 km)
dN/dlnr (# L^{-1})
radius (μm)
(f) snow (N_{4800} - N_{600}, 7 km)
dm/dlnr (mg m^{-3})
radius (μm)

Figure 4.7. Mass size distributions of (a) drops at z = 3 km and (c) snow at z = 5 km and number size distributions of (e) snow at z = 5 km in the cases of N_0 = 4800 cm^{-3} (solid lines) and 600 cm^{-3} (dashed lines). Differences in the mass size distributions of (b) drops at z = 3 km, (d) snow at z = 5 km, and (f) snow at z = 7 km between the case of N_0 = 4800 cm^{-3} and the case of N_0 = 600 cm^{-3}. All the size distributions are obtained by averaging over 24 h from 00 UTC 21 to 00 UTC 22 August 2014 and the analysis area.

result, the mass content of small-sized snow particles is larger in the case of N_0 = 4800 cm^{-3} than in the case of N_0 = 600 cm^{-3} (Fig. 4.7d). In addition, the mass content of large-sized snow particles is larger in the radius range of ~6–15 mm with a peak at ~8 mm in the case of N_0 = 4800 cm^{-3} than in the case of N_0 = 600 cm^{-3} (Fig. 4.7d). Through the comparison of Fig. 4.7d with Fig. 4.7f, can deduce that the increased mass content of large-sized snow particles is largely due to riming. More snow particles of large sizes which grow through riming melt to form relatively large drops. The relatively large drops collect drops of small sizes (collision-coalescence process), which leads to enhanced surface precipitation amount.

Van den Heever et al. (2006) and Fan et al. (2012) showed that the high CCN concentration results in the high graupel/hail mass content through riming in their numerical modeling studies of deep convective clouds over Florida and the Southeast China, respectively. A recent numerical modeling study of aerosol loading effects on the amount of surface precipitation from deep convective clouds over the Indian peninsula during the monsoon season (Gayatri et al., 2017) also showed that the melting of graupel particles grown through active riming largely affects the surface precipitation amount in the high CCN case. On the other hand, this study shows that the increase in surface precipitation amount is mainly due to the melting of snow particles rather than graupel particles. One plausible reason for the difference in results between the aforementioned studies and this study might be associated with the differing climates of the study regions. North central Mongolia is less humid than Florida, the Southeast China, and India. In the less humid region, the growth of graupel and hail particles

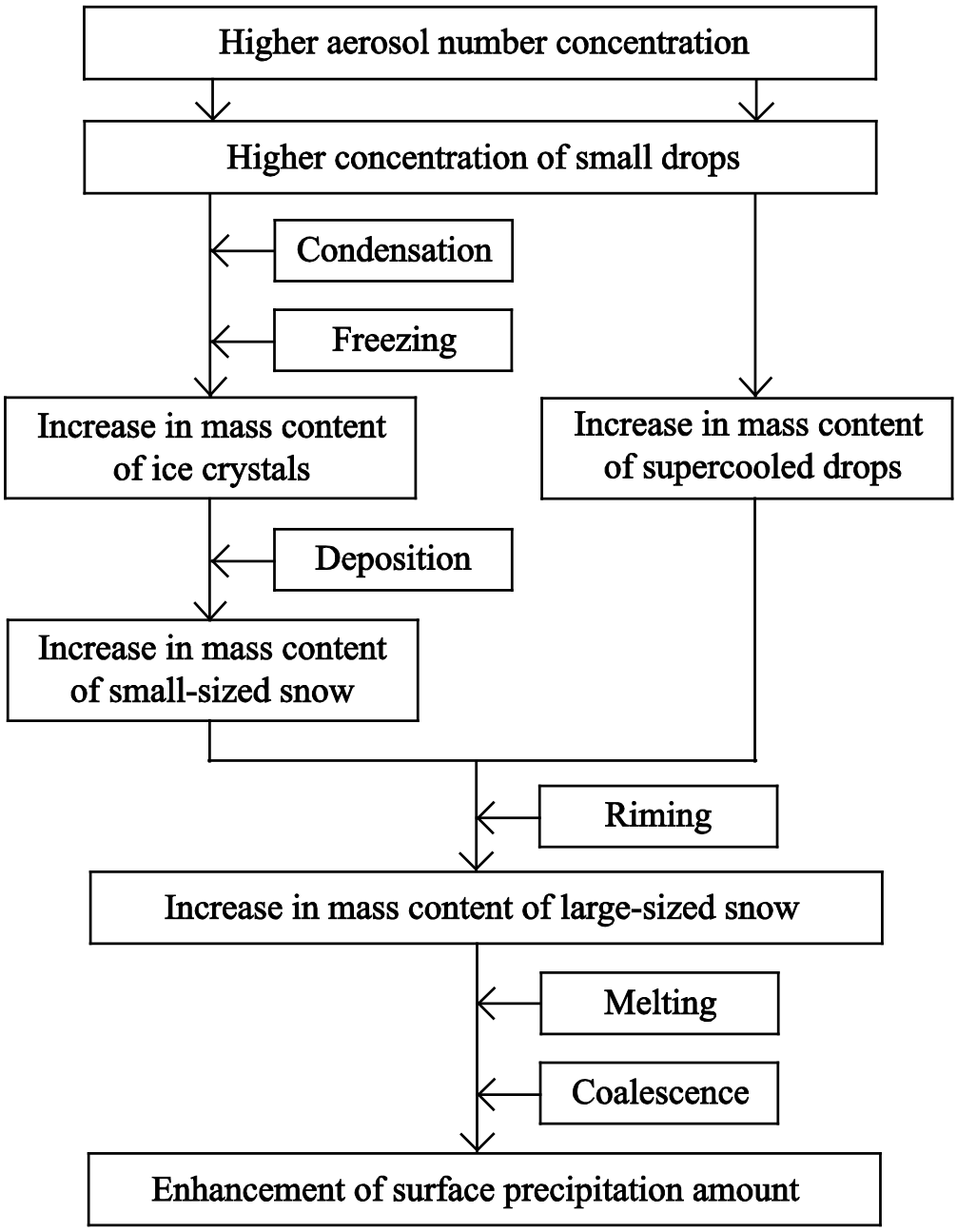

Figure 4.8. Schematic diagram of main pathways of microphysical processes that lead to larger surface precipitation amount for higher aerosol number concentration.

seems to be not favorable since the drop mass content is smaller.

Figure 4.8 presents a schematic diagram that depicts microphysical processes and changes in hydrometeor mass contents that lead to larger accumulated surface precipitation amount for higher aerosol number concentration in the aerosol number concentration range of N_0 = 600–4800 cm^{-3}. For higher aerosol number concentration, more drops of small sizes form. More drops of small sizes grow through stronger condensation due to a larger sum of the surface areas of drops while being transported upward and some of them freeze, which leads to an increase in the mass content of ice crystals. The increased ice crystal mass content leads to an increase in the mass content of small-sized snow particles largely through deposition. The increased mass content of small-sized snow particles leads to an increase in the mass content of large-sized snow particles largely through riming. Moreover, more drops of small sizes is responsible for an increase in the mass content of supercooled drops above the freezing level. The increased supercooled drop mass content leads to an increase in the mass content of large-sized snow particles through riming. More snow particles of large sizes, which form in these pathways, contribute to an increase in the amount of surface precipitation through melting and collision-coalescence.

4.4. Summary and conclusions

This study investigates the impacts of changes in aerosol loading on surface precipitation from mid-latitude deep convective systems through simulations of a real case. For this, a precipitation event that occurred over north central Mongolia on 21

August 2014 was selected and simulations were performed with different initial aerosol number concentrations using the WRF model coupled with an updated bin microphysics scheme. The improved quasi-stochastic collection model which considers multiple collisions of cloud particles within a model time step is implemented in the bin microphysics scheme. It was found that the behavior of 24-h accumulated surface precipitation amount with aerosol number concentration is not monotonic. The 24-h accumulated surface precipitation amount slightly decreases with increasing aerosol number concentration in the range of N_0 = 150–600 cm^{-3}, while it notably increases with increasing aerosol number concentration in the range of N_0 = 600–4800 cm^{-3}. The 24-h accumulated surface precipitation amount in the case of N_0 = 4800 cm^{-3} is 22% larger than that in the case of N_0 = 600 cm^{-3}. Based upon the results of the analysis of mass contents and number concentrations of hydrometeors, mass change rates of hydrometeors and water vapor due to microphysical processes, and size distributions of hydrometeors, provided explanations of why the accumulated surface precipitation amount increases with increasing aerosol number concentration in the range of N_0 = 600–4800 cm^{-3}.

This study does not try to explain why the 24-h accumulated surface precipitation amount slightly decreases with increasing aerosol number concentration in the range of N_0 = 150–600 cm^{-3}. Changes in hydrometeor mass contents and main responsible microphysical processes might be different from those depicted in Fig. 4.8. The impacts of aerosol loading on surface precipitation in the low aerosol concentration regime deserve an investigation. For this, additional simulations with much lower

aerosol number concentrations are required. To further enhance our understanding of aerosol impacts on precipitation, more studies of real-case simulations in various geographical regions as well as well-designed idealized simulations using advanced numerical models need to be carried out. The present study is such an attempt. It reports the impacts of changes in aerosol loading on surface precipitation amount over north central Mongolia which is a high-altitude, inland region.

5. A Hail climatology in Mongolia

5.1. Introduction

Hailstorms have received much attention because of their disastrous impacts and distinct cloud microphysical aspects such as extreme riming process. A Hailstorm is meso-γ scale convective phenomenon, which can cause considerable damage to crops, livestock, houses, and even humans (Cao, 2008). Hailstones are produced through extreme riming in convective clouds. The diameter of a hailstone is typically ~1 cm, but hailstones of 10–15 cm have also been observed (Houze, 2014). The microphysics of hailstones and the dynamics of storms that can produce hailstones have been extensively studied in recent decades (see Pruppacher and Klett, 1997 and Houze, 2014). Moreover, the long-term climatology of hail in many regions of the world has been documented (Table 5.1).

Previous studies of long-term hail climatology are summarized in Table 5.1. Here, only studies that used hail observation data spanning at least 10 years are considered. The third column of Table 5.1 indicates the trend of annual hail frequency. In some regions of the world, the annual hail frequency exhibits an increasing trend (e.g., Suwala and Bednorz, 2013; Cao, 2008), while in other regions, it exhibits a decreasing trend (e.g., Li et al., 2016; Jin et al., 2016). Moreover, there are regions that show no clear trend with regard to the annual hail frequency (e.g., Giaiotti et al., 2003; Simeonov et al., 2009; Berthet et al., 2011). These results imply that the temporal and

Study area	References	Annual trend
Asia		
China	Zhang et al. (2008)	
	Li et al. (2016)	decrease
North Korea	Kim and Ni (2015)	decrease
South Korea	Jin et al. (2016)	decrease
Turkey	Kahraman et al. (2016)	increase since 2005
Europe		
Alpine region	Nisi et al. (2016)	decrease since 2009
Bulgaria	Simeonov (2009)	unclear
Central Europe	Suwala & Bednorz (2013)	increase since the late 1990s
Finland	Tuovinen et al. (2009)	unclear
France	Dessens (1986)*	unclear
	Vinet (2001)	
	Berthet et al. (2011)	unclear
Germany	Kunz et al. (2009)	increase
Greece	Kotinis-Zambakas (1989)	
	Sioutas et al. (2009)*	unclear
Italy	Giaiotti et al. (2003)*	unclear
	Baldi et al. (2014)	
Romania	Burcea et al.(2016)	region-dependent
United Kingdom	Webb et al. (2001)	unclear
North America		
Canada	Etkin and Brun (1999)	unclear
	Cao (2008)*	increase
United States	Changnon (1977)	region-dependent
	Changnon &Changnon (2000)	decrease since 1970s
	Schaefer et al. (2004)	unclear
South America		
Argentina	Mezher et al. (2012)	region-dependent
Oceania		
Australia	Schuster et al. (2005)	unclear

Table 5.1. Previous studies of long-term (here spanning at least 10 years) hail climatology. Study area, references, and annual trend are listed. The stars (*) in references indicate that the study area is the part of the country. Annual trend is written as “unclear” when the annual trend is too weak to determine or when it is mentioned in the study that the annual trend is affected by the inhomogeneity of data. Annual trend is written as “region-dependent” when the annual trend is an increase or a decrease depending on regions of the country.

spatial characteristics of hail differ, depending upon the geographical location and regional atmospheric flow/circulation features. Some attempts have been made to connect the trend of annual hail frequency to thermodynamic factors. Kunz et al. (2009) established a relationship between the annual hail frequency and convective indices depending on temperature and moisture in the lowest layer. Li et al. (2016) attributed the decrease of annual hail frequency in northern China to the increase of convective inhibition (CIN) as well as weakened synoptic troughs in East Asia. Jin et al. (2017) related the decrease of annual hail frequency in South Korea to the increase of freezing-level height and the decrease of vertical wind shear.

Hartmann et al. (2013) noted that it is difficult to describe climate change-related trends of small-scale severe weather phenomena, such as hailstorms, because of the inhomogeneity of the observational data. For example, the trend of annual hail frequency in Tuovinen et al. (2009) is described as “unclear” in Table 5.1 in spite of an apparent increase since the late 1990s because the increasing trend is partially attributed to the more efficient collection of reports by the Finnish Meteorological Institute.

Mongolia experiences frequent hailstorms, sometimes with hailstorm-related damage. Geographically, Mongolia is located at a high altitude (85% of the country exceeds 1000 m in elevation), with rolling plateaus that occupy a large portion of the country. There are mountain ranges in the western and northern parts of Mongolia, the Gobi Desert in the southern part, and grasslands in the eastern part (Figure 5.1). Moreover, Mongolia has been considerably affected by climate change, experiencing an annual mean near-surface temperature increase of 2.14°C during the past 70 years

(Dagvadorj et al., 2009). These geographical and climatic features can provide the distinctive temporal and spatial characteristics of hail frequency in Mongolia, which is the motivation behind the present study.

In this study, a long-term hail climatology in Mongolia is documented, presenting the temporal and spatial distributions of hail frequency. In addition, hail frequency is related to thermodynamic factors such as CAPE, temperature lapse rate between 700 and 500 hPa, mixing ratio averaged over the lowest 100 hPa layer, and freezing-level height. In chapter 5.2, the data used in this study are described. In chapter 5.3, the analysis results are presented and discussed. In chapter 5.4, a summary is given.

5.2. Data

The first systematic meteorological observation network of Mongolia was established in 1936. However, the observation periods of some observatories were not continuous for hail records before 1984. For the homogeneity of data, use the hail observation dataset for the period of 1984–2013 provided by the National Agency for Meteorology and Environment Monitoring of Mongolia. Figure 5.1 shows the locations of 61 meteorological observatories which have been fully operational during the 30-year period of 1984–2013. The dataset includes information on the time and duration of hail occurrence, which was recorded manually. Hail is recorded only if hailstones fall inside the observation area. Observers in Mongolia distinguish hail based on the definition of hail, a type of precipitation in the form of balls or lumps of ice (Changnon, 1977),

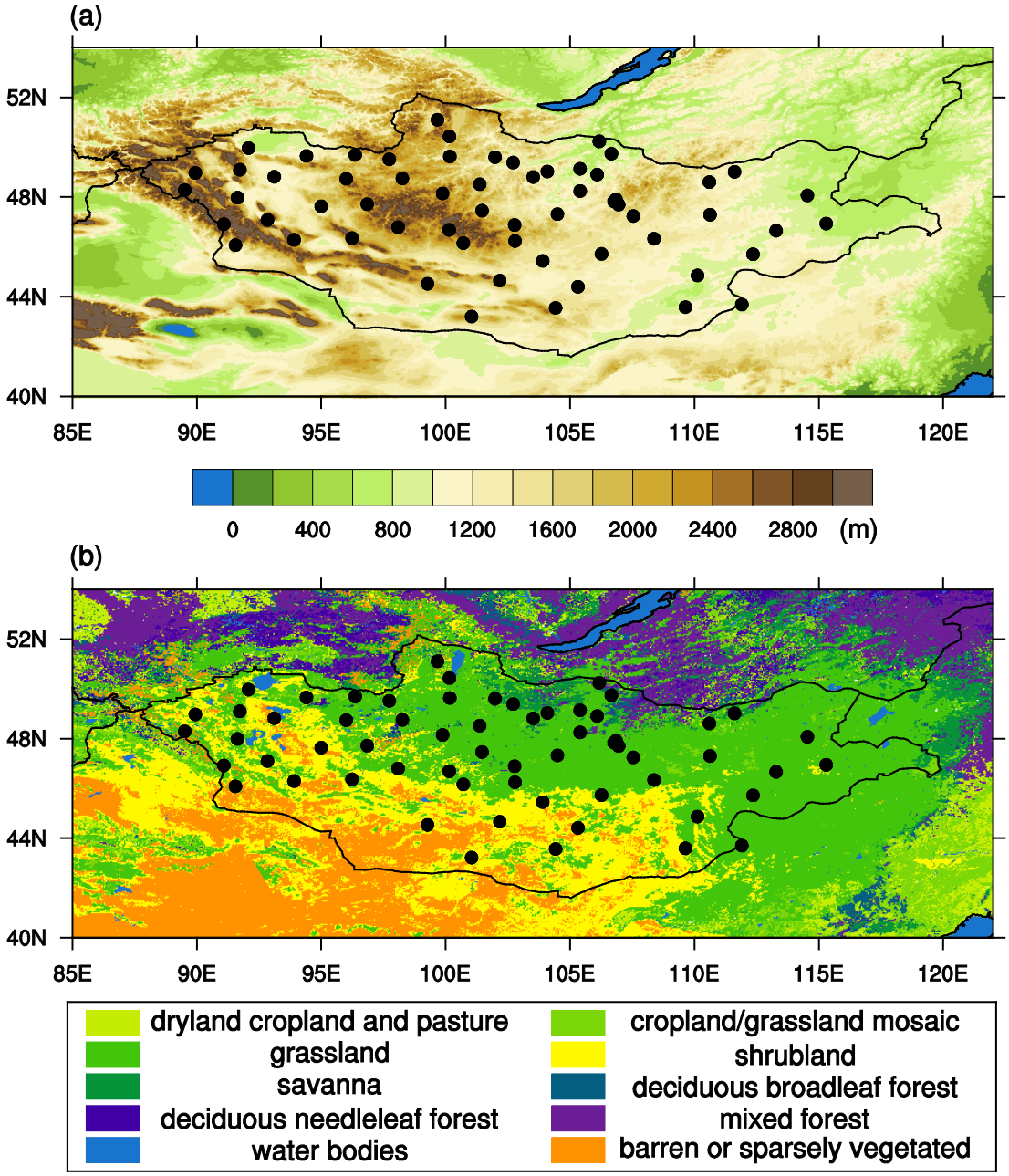
(a)
52N
48N
44N
40N
85E
90E
95E
100E
105E
110E
115E
120E
0
400
800
1200
1600
2000
2400
2800
(m)
(b)
dryland cropland and pasture
grassland
savanna
deciduous needleleaf forest
water bodies
cropland/grassland mosaic
shrubland
deciduous broadleaf forest
mixed forest
barren or sparsely vegetated

Figure 5.1. (a) Terrain height and (b) land use in Mongolia. Locations of 61 meteorological observatories are indicated in closed circles. Information on the terrain height and land use is from the United States Geological Survey (USGS).

although a specific diameter criterion is not provided.

To represent hail frequency in this study, a hail day is defined as a day during which hail was observed one or more times at an observatory, and the term “hail frequency” in this study means the frequency of hail days. Moreover, to describe hail frequency at an observatory, the annual mean hail frequency and the monthly mean hail frequency are defined following Zhang et al. (2008) and Jin et al. (2017). The annual mean hail frequency is the average number of hail days at an observatory per year (i.e., the number of hail days at the observatory divided by the number of years), while the monthly mean hail frequency is the average number of hail days at an observatory during each month per year (i.e., the number of hail days in a particular month at the observatory divided by the number of years).

To examine the relationship between hail frequency and thermodynamic factors in Mongolia, atmospheric sounding data are required. However, only one station (Ulaanbaatar) has launched radiosondes regularly in Mongolia during the last 30 years. Therefore, instead of using radiosonde data, the ERA-Interim reanalysis data provided by the European Centre for Medium-Range Weather Forecasts are used. The reanalysis data are interpolated to the locations of the 61 meteorological observatories. Then, the aforementioned thermodynamic factors (i.e., CAPE, 700–500 hPa temperature lapse rate, average water vapor mixing ratio in the lowest 100 hPa layer, and freezing-level height) are calculated.

The ERA-Interim reanalysis data contain atmospheric thermodynamic data in time intervals of four times a day [0200, 0800, 1400, and 2000 local standard time

(LST)]. The hail occurrence in Mongolia is extremely concentrated in the afternoon (see Figure 5.4). Therefore, only the data at 1400 LST are chosen to calculate the thermodynamic factors on hail days. Moreover, for reasonable comparison of the thermodynamic factors between all days and hail days, only the data at 1400 LST are also chosen to calculate the thermodynamic factors on all days.

5.3. Results and discussion

5.3.1 Temporal and spatial characteristics

A total of 1358 hail days were reported from the 61 meteorological observatories in Mongolia for the period of 1984–2013. Hence, the annual mean hail frequency averaged over all observatories and the entire period is 0.74 (i.e., 0.74 hail days per year on average). The annual mean hail frequency in Mongolia is relatively low compared to that in Inner Mongolia in China averaged over the period 1961–2005 (Zhang et al., 2008), which is located southeast of Mongolia.

Figure 5.2 shows the annual variation of the number of hail days. Although the number of hail days exhibits large fluctuations, it clearly shows an annually decreasing trend, particularly since 1993. The decreasing trend of hail days is also evident in China (Xie et al., 2008; Li et al., 2016), United States (Changnon and Changnon, 2000), North Korea (Kim and Ni, 2015), and South Korea (Jin et al., 2017). Using the linear regression method, it is found that the decreasing rate of the annual number of hail days

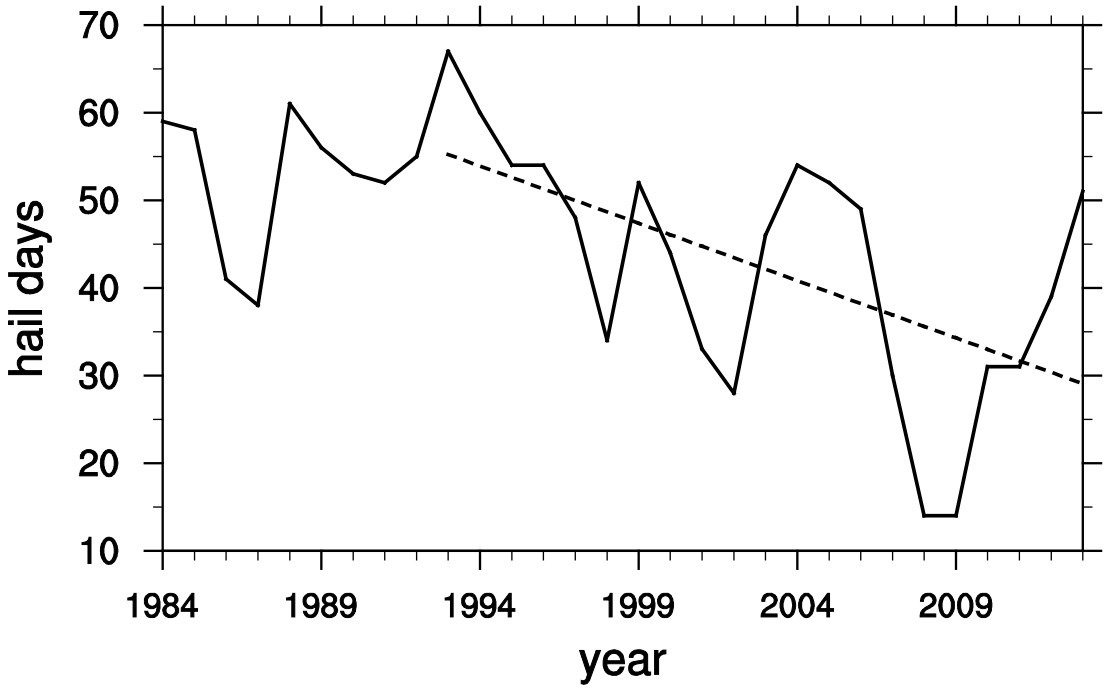

Figure 5.2. Annual variation of the number of hail days. The dashed line indicates the linear trend since 1993.

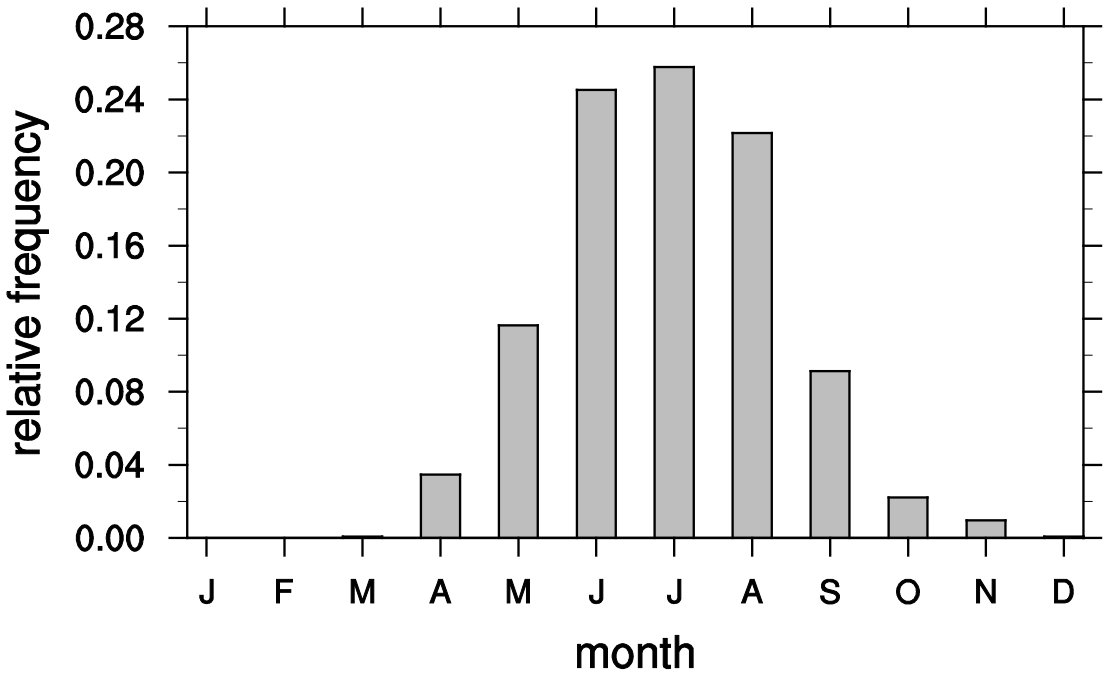

Figure 5.3. Monthly variation of relative frequency of hail days.

since 1993 is 0.214 per decade and statistically significant at the significance level of 95% (see the dashed line in Figure 5.2).

Figure 5.3 shows the monthly variation of monthly mean hail frequency averaged over all observatories. The monthly variation is represented in terms of the relative frequency of hail days, which is the total hail days in a certain month divided by the total hail days in the entire period. Seventy-two percent of the total hail days are concentrated in summer (June, July, and August). The high hail frequency in summer is commonly observed in inland regions (central United States: Changnon, 1977; north central China: Zhang et al., 2008; parts of inland Europe: Punge and Kunz, 2016). Hail is rarely observed in winter (December, January, and February) and March due to the strong influence of the Siberian high. Some studies have reported that hail is most frequent in April or October/November in some regions mainly due to the large instability in the middle level of the troposphere (southern China: Zhang et al., 2008; South Korea: Jin et al., 2017), while only 7% of the total hail days occur in April, October, and November in Mongolia.

The diurnal variation of the relative frequency of hail occurrence is shown in Figure 5.4. It is noted that multiple hail occurrence in one hail day is taken into account to examine the diurnal variation of hail occurrence. Hail occurrence is mostly concentrated in the afternoon and early evening. The maximum relative frequency of hail occurrence is 0.147 at 1600–1700 LST. Eighty-nine percent of the total hail events occur between 1200 and 2100 LST. Strong daytime solar radiation raises the near-surface temperature, resulting in the increase of the temperature lapse rate. The induced

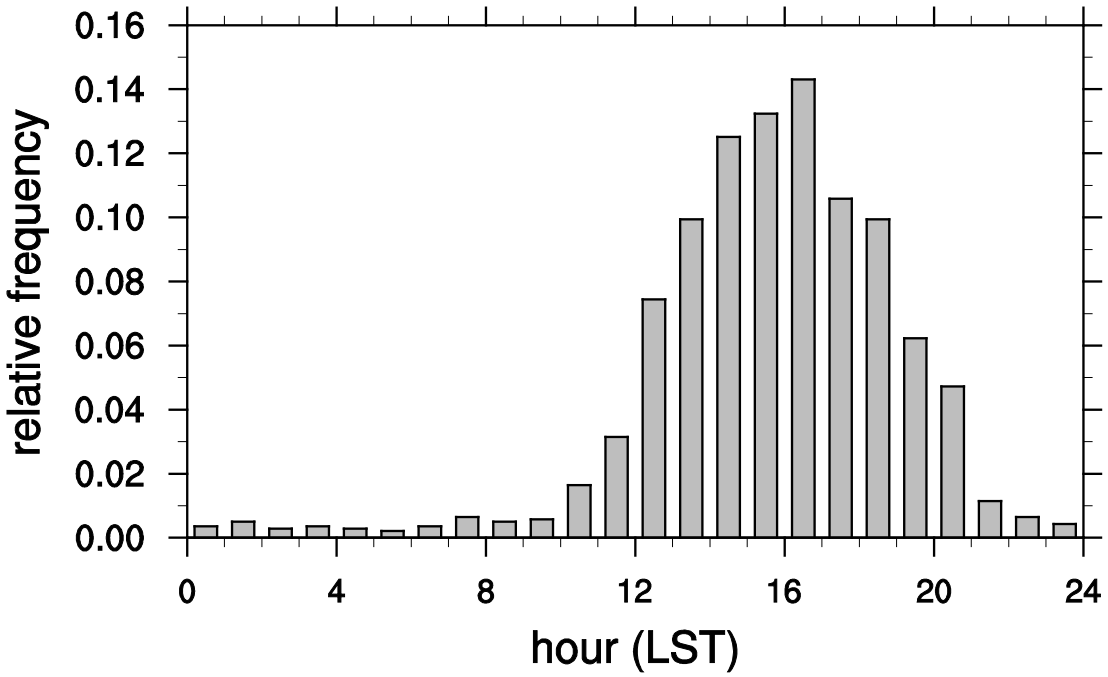

Figure 5.4. Diurnal variation of relative frequency of hail occurrence.

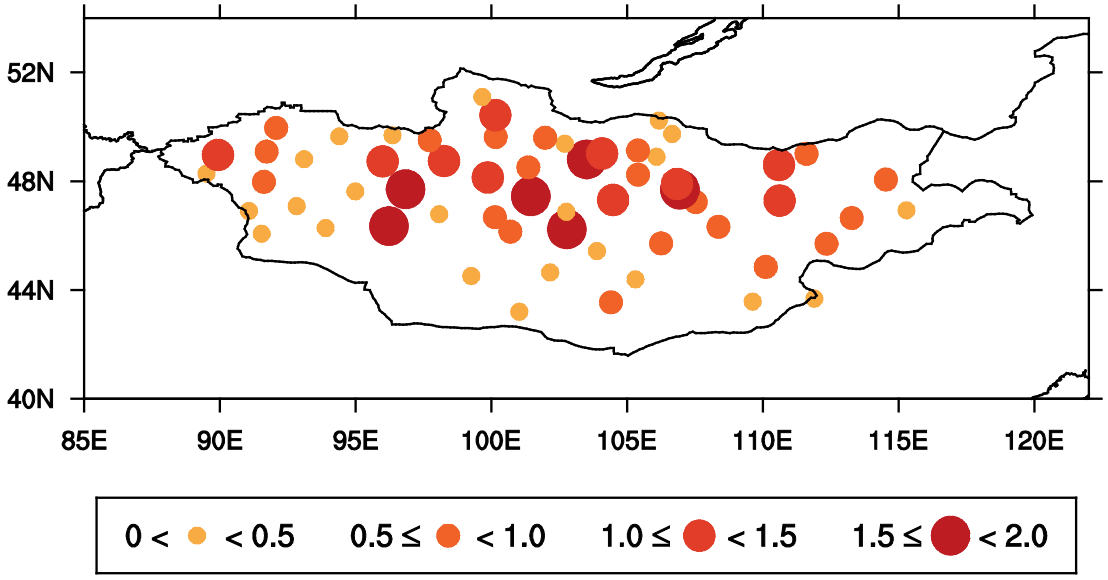

Figure 5.5. Spatial distribution of annual-mean hail frequency.

atmospheric instability provides a favorable condition for convection, which may be a main reason for the high hail frequency in the afternoon (Punge and Kunz, 2016).

Figure 5.5 illustrates the spatial distribution of annual mean hail frequency in Mongolia. In the northern region of the country, where most of the land is grassland and the overall terrain height is relatively high (Figure 5.1), the annual mean hail frequency exhibits a high spatial variability. At some observatories in the northern region of the country, the annual mean hail frequency is higher than 1, while at the other observatories of this region, the annual mean hail frequency is less than 0.5. In the northern region of the country, even if the distance between two observatories is close, the annual mean hail frequency tends to show a large difference. However, it should be noted that a large number of observatories with relatively high hail frequency are located in the north central region of the country, where almost all of the land is mountainous or covered by grassland. Mountainous terrain can divert flows and cause low-level flow convergence, parts of which may contribute to a high hail frequency (Nisi et al., 2016). The high hail frequency in the north central region may have been affected by the orography and relatively wet atmospheric condition compared to the western and southern regions covered by shrubland or desert (see Figure 5.1b). In contrast to the north central region, hail seldom occurs in the southern region of the country, where most of the region is desert (the Gobi Desert). The annual mean hail frequency in the southern region is generally less than 0.5. The extremely dry conditions are largely responsible for the low annual mean hail frequency in the southern region, because hail is less likely to occur in dry conditions (see Figure 5.7c).

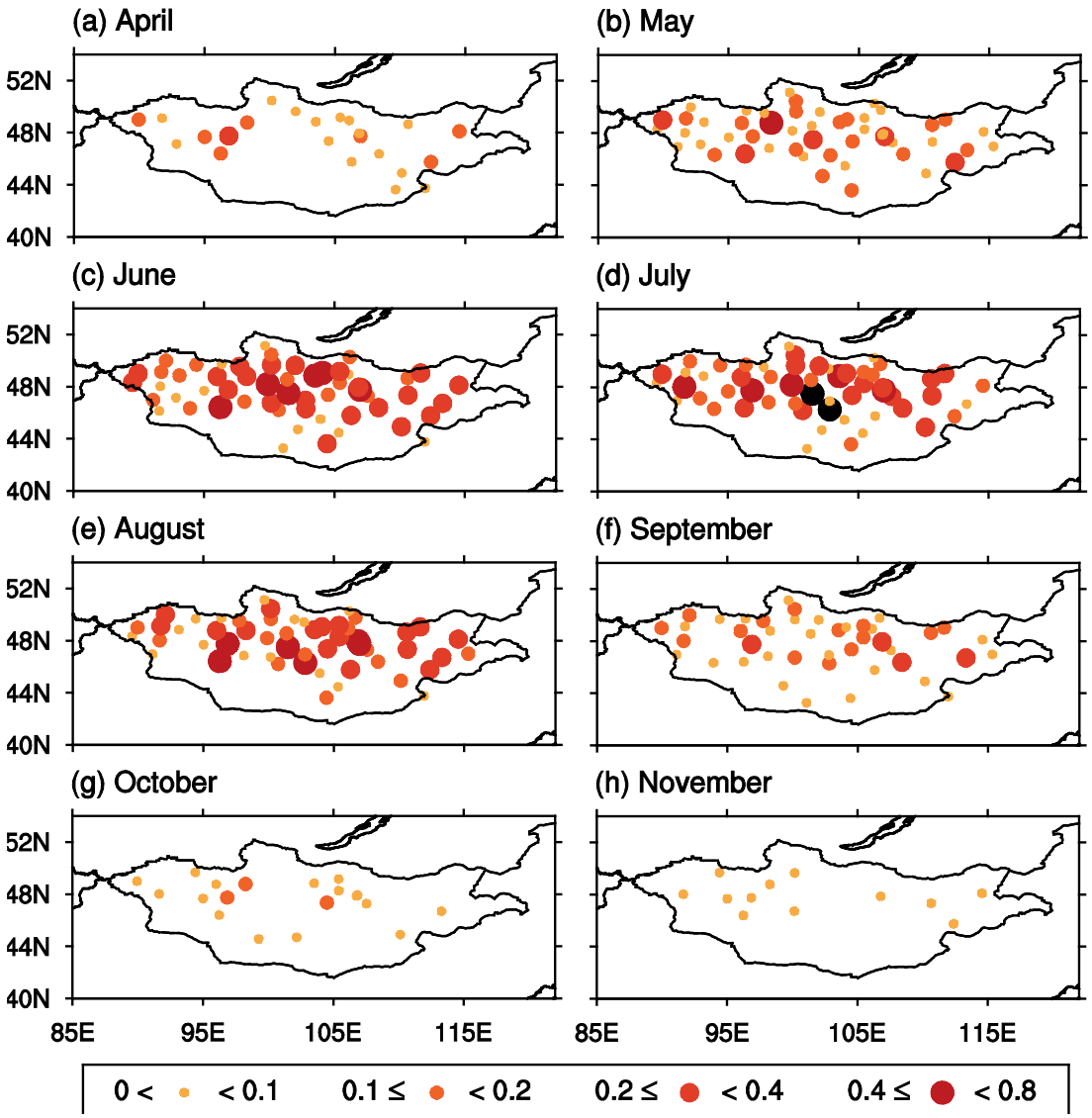

Figure 5.6. Spatial distributions of monthly mean hail frequency in (a) April, (b) May, (c) June, (d) July, (e) August, (f) September, (g) October, and (h) November. The black circles in (d) are Arvaikheer (46.26°N, 102.79°E) and Tsetserleg (47.47°N, 101.46°E) which exhibit the highest monthly mean hail frequency in July, 0.77.

Figure 5.6 illustrates the spatial distributions of monthly mean hail frequency in each month, from April to November. Hail events are observed in April, except in the southern desert region. In May, the hail frequency increases at almost all observatories, with a few observatories showing the maximum monthly mean hail frequency [e.g., Tosontsengel (48.76^{o}N, 98.26^{o}E), with a maximum monthly mean hail frequency of 0.43]. Throughout the country, the monthly mean hail frequency is generally the highest in June, July, and August. The maximum monthly mean hail frequency reaches 0.77 at Arvaikheer and Tsetserleg (black circles in Figure 5.6d) in July. The monthly mean hail frequency decreases drastically beginning in September at almost all observatories. In October and November, the monthly mean hail frequency is less than 0.2 at all observatories.

5.3.2 Relations to thermodynamic factors

Many thermodynamic and dynamic factors that affect hail occurrence are known. These factors include CAPE, temperature lapse rate, low-level moisture supply, freezing-level height, vertical wind shear, jet stream, and cold fronts (e.g., Dessens, 1986; Vinet, 2001; Zhang et al., 2008; Tippett et al., 2015; Jin et al., 2017). To examine possible links between the characteristics of hail frequency in Mongolia and thermodynamic factors, CAPE, the temperature lapse rate between 700 and 500 hPa, the water vapor mixing ratio averaged over the lowest 100 hPa layer, and the freezing-level height are considered in this study.

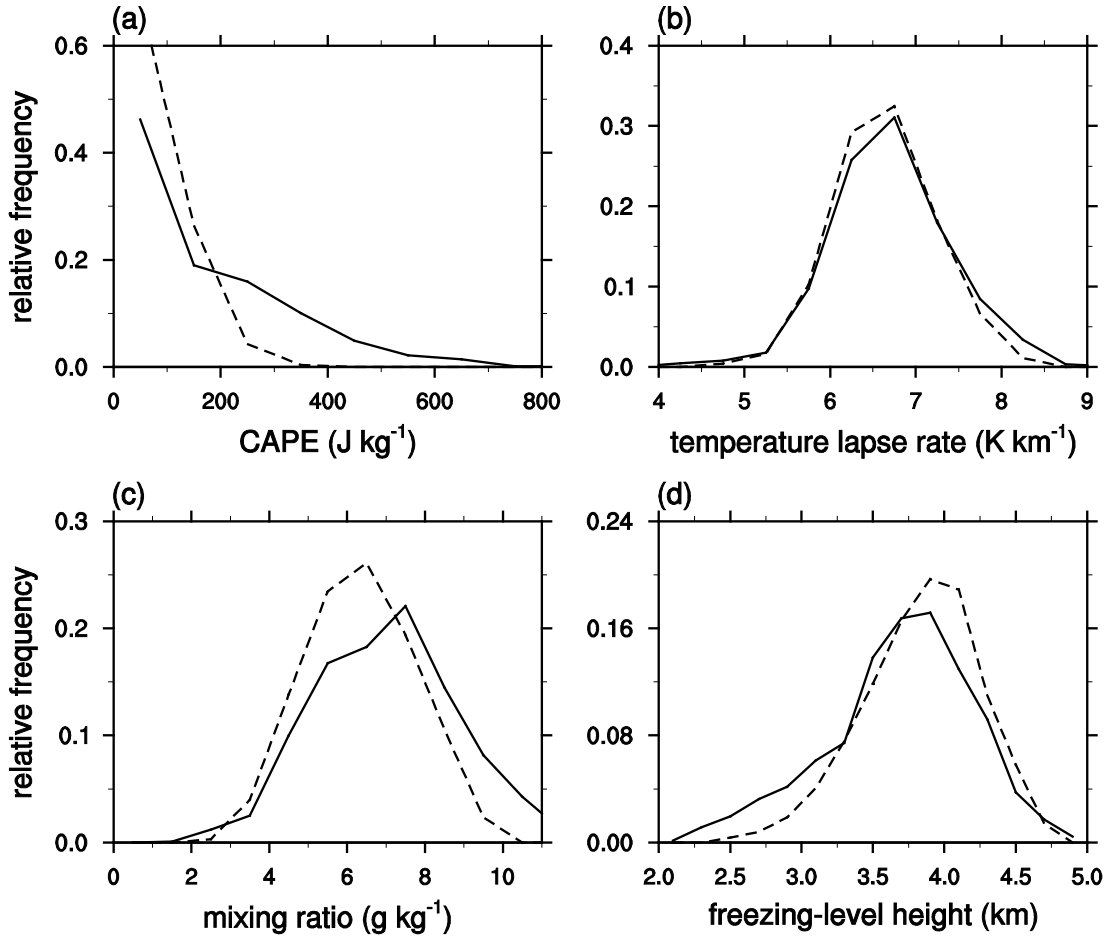

Figure 5.7. Relative frequency distributions of (a) CAPE, (b) the temperature lapse rate between 700 and 500 hPa, (c) the water vapor mixing ratio averaged over the lowest 100 hPa layer, and (d) the freezing-level height in summer. Solid and dashed lines indicate the hail days and all days, respectively.

Figure 5.7 shows the relative frequency distributions of thermodynamic factors calculated on hail days and all days of June, July, and August. It is observed that the relative frequency for large CAPE, large low-level water vapor mixing ratio, and low freezing-level height is higher on hail days than on all days. That is, CAPE is larger, the low-level water vapor mixing ratio is larger, and the freezing-level height is lower on hail days than on all days in summer. The mean CAPEs averaged over hail days and over all days are 161.2 and 79.1 J kg^{-1}, respectively. The mean low-level water vapor mixing ratios averaged over hail days and over all days are 7.05 and 6.34 g kg^{-1}, respectively. The freezing-level height averaged over hail days and over all days are 3680 and 3842 m, respectively. Therefore, it can be said that large CAPE, large low-level water vapor mixing ratio, and low freezing-level height are related to the high hail frequency in summer. The midlevel temperature lapse rate is also known to affect hail occurrence in some regions of the world (Farnell and Llasat, 2013; Allen et al., 2015; Jin et al., 2017). Figure 5.7b shows that the relative frequency for large midlevel temperature lapse rate is slightly higher on hail days than on all days. However, the difference is small, with no statistical significance. It seems that the midlevel temperature lapse rate has little relationship with the hail occurrence in Mongolia. The midlevel temperature lapse rates averaged over hail days and over all days are 6.71 and 6.65 K km^{-1}, respectively.

The monthly variations of the thermodynamic factors on all days are shown in Figure 5.8. As expected, CAPE and the low-level water vapor mixing ratio exhibit their peaks in July, which might affect the maximum hail frequency in July. The freezing-

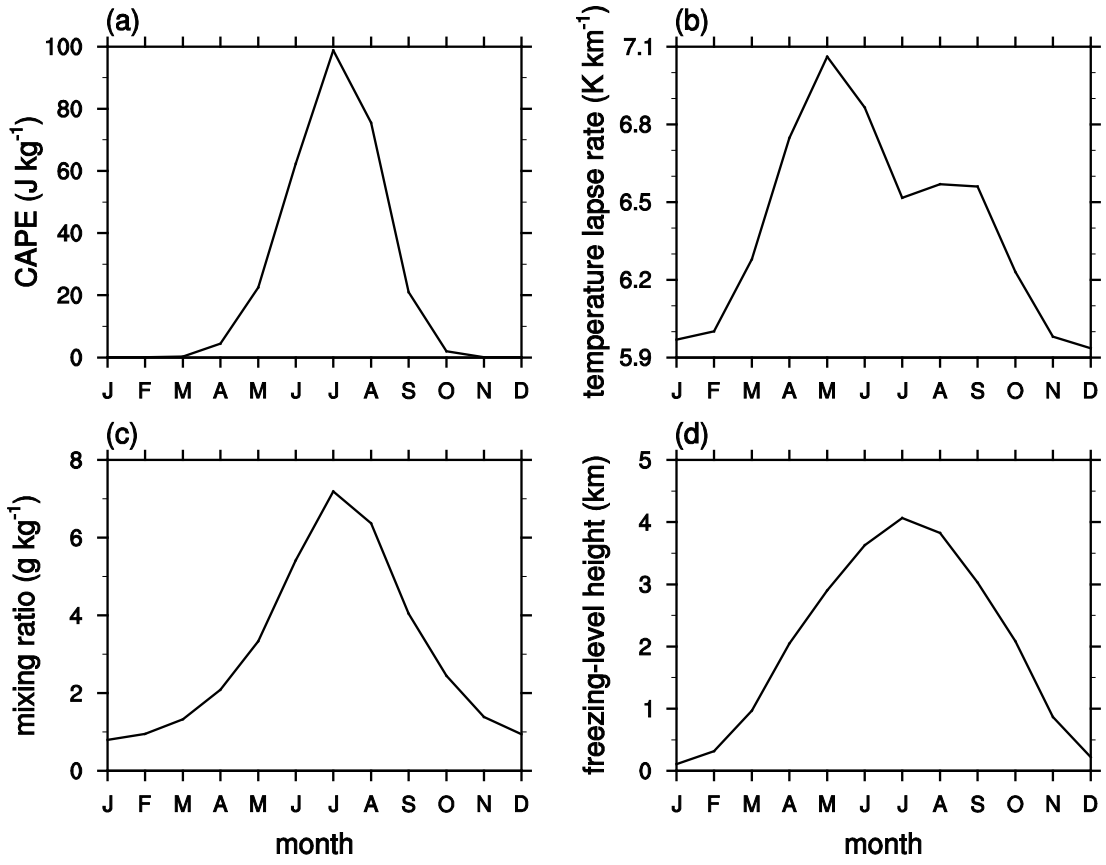

Figure 5.8. Monthly variations of (a) CAPE, (b) the midlevel temperature lapse rate, (c) the low-level water vapor mixing ratio, and (d) the freezing-level height on all days.

level height is the highest in July due to warm air. CAPE and the low-level water vapor mixing ratio play important roles in the high hail frequency in summer. CAPE and low-level water vapor amount are also important factors to summer precipitation. It is noted that precipitation shows a maximum in summer in Mongolia (Doljinsuren and Gomes, 2015), and heavy rainfall in Mongolia is occasionally accompanied by hail occurrence (Goulden et al., 2016). To investigate common and different atmospheric conditions for hail occurrence and heavy rainfall, further research examining thermodynamic/dynamic factors is needed. The midlevel temperature lapse rate peaks in May, possibly due to the frequent passage of cold fronts (Jambaajamts, 1989). However, the hail frequency in May is not very high. The midlevel temperature lapse rate shows a local minimum in July, during which the hail frequency is the highest. It seems that the monthly variation of hail frequency is largely affected by CAPE and the low-level water vapor mixing ratio, whereas the midlevel temperature lapse rate does not show any significant relationship with the hail frequency. It is hypothesized that hail occurrence is generally attributed to both low-level water vapor amount and atmospheric instability such as midlevel temperature lapse rate. Because of the relatively dry atmospheric condition of the country, the relative importance of the midlevel temperature lapse rate is small compared to that of the low-level water vapor mixing ratio. This could be a possible reason for the different monthly variation of hail occurrence in Mongolia from that in wetter regions (e.g., southern China: Zhang et al., 2008; North Korea: Kim and Ni, 2015; South Korea: Jin et al., 2017). Further research is needed to quantify the importance of the midlevel temperature lapse rate.

Besides thermodynamic factors, there could be dynamic factors or atmospheric circulations that are related to hail occurrence in Mongolia. Li et al. (2016) discussed that the weakened 850-hPa meridional wind is responsible for the decreasing trend of annual hail frequency in northern China, which is close to Mongolia. Vertical wind shear is known to be related to the development of supercell storms that can produce severe weather (Groenemeijer and van Delden, 2007; Jin et al., 2017). Two additional factors, that are the low-level meridional wind and the vertical wind shear, are examined for hail days and all days. It is revealed that the average low-level horizontal wind in summer in Mongolia is weak. The weak circulation in summer is less likely to affect the change of annual hail frequency significantly. It is also revealed that there is no noticeable relationship between the vertical wind shear and hail occurrence in Mongolia.

To examine the relationship between the decreasing trend of the number of annual hail days in Mongolia (Figure 5.2) and thermodynamic factors, the annual variations of the thermodynamic factors averaged over the entire year and over summer are shown in Figure 5.9. CAPE exhibits a decreasing trend. Since CAPE is very small in the other seasons (Figure 5.8a), the decreasing trend in CAPE is mainly due to the decrease in CAPE in summer (Figure 5.9b). The low-level water vapor mixing ratio also exhibits a decreasing trend, which becomes clear in the 2000s. The freezing-level height in summer exhibits an increasing trend, although its annual variation is somewhat large. Therefore, the changing trends of CAPE, the low-level water vapor mixing ratio, and the freezing-level height seem to be closely related to the decreasing trend of the number of annual hail days, whereas the midlevel temperature lapse rate increases

slightly annually, which might act to increase hail occurrence.

Scatter plots of the number of hail days and the thermodynamic factors averaged over summer are shown in Figure 5.10. All the correlations between the thermodynamic factors and the number of hail days are statistically significant at the significance level of 95%. CAPE and the low-level water vapor mixing ratio show positive correlations with the number of hail days, i.e., the number of hail days tends to be larger in the years with larger CAPE and larger low-level water vapor mixing ratio. The correlation coefficients of CAPE and the low-level water vapor mixing ratio with the number of hail days are 0.40 and 0.45, respectively. The freezing-level height shows a negative correlation with the number of hail days, which indicates that the increase in freezing-level height is related to the decrease in the number of hail days. The correlation coefficient between the freezing-level height and the number of hail days is –0.47. The midlevel temperature lapse rate is negatively correlated with the number of hail days, i.e., the number of hail days tends to be smaller in the years with larger midlevel temperature lapse rate. This is in opposition to the previous result which indicates that the large midlevel temperature lapse rate might result in high hail frequency (e.g., Jin et al., 2017). More detailed analysis is needed to clarify the relationship between midlevel temperature lapse rate and hail frequency.

5.4. Summary

This study examines the long-term hail climatology in Mongolia and its association with the thermodynamic environment using the hail observation data from

61 meteorological observatories for 1984–2013. The average number of annual hail days is 0.74, and exhibits a decreasing trend. Seventy-two percent of the total hail days are concentrated in summer, and 89% of the total hail events are observed between 1200 and 2100 LST. Observatories where relatively frequent hail events are observed are concentrated in the central northern region. On the other hand, hail events are observed less frequently in the southern desert region. In summer, CAPE and the low-level water vapor mixing ratio are larger on hail days than on all days, while the relationship between the hail frequency and the 700–500 hPa temperature lapse rate is not clear. CAPE and the low-level water vapor mixing ratio show an annually decreasing trend, while the freezing-level height shows an annually increasing trend. These trends are responsible for the annually decreasing trend of the number of hail days in Mongolia.

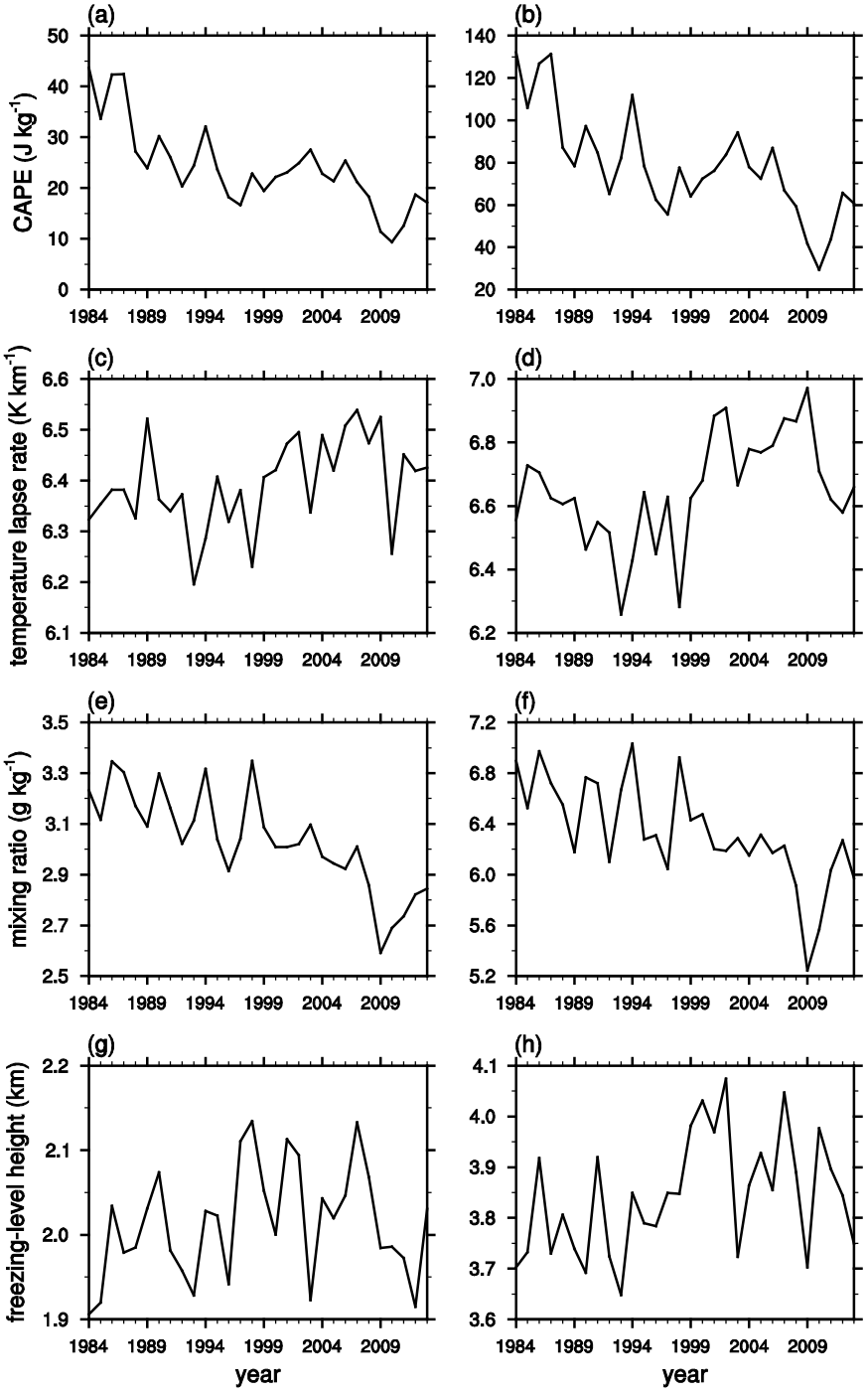
(a)
(b)
(c)
(d)
(e)
(f)
(g)
(h)
CAPE (J kg-1)
temperature lapse rate (K km-1)
mixing ratio (g kg-1)
freezing-level height (km)
year
year
1984
1989
1994
1999
2004
2009

Figure 5.9. Annual variations of whole-year averaged (a) CAPE, (c) midlevel temperature lapse rate, (e) low-level water vapor mixing ratio, and (g) freezing-level height. (b), (d), (f), and (h) are the same as (a), (c), (e), and (g), respectively, but averaged over summer.

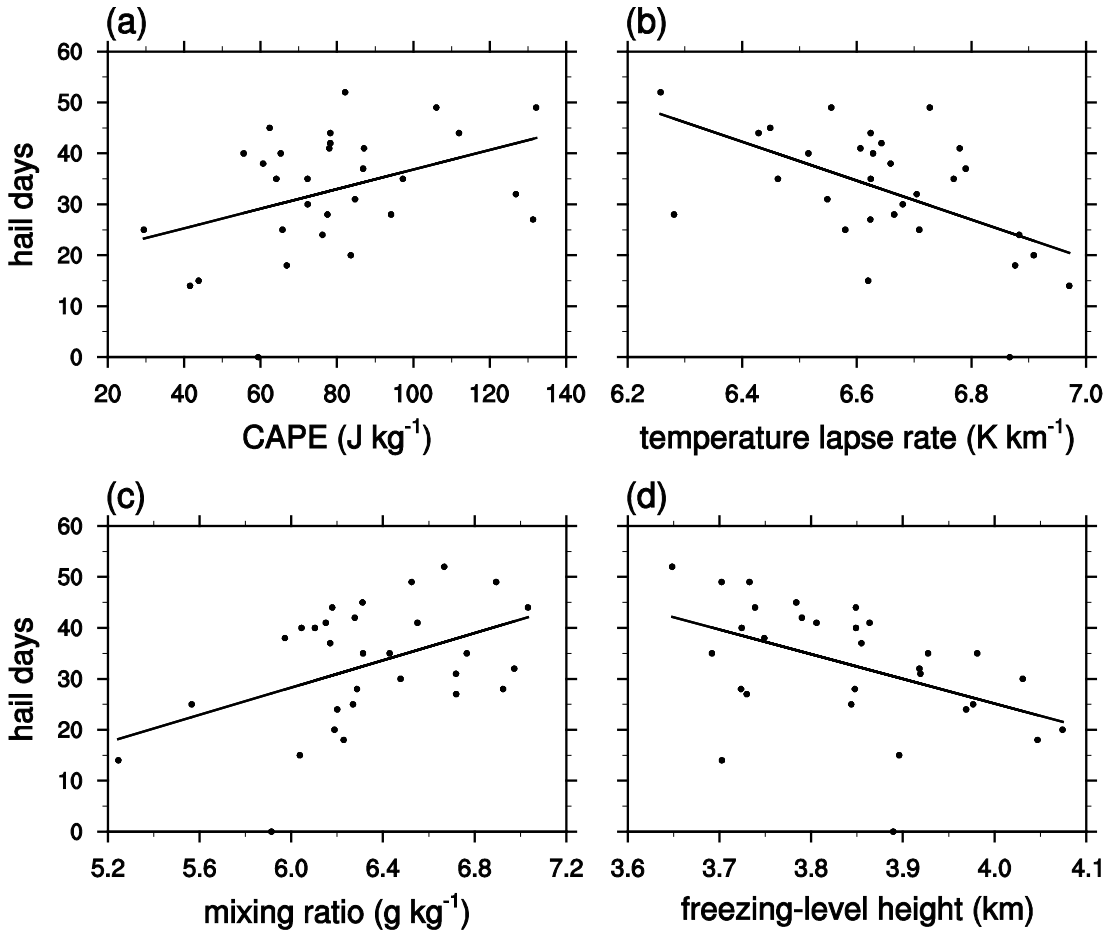

Figure 5.10. Scatter plots of the number of hail days and (a) CAPE, (b) the midlevel temperature lapse rate, (c) the low-level water vapor mixing ratio, and (d) the freezing-level height for each year. The thermodynamic factors are averaged over summer of each year.

6. Summary and conclusions

A quasi-stochastic model that solves the stochastic collection equation in a deterministic way describes the evolution of cloud drop size distribution due to the collision-coalescence process. We have derived an improved quasi-stochastic collection model (IQS model) by rigorously taking account of a finite model time step. The IQS model, which allows a large collector drop to collide with a small collected drop more than one time in a model time step, is evaluated and compared to the normal quasi-stochastic collection model (NQS model).

The box model results show that large drops tend to have larger sizes in the IQS model than in the NQS model and that the IQS model accelerates the formation of large drops compared to the NQS model. The IQS model is implemented in a detailed bin microphysics scheme that is coupled with the Weather Research and Forecasting (WRF) model. The idealized warm cloud simulation results confirm that the onset of surface precipitation is accelerated in the IQS model. These results help to explain to some extent fast raindrop formation in real-world cumuli. The performance of the IQS model in precipitation prediction is evaluated. For this, a precipitation event over north central Mongolia on 21 August 2014 is simulated. It is found that the surface precipitation amount is larger in the IQS model than in the NQS model, particularly over the strong precipitation region. This is attributed to the fact that the IQS model increases the mass contents of small drops and large drops due to multiple collisions. The impacts of aerosol loading on surface precipitation from mid-latitude deep convective systems over

north central Mongolia are examined. The surface precipitation amount notably increases in the range of N_0 = 600–4800 cm^{-3} (22% increase with eightfold aerosol loading). We have attempted to explain why the surface precipitation amount increases as the aerosol number concentration increases. Lastly, the long-term hail climatology in Mongolia is documented using the hail observation data from 61 meteorological observatories for 1984–2013.

This study demonstrates that the numerical model that includes an advanced bin microphysics scheme leads to better understanding of cloud and precipitation processes and more accurate prediction of precipitation. To further advance our current science of cloud and precipitation microphysics, developments of bin microphysics schemes and in-depth cloud and precipitation modeling works are needed.

Appendix: The detailed algorithm of the IQS model

In this appendix, the detailed algorithm of the IQS model is presented in a pseudo-code form as follows:

for $i = 1, 2, 3, \ldots, N$ **do**

for $j = 1, 2, 3, \ldots, i$ **do**

$p \leftarrow n_j \times K_{ij} \times \Delta t$

$x \leftarrow 0$

$p(x) \leftarrow e^{-p}$

$S_p \leftarrow p(x)$

loop

$x \leftarrow x + 1$

$p(x) \leftarrow p(x) \times p / x$

$\Delta n_i \leftarrow n_i \times p(x)$

$n_j \leftarrow n_j - x \times \Delta n_i$

$S_p \leftarrow S_p + p(x)$

$m(x) \leftarrow m_i + x \times m_j$

$M(x) \leftarrow m(x) \times \Delta n_i$

if $n_j \leq 0$ **or** $S_p > 1 - \varepsilon$ **then**

break out of loop

end if

end loop

$n_i \leftarrow n_i \times \{S_p - p(0)\}$

redistribute $M(x)$

end for

end for

Here, ε is a sufficiently small positive number, which is set to 10^{-5} in this study. All the other notations have the same meanings as in chapter 2.1. A simple algorithm to prevent n_j from being negative is applied. For the redistribution of $M(x)$, the method proposed in Bott (1998, 2000) is used, as for the NQS model.

References

Albrecht, B. A., 1989: Aerosols, cloud microphysics, and fractional cloudiness. *Science*, **245**, 1227–1230.

Alfonso, L., 2015: An algorithm for the numerical solution of the multivariate master equation for stochastic coalescence. *Atmos. Chem. Phys.*, **15**, 12,315–12,326.

Alfonso, L., G. B. Raga, and D. Baumgardner, 2013: The validity of the kinetic collection equation revisited-Part 3: Sol-gel transition under turbulent conditions. *Atmos. Chem. Phys.*, **13**, 521–529.

Alizadeh-Choobari, O., and M. Gharaylou, 2017: Aerosol impacts on radiative and microphysical properties of clouds and precipitation formation. *Atmos. Res.*, **185**, 53–64.

Allen, J. T., M. K. Tippett, and A. H. Sobel, 2015: An empirical model relating U.S. monthly hail occurrence to large-scale meteorological environment. *J. Adv. Model. Earth Syst.*, **7**, 226–243.

Baldi, M., V. Ciardini, J. D. Dalu, T. De Filippis, G. Maracchi, and G. Dalu, 2014: Hail occurrence in Italy: Towards a national database and climatology. *Atmos. Res.*, **138**, 268–277.

Bayewitz, M. H., J. Yerushalmi, S. Katz, and R. Shinnar, 1974: The extent of correlations in a stochastic coalescence process. *J. Atmos. Sci.*, **31**, 1604–1614.

Beard, K. V. , 1976: Terminal velocity and shape of cloud and precipitation drops aloft. *J. Atmos. Sci.*, **33**, 851–864.

Beard, K. V., and H. T. Ochs, 1993: Warm-rain initiation: An overview of microphysical mechanisms. *J. Appl. Meteorol.*, **32**, 608–625.

Berry, E. X., 1967: Cloud droplet growth by collection. *J. Atmos. Sci*., **24**, 688–701.

Berry, E. X., and R. L. Reinhardt, 1974: An analysis of cloud drop growth by collection: Part II. Single initial distributions. *J. Atmos. Sci.*, **31**, 1825–1831.

Berthet, C., J. Dessens, J. and L. Sanchez, 2011: Regional and yearly variations of hail frequency and intensity in France. *Atmos. Res*., **100**, 391–400.

Bluestein, H. B., 1993: *Synoptic-dynamic meteorology in midlatitudes. Volume II. Observations and theory of weather systems.* Oxford University Press. 594 pp.

Bott, A., 1998: A flux method for the numerical solution of the stochastic collection equation. *J. Atmos. Sci*., **55**, 2284–2293.

Bott, A., 2000: A flux method for the numerical solution of the stochastic collection equation: Extension to two-dimensional particle distributions. *J. Atmos. Sci.*, **57**, 284–294.

Burcea, C., R. Cică, and R. Bojariu, 2016: Hail climatology and trends in Romania: 1961-2014. *Mon. Wea. Rev*., **144**, 4289–4299.

Cao, Z., 2008: Severe hail frequency over Ontario, Canada: Recent trend and variability. *Geophys. Res. Lett.*, **35**, L14803.

Changnon, S. A., 1977: The scales of hail. *J. Appl. Meteorol.*, **16**, 626–648.

Changnon, S. A. and D. Changnon, 2000: Long-term fluctuations in hail incidences in the United States. *J. Climate.*, **13**, 658–664.

Chen, F., and J. Dudhia, 2001: Coupling an advanced land-surface/hydrology model

with the Penn State/NCAR MM5 modeling system. Part I: Model description and implementation. *Mon. Wea. Rev.*, **129**, 569–585.

Chen, S. M., M. Yau, and P. Bartello, 2017: Turbulence effects of collision efficiency and broadening of droplet size distribution in cumulus clouds. *J. Atmos. Sci.*, doi.org/10.1175/JAS-D-17-0123.1, in press.

Cheng, C. T., W. C. Wang, and J. P. Chen, 2007: A modelling study of aerosol impacts on cloud microphysics and radiative properties. *Q. J. R. Meteorol. Soc.*, **133**, 283–297.

Choi, I.-J., T. Iguchi, S.-W. Kim, T. Nakajima, and S.-C. Yoon, 2014: The effect of aerosol representation on cloud microphysical properties in Northeast Asia. *Meteorol. Atmos. Phys.*, **123**, 181–194.

Clavner, M., W. R. Cotton, S. C. van den Heever, S. M. Saleeby, and J. R. Pierce, 2018: The response of a simulated mesoscale convective system to increased aerosol pollution: Part I: Precipitation intensity, distribution, and efficiency. *Atmos. Res.*, **199**, 193–208.

Costa, A. A., C. J. Oliveira, J. C. P. Oliveira, and A. J. C. Sampaio, 2000: Microphysical observations of warm cumulus clouds in Ceará, Brazil. *Atmos. Res.*, **54**, 167–199.

Dagan, G., I. Koren, O. Altaratz, and R. H. Heiblum, 2017: Time-dependent, non-monotonic response of warm convective cloud fields to changes in aerosol loading. *Atmos. Chem. Phys.*, **17**, 7435–7444.

Dagvadorj, D., Z. Batjargal, and L. Natsagdorj, 2014: *MARCC 2014: Mongolia Second Assessment Report on Climate Change 2014*. Ministry of Environmental and

Green Development of Mongolia, Mongolia, 302 pp.

Dagvadorj, D., L. Natsagdorj, J. Dorjpurev, and B. Namkhainyam, 2009: *Mongolia Assessment Report on Climate Change 2009*. Ministry of Nature, Environment and Tourism, Mongolia, 228 pp.

Dee, D. P., S. M. Uppala, A. J. Simmons, P. Berrisford, P. Poli, S. Kobayashi, U. Andrae, M. A. Balmaseda, G. Balsamo, P. Bauer, P. Bechtold, A. C. M. Beljaars, L. van de Berg, J. Bidlot, N. Bormann, C. Delsol, R. Dragani, M. Fuentes, A. J. Geer, L. Haimberger, S. B. Healy, H. Hersbach, E. V. Hólm, L. Isaksen, P. Kållberg, M. Köhler, M. Matricardi, A. P. McNally, B. M. Monge-Sanz, J.-J. Morcrette, B.-K. Park, C. Peubey, P. de Rosnay, C. Tavolato, J.-N. Thépaut and F. Vitart, 2011: The ERA-Interim reanalysis: Configuration and performance of the data assimilation system. *Q. J. R. Meteorol. Soc.*., **137**, 553–597.

Dessens, J., 1986: Hail in southwestern France. I: hailfall characteristics and hailstorm environment. *J. Climate Appl. Meteorol*., **25**, 35–47.

Doljinsuren, M., and C. Gomes, 2015: Lightning incidents in Mongolia. *Geomatics, Natural Hazards and Risk*, **6**, 686–701.

Etkin, D., and S. E. Brun, 1999: A note on Canada's hail climatology: 1977–1993. *Int. J. Climatol.*, **19**, 1357–1373.

Fan, J. W., L. R. Leung, Z. Q. Li, H. Morrison, H. B. Chen, Y. Q. Zhou, Y. Qian, and Y. Wang, 2012: Aerosol impacts on clouds and precipitation in eastern China: Results from bin and bulk microphysics. *J. Geophys. Res.*, **117**, D00K36.

Fan, J., Y. Wang, D. Rosenfeld, and X. Liu, 2016: Review of Aerosol-Cloud interactions:

Mechanisms, Significance, and Challenges. *J. Atmos. Sci.*, **73**, 4221–4252.

Farnell, C., and M. D. C. Llasat Botija, 2013: Proposal of three thermodynamic variables to discriminate between storms associated with hail and storms with intense rainfall in Catalonia. *Tethys*, **10**, 25–34.

Gayatri, K., S. Patade, and T. Prabhakaran, 2017: Aerosol cloud interaction in deep convective clouds over the Indian peninsula using Spectral (bin) Microphysics. *J. Atmos. Sci.*, **74**, 3145–3166.

Giaiotti, D., S. Nordio, and F. Stel, 2003: The climatology of hail in the plain of Friuli Venezia Giulia. *Atmos. Res.*, **67–68**, 247–259.

Gillespie, D. T., 1972: The stochastic coalescence model for cloud droplet growth. *J. Atmos. Sci*., **29**, 1496–1510.

Gillespie, D. T., 1975a: Three models for the coalescence growth of cloud drops. *J. Atmos. Sci.*, **32**, 600–607.

Gillespie, D. T., 1975b: An exact method for numerically simulating the stochastic coalescence process in a cloud. *J. Atmos. Sci.*, **32**, 1977–1989.

Goulden, C. E., J. Mead, R. Horwitz, M. Goulden, B. Nandintsetseg, S. McCormick, B. Boldgiv, and P. S. Petraitis, 2016: Interviews of Mongolian herders and high resolution precipitation data reveal an increase in short heavy rains and thunderstorm activity in semi-arid Mongolia. *Climatic Change*, **136**, 281–295.

Grabowski, W. W., and L.-P. Wang, 2013: Growth of cloud droplets in a turbulent environment. *Annu. Rev. Fluid Mech.*, **45**, 293–324.

Groenemeijer, P. H., and A. van Delden, 2007: Sounding-derived parameters associated

with large hail and tornadoes in the Netherlands. *Atmos. Res.*, **83**, 473–487.

Hartmann, D. L., A. M. G. Klein Tank, M. Rusticucci, L. V. Alexander, S. Brönnimann, Y. Charabi, F. J. Dentener, E. J. Dlugokencky, D. R. Easterling, A. Kaplan, B. J. Soden, P. W. Thorne, M. Wild, and P. M. Zhai, 2013: Observations: Atmosphere and surface. *Climate Change 2013: The Physical Science Basis. Contribution of Working Group I to the Fifth Assessment Report of the Intergovernmental Panel on Climate Change*. Cambridge University Press, 159–254.

Han, J.-Y., J.-J. Baik, and A. P. Khain, 2012: A numerical study of urban aerosol impacts on clouds and precipitation. *J. Atmos. Sci.*, **69**, 504–520.

Hong, S.-Y., Y. Noh, and J. Dudhia, 2006: A new vertical diffusion package with an explicit treatment of entrainment processes. *Mon. Wea. Rev.*, **134**, 2318–2341.

Houze, R., 2014: *Cloud Dynamics.* 2nd ed., Academic Press, 432 pp.

Huffman, G., D. T. Bolvin, and E. J. Nelkin, 2015: *Integrated Multi-satellitE Retrievals for GPM (IMERG) technical documentation*, NASA Goddard Space Flight Center, 19 June. [Available at http://pmm.nasa.gov/sites/default/files/document_files/IMERG_doc.pdf]

Iacono, M. J., J. S. Delamere, E. J. Mlawer, M. W. Shephard, S. A. Clough, and W. D. Collins, 2008: Radiative forcing by long-lived greenhouse gases: Calculations with the AER radiative transfer models. *J. Geophys. Res.*, **113**, D13103.

Igel, A. L., S. C. van den Heever, C. M. Naud, S. M. Saleeby, and D. J. Posselt, 2013: Sensitivity of warm-frontal processes to cloud-nucleating aerosol concentrations.

J. Atmos. Sci., **70**, 1768–1783.

Iguchi, T., T. Nakajima, A. P. Khain, K. Saito, T. Takemura, H. Okamoto, T. Nishizawa, and W. K. Tao, 2012: Evaluation of cloud microphysics in JMA-NHM simulations using bin or bulk microphysical schemes through comparison with cloud radar observations. *J. Atmos. Sci.*, **69**, 2566–2586.

Ilotoviz, E., A. P. Khain, N. Benmoshe, V. T. Phillips, and A. V. Ryzhkov, 2016: Effect of aerosols on freezing drops, hail, and precipitation in a midlatitude storm. *J. Atmos. Sci.*, **73**, 109–144.

Jambaajamts, B., 1989: *Climate of Mongolia*. Ulsiin hevlel Publishers, 271 pp. (in Mongolian).

Jin, H.-G., H. Lee, J. Lkhamjav, and J.-J. Baik, 2017: A hail climatology in South Korea. *Atmos. Res.*, **188**, 90–99.

Kahraman, A., S. Tilev-Tanriover, M. Kadioglu, D. M. Schultz, and P. M. Markowski, 2016: Severe hail climatology of Turkey. *Mon. Wea. Rev.*, **144**, 337–346.

Kain, J. S., 2004: The Kain–Fritsch convective parameterization: an update. *J. Appl. Meteorol*., **43**, 170–181.

Kessler, E., 1969: *On the Distribution and Continuity of Water Substance in Atmospheric Circulations*, AMS, Massachusetts. 84 pp.

Khain, A., 2009: Notes on state-of-the-art investigations of aerosol effects on precipitation: a critical review. *Environ. Res. Lett.*, **4**, 015004.

Khain, A. P., K. Beheng, A. Heymsfield, A. Korolev, S. Krichak, Z. Levin, M. Pinsky, V. Phillips, T. Prabhakaran, A. Teller, S. C. van den Heever, and J.-I. Yano, 2015:

Representation of microphysical processes in cloud-resolving models: Spectral (bin) microphysics versus bulk parameterization. *Rev. Geophys.*, **53**, 247–322.

Khain, A. P., M. Ovtchinnikov, M. Pinsky, A. Pokrovsky, and H. Krugliak, 2000: Notes on the state-of-the-art numerical modeling of cloud microphysics. *Atmos. Res.*, **55**, 159–224.

Khain, A., A. Pokrovsky, and I. Sednev, 1999: Some effects of cloud aerosol interaction on cloud microphysics structure and precipitation formation: Numerical experiments with a spectral microphysics cloud ensemble model. *Atmos. Res.*, **52**, 195–220.

Khain, A., D. Rosenfeld, and A. Pokrovsky, 2005: Aerosol impact on the dynamics and microphysics of deep convective clouds. *Q. J. R. Meteorol. Soc.*, **131**, 1–25.

Khain, A., D. Rosenfeld, A. Pokrovsky, U. Blahak, and A. Ryzhkov, 2011: The role of CCN in precipitation and hail in a mid-latitude storm as seen in simulations using a spectral (bin) microphysics model in a 2D dynamic frame. *Atmos. Res.*, **99**, 129–146.

Khain, A. P., I. Sednev, and V. Khvorostyanov, 1996: Simulation of coastal circulation in the eastern Mediterranean using a spectral microphysics cloud ensemble model. *J. Climate*., **9**, 3298–3316.

Kim, C., and X. Ni, 2015: Climatology of hail in North Korea. *Acta Sci. Nat. Univ. Pekin*, **51**, 437–443 (in Chinese with English abstract).

Kogan, Y. L., 1993: Drop size separation in numerically simulated convective clouds and its effect on warm rain formation. *J. Atmos. Sci*., **50**, 1238–1253.

Köhler, H., 1936: The nucleus in and the growth of hygroscopic droplets. *J. Chem. Soc. Faraday Trans*., **32**, 1152–1161.

Kotinis-Zambakas, S. R., 1989: Average spatial patterns of hail days in Greece. *J. Climate*, **2**, 508–511.

Kuba, N., and Y. Fujiyoshi, 2006: Development of a cloud microphysical model and parameterizations to describe the effect of CCN on warm cloud. *Atmos. Chem. Phys*., **6**, 2793–2810.

Kunz, M., J. Sander, and Ch. Kottmeier, 2009: Recent trends of thunderstorm and hailstorm frequency and their relation to atmospheric characteristics in southwest Germany. *Int. J. Climatol*., **29**, 2283–2297.

Langmuir, I., 1948: The production of rain by a chain reaction in cumulus clouds at temperatures above freezing. *J. Meteorol*., **5**, 175–192.

Lee, H., and J.-J. Baik, 2016: Effects of turbulence-induced collision enhancement on heavy precipitation: The 21 September 2010 case over the Korean Peninsula. *J. Geophys. Res. Atmos*., **121**, 12319–12342.

Lee, H., and J.-J. Baik., 2017: A physically based autoconversion parameterization. *J. Atmos. Sci.*, **74**, 1599–1616.

Lee, H., J.-J. Baik, and J.-Y. Han, 2014: Effects of turbulence on mixed-phase deep convective clouds under different basic-state winds and aerosol concentrations. *J. Geophys. Res. Atmos*., **119**, 13506–13525.

Lee, H., J.-J. Baik, and J.-Y. Han, 2015: Effects of turbulence on warm clouds and precipitation with various aerosol concentrations. *Atmos. Res.*, **153**, 19–33.

Lee, S. S., L. J. Donner, V. T. Phillips, and Y. Ming, 2008: The dependence of aerosol effects on clouds and precipitation on cloud-system organization, shear and stability. *J. Geophys. Res.*, **113,** D16202.

Li, M., Q. Zhang, and F. Zhang, 2016: Hail day frequency trends and associated atmospheric circulation patterns over China during 1960–2012. *J. Climate*, **29**, 7027–7044.

Lim, K.-S. S., and S.-Y. Hong, 2010: Development of an effective double-moment cloud microphysics scheme with prognostic cloud condensation nuclei (CCN) for weather and climate models. *Mon. Wea. Rev*., **138**, 1587–1612.

Lin, Y.-L, R. D. Farly, and H. D. Orville, 1983: Bulk parameterization of the snow field in a cloud model. *J. Climate Appl. Meteorol.*, **22**, 1065–1092.

Lynn, B. H., A. Khain, J. Dudhia, D. Rosenfeld, A. Pokrovsky, and A. Seifert, 2005a: Spectral (bin) microphysics coupled with a mesoscale model (MM5). Part I: Model description and first results. *Mon. Wea. Rev*., **133**, 44–58.

Lynn, B. H., A. P. Khain, J. Dudhia, D. Rosenfeld, A. Pokrovsky, and A. Seifert, 2005b: Spectral (bin) microphysics coupled with a mesoscale model (MM5). Part II: Simulation of a CaPE rain event with a squall line. *Mon. Wea. Rev*., **133**, 59–71.

McGraw, R., and Y. Liu, 2006: Brownian drift-diffusion model for evolution of droplet size distributions in turbulent clouds, *Geophys. Res. Lett.*, **33**, L03802.

Mezher, R. N., M. Doyle, and V. Barros, 2012: Climatology of hail in Argentina. *Atmos. Res.*, **114–115**, 70–82.

Nisi, L., O. Martius, A. Hering, M. Kunz, and U. Germann, 2016: Spatial and temporal

distribution of hailstorms in the Alpine region: a long-term, high resolution, radar-based analysis. *Q. J. R. Meteorol. Soc.*, **142**, 1590–1604.

Ogura, Y., and T. Takahashi, 1973: The development of warm rain in a cumulus cloud. *J. Atmos. Sci.*, **30**, 262–277.

O'Halloran, T. L., J. D. Fuentes, W. K. Tao, and X. Li, 2015: Sensitivity of convection to observed variation in aerosol size distributions and composition at a rural site in the southeastern United States. *J. Atmos. Chem.*, **72**, 441–454.

Phillips, V. T. J., A. Pokrovsky, and A. Khain, 2007: The influence of time-dependent melting on the dynamics and precipitation production in maritime and continental storm clouds. *J. Atmos. Sci.*, **64**, 338–359.

Pinsky, M., A. P. Khain, and H. Krugliak, 2008: Collisions of cloud droplets in a turbulent flow. Part V: Application of detailed tables of turbulent collision rate enhancement to simulation of droplet spectra evolution. *J. Atmos. Sci.*, **65**, 357–374.

Pinsky, M., A. Khain, and M. Shapiro, 2001: Collision efficiency of drops in a wide range of Reynolds number: Effects of pressure on spectrum evolution. *J. Atmos. Sci.*, **58**, 742–764.

Pruppacher, H. R., and J. D. Klett, 1997: *Microphysics of Clouds and Precipitation*. 2nd ed. Kluwer Academic Publishers, 954 pp.

Punge, H. J., and M. Kunz, 2016: Hail observations and hailstorm characteristics in Europe: A review. *Atmos. Res.*, **176**, 159–184.

Rosenfeld, D., 1999: TRMM observed first direct evidence of smoke from forest fires

inhibiting rainfall. *Geophys. Res. Lett.*, **26**, 3105–3108.

Rosenfeld, D., U. Lohmann, G. B. Raga, C. D. O'Dowd, M. Kulmala, S. Fuzzi, A. Reissell, and M. O. Andreae, 2008: Flood or drought: How do aerosols affect precipitation?. *Science*, **321**, 1309–1313.

Sarangi, C., S. N. Tripathi, V. P. Kanawade, I. Koren, and D. S. Pai, 2017: Investigation of the aerosol-cloud-rainfall association over the Indian summer monsoon region. *Atmos. Chem. Phys.*, **17**, 5185–5204.

Sato, Y., T. Nakajima, K. Suzuki, and T. Iguchi, 2009: Application of a Monte Carlo integration method to collision and coagulation growth processes of hydrometeors in a bin-type model. *J. Geophys. Res.*, **114**, D09215.

Schaefer, J. T., J. J. Levit, S. J. Weiss, and D. W. McCarthy, 2004: The frequency of large hail over the contiguous United States. *Preprints of the 14th Conf. on Applied Climatology*, AMS, Seattle, 7 pp.

Schuster, S. S., R. J. Blong, and M. S. Speer, 2005: A hail climatology of the Greater Sydney area and New South Wales. Australia. *Int. J. Climatol.*, **25**, 1633–1650.

Seifert, A., and K. Beheng, 2006: A two-moment cloud microphysics parameterization for mixed-phase clouds. Part 1: Model description. *Meteorol. Atmos. Phys*., **92**, 45–66.

Simeonov, P., L. Bocheva, and T. Marinova, 2009: Severe convective storms phenomena occurrence during the warm half of the year in Bulgaria (1961–2006). *Atmos. Res.*, **93**, 498–505

Sioutas, M., T. Meaden, and J. D. C. Webb, 2009: Hail frequency, distribution, and

intensity in northern Greece. *Atmos. Res.*, **93**, 526–533.

Skamarock, W. C., J. B. Klemp, J. Dudhia, D. O. Gill, D. M. Barker, M. G. Duda, X.-Y. Huang, W. Wang, and J. G. Powers, 2008: *A description of the advanced research WRF version 3*. NCAR Technical Note, NCAR/TN–475+STR, NCAR, 113 pp.

Suwala, K., and E. Bednorz, 2013: Climatology of hail in Central Europe. *Quaestiones Geographicae*, **32**, 99–110.

Straka, J. M., 2009: *Cloud and Precipitation Microphysics: Principles and Parameterizations*. Cambridge University Press, 392 pp.

Tao, W.-K., and X. Li, 2016: The relationship between latent heating, vertical velocity, and precipitation processes: The impact of aerosols on precipitation in organized deep convective systems. *J. Geophys. Res. Atmos.*, **121**, 6299–6320.

Tao, W.-K, J.-P. Chen, Z. Li, C. Wang, and C. Zhang, 2012: Impact of aerosols on convective clouds and precipitation. *Rev. Geophys.*, **50**, RG2001.

Tao, W.-K, X. Li, A. Khain, T. Matsui, S. Lang, and J. Simpson, 2007: Role of atmospheric aerosol concentration on deep convective precipitation: Cloud-resolving model simulations. *J. Geophys. Res.*, **112**, D24.

Telford, J., 1955: A new aspect of coalescence theory. *J. Meteorol*., **12**, 436–444.

Tippett, M., J. T. Allen, V. A. Gensini, and H. E. Brooks, 2015: Climate and hazardous convective weather. *Curr. Climate Change Rep.*, **1**, 60–73.

Tuovinen, J. P., A. J. Punkka, J. Rauhala, H. Hohti, and D. M. Schultz, 2009: Climatology of severe hail in Finland: 1930–2006. *Mon. Wea. Rev.*, **137**, 2238–

2249.

Twomey, S., 1959: The nuclei of natural cloud formation. Part II: The supersaturation in natural clouds and the variation of cloud droplet concentration. *Pure Appl. Geophys.*, **43**, 243–249.

Twomey, S., 1964: Statistical effects in the evolution of a distribution of cloud droplets by coalescence, *J. Atmos. Sci.*, **21**, 553–557

Twomey, S., 1977: Influence of pollution on shortwave albedo of clouds. *J. Atmos. Sci.*, **34**, 1149–1152.

van den Heever, S. C., G. G. Carrio, W. R. Cotton, P. J. DeMott, and A. J. Prenni, 2006: Impacts of nucleating aerosol on Florida storms. Part I: Mesoscale simulations. *J. Atmos. Sci.*, **63**, 1752–1775.

Vinet, F., 2001: Climatology of hail in France. *Atmos. Res.*, **56**, 309–323.

Wang, C., 2005: A modeling study of the response of tropical deep convection to the increase of cloud condensation nuclei concentration: 1. Dynamics and microphysics. *J. Geophys. Res.*, **110**, D21211

Wang, L. P., Y. Xue, O. Ayala, and W. W. Grabowski, 2006: Effect of stochastic coalescence and air turbulence on the size distribution of cloud droplets. *Atmos. Res.*, **82**, 416–432.

Webb, J. D. C., D. M. Elsom, and D. J. Reynolds, 2001: Climatology of severe hailstorms in Great Britain. *Atmos. Res.*, **56**, 291–308.

Xiao, H., Y. Yin, L. Jin, Q. Chen, and J. Chen, 2015: Simulation of the effects of aerosol on mixed-phase orographic clouds using the WRF model with detailed bin

microphysics scheme. *J. Geophys. Res. Atmos.*, **120**, 8345–8358.

Xie, B., Q. Zhang, and Y. Wang, 2008: Trends in hail in China during 1960–2005. *Geophys. Res. Lett.*, **35**, L13801.

Xue, H., and G. Feingold, 2006: Large-eddy simulations of trade wind cumuli: Investigation of aerosol indirect effects. *J. Atmos. Sci.*, **63**, 1605–1622.

Xue, L., A. Teller, R. Rasmussen, I. Geresdi, Z. Pan, and X. Liu, 2012: Effects of aerosol solubility and regeneration on mixed-phase orographic clouds and precipitation. *J. Atmos. Sci.*, **69**, 1994–2010.

Young, K. C., 1975: The evolution of drop spectra due to condensation, coalescence and breakup. *J. Atmos. Sci*., **32**, 965–973.

Zhang, C., Q. Zhang, and Y. Wang, 2008: Climatology of hail in China: 1961–2005. *J. Appl. Meteorol. Climatol.*, **47**, 795–804

Zhou, X., N. Bei, H. Liu, J. Cao, L. Xing, W. Lei, L. T. Molina, and G. Li, 2017: Aerosol effects on the development of cumulus clouds over the Tibetan Plateau. *Atmos. Chem. Phys.*, **17**, 7423–7434.

초 록

충돌-병합 과정에 의한 구름 방울의 크기 분포 변화는 주로 확률 포착 방정식(SCE)을 결정론적인 방법으로 푸는 준 확률 포착 모형을 통해 계산된다. 본 연구에서는 유한한 적분 시간 간격을 엄밀하게 고려함으로써 개선된 준 확률 포착(IQS) 모형을 기존의 확률 포착(NQS) 모형과 비교하여 분석하였다. IQS 모형에서는 적분 시간 간격 동안 충돌 확률이 매우 작은 조건하에서도 큰 물방울이 작은 물방울을 한 번 이상 포획할 수 있다. 그 결과, 큰 물방울이 작은 물방울과 충돌하는 횟수가 푸아송 분포를 따르게 된다. 난류가 유도하는 충돌 향상(TICE)을 함께 고려한 상자 모형을 이용한 결과, IQS 모형에서 큰 물방울들의 크기가 대체로 NQS 모형보다 큰 것으로 나타났고, NQS 모형에서보다 IQS 모형에서의 큰 물방울 생성 시간이 수분가량 단축되었다. IQS 모형의 효과는 적분 시간 간격과 초기 물방울들의 크기 분포 형태에 따라 달라진다. IQS 모형이 포함된 상세 bin 구름 미세물리 모형을 Weather Research and Forecasting (WRF) 모형에 결합하였고, 이를 이용해 이상적인 대기 조건 하의 단일 온난 구름을 수치 모의하였다. 그 결과, IQS 모형의 결과에서 강수 시작 시점이 앞당겨진 것을 확인하였다.

강수량 예측의 관점에서 IQS 모형을 NQS 모형과 비교하여 평가하였다. 이를 위해 2014년 8월 21일에 몽골 중북부 지역에서 발생한 강수를 상세 bin 구름 미세물리 모형을 결합한 WRF 모형을 이용하여 모의하였다. NQS 모형보다 IQS 모형에서 지표 강수량이 더 많이 모의되었으며, 특히 강수가 집중된 영역에서 차이가 두드러졌다. IQS 모형에서의 수상 간 다중 충돌로 인하여 작은 물방울 및 큰 물방울의 질량 함량이 높았다. 큰 물방울의 질량 함량 증가는 지표 강수량 증가로 이어졌다. 증가한 작은 물방울은 연직 위로 수송되었고, 이로 인해 눈송이의 질량 함량이 증가하였다. IQS 모형에서 결착 및 수증기 침착이 더 활발하게 일어났으며, 이로 인해 눈송이 질량 함량이 더욱 증가하였다. 질량 함량이 증가된 눈송이는 녹아 지표 강수량을 증가

시켰다.

에어로졸 하중이 중위도 깊은 대류계의 강수에 미치는 영향을 연구하였다. 이를 위해 2014년 8월 21일에 몽골 중북부 지역에서 발생한 강수 사례를 N_0 = 150, 300, 600, 1200, 2400, 4800 cm^{-3} 인 여러 에어로졸 수 농도에 대하여 수치 모의하였다. N_0 = 150–600 cm^{-3} 의 범위에서 에어로졸 하중이 증가함에 따라 강수량이 약간 감소하였으나, N_0 = 600–4800 cm^{-3} 의 범위에서는 강수량이 급격한 증가 추세(에어로졸 수 농도가 8배 증가하였을 때, 강수량이 22% 증가)를 보였다. N_0 = 600–4800 cm^{-3} 의 범위에서 에어로졸 수 농도가 증가할 때 강수량이 증가하게 된 원인을 분석하였다. 높은 에어로졸 하중 하에서는 작은 물방울이 더 많이 생성된다. 이 작은 물방울들은 응결을 통해 성장하며, 일부가 연직 위로 수송되면 결빙을 거쳐 얼음 결정의 질량 함량을 증가시킨다. 얼음 결정의 질량 함량 증가는 주로 수증기 침착을 통해 작은 눈송이의 질량 함량 증가로 이어지며, 결착을 통해 큰 눈송이 질량 함량 증가로 이어진다. 한편, 더 많은 양의 작은 물방울은 과냉각 수적의 질량 함량을 증가시키며, 이는 결착을 통한 큰 눈송이의 질량 함량 증가의 요인이 된다. 앞선 요인들에 의하여 질량 함량이 증가한 큰 눈송이는 낙하 과정을 통해 융해 및 충돌–병합 과정을 거치면서, 지표 강수량 증가에 기여한다.

주요어: 개선된 준 확률 포착 모형, bin 구름 미세물리, WRF 모형, 구름 및 강수, 에어로졸, 우박 기후, 몽골

학 번: 2014-30900